

Politecnico di Torino

Quantum Engineering

A.y. 2025/2026

Graduation session: September 2026

On-Demand Qubit and Gate Characterization

Developing Diagnostic Subroutines
for the *Lagrange* QPU

Supervisors:

Prof. Bartolomeo Montrucchio
(Politecnico di Torino)

Dr. Emanuele Dri
(LINKS)

Dr. Giacomo Vitali
(LINKS)

Candidate:

Federico Fissore
s323191

Contents

Abstract 1
1. Introduction 2
    1.1. Structure of this work 3
    1.2. Use of Artificial Intelligence 4
2. Theoretical Framework 5
    2.1. Quantum States 5
    2.2. Quantum Gates 9
    2.3. Universal computation and Clifford Gates 16
    2.4. Density Matrix and Kraus Formalism 23
    2.5. Error Models 29
3. System Architecture 40
    3.1. The *Lagrange* Quantum Computer 40
    3.2. Transmon Qubits 40
        3.2.1. Josephson Junction 41
        3.2.2. Charge qubit 43
        3.2.3. Transmon qubit 45
    3.3. Qubits control 52
    3.4. Qubits Readout 59
    3.5. The software stack 64
4. Experiments 69
    4.1. SPAM Errors Characterization 69
        4.1.1. Confusion Matrix 69
        4.1.2. I-Q Cloud 70
    4.2. Spectroscopy 71
    4.3. Qubit coherence characterization 73
        4.3.1. Inversion Recovery (T1) 73
        4.3.2. Ramsey experiment (T_2^*) 74
        4.3.3. Hahn-Echo (T_2) 76
    4.4. Gates characterization 78
        4.4.1. All-XY 78
        4.4.2. Randomized Benchmarking 81
        4.4.3. Interleaved Randomized Benchmarking 83
5. Implementation and Results 86
    5.1. SPAM Errors 86
        5.1.1. Confusion Matrix 86
        5.1.2. I-Q Cloud 88
    5.2. Spectroscopy 90
    5.3. Qubit coherence characterization 95
        5.3.1. Inversion Recovery (T1) 95
        5.3.2. Ramsey (T_2^*) 96
        5.3.3. Hahn-Echo (T_2) 98

5.4. Gates characterization 100
5.4.1. All-XY 100
5.4.2. Randomized Benchmarking 102
5.4.3. Interleaved Randomized Benchmarking 103
6. Conclusions and Future Perspectives 106
6.1. Conclusions 106
6.2. Future Perspectives 107
A. Appendix 108
A.1. Bloch Sphere 108
A.2. Unitary Transformations 110
Bibliography 112

Abstract

The work presented in this thesis aims to develop a standalone, on-demand toolset to characterize qubit parameters as well as single-qubit gates. Having a reliable procedure to characterize key parameters of a quantum computer enables the proper scheduling of jobs by also offering an estimation of the validity of computed results. The practical utility of the toolset is proven on the on-premise quantum machine *Lagrange*, an IQM Spark machine equipped with a Quantum Processing Unit (QPU) composed of 5 superconducting transmon qubits interconnected by means of tunable couplers in a star topology. [1] Following a top-down approach, this thesis begins with a computer engineering perspective. The compilation stages —as well as the passes that compose them — are examined to bring a complete understanding of the executed algorithms that act on high-level quantum circuits translating them into the corresponding sequence of scheduled pulses to be executed. *Qiskit* circuits are transpiled for the *Spark* hardware. Validation of different parameters regarding the *Lagrange* machine is performed by means of typical gate-level algorithms. The characterization of typical qubit parameters is performed by standard procedures. Longitudinal relaxation time T_1 is evaluated with the Inversion Recovery experiment by fitting the exponential decay of the probability of measuring the prepared $|1\rangle$. Similarly, the Hahn Echo experiment is performed to characterize the T_2 dephasing time. State Preparation And Measurement (SPAM) errors are investigated by exploiting the measurement apparatus of superconducting qubits: measured states are evaluated by acquiring the resulting IQ cloud, allowing the identification of main sources of systematic error and to therefore apply the Readout Error Mitigation (REM) procedure. Randomized Benchmarking (RB) is used to evaluate the average error rate in *m-long* sequences of Clifford gates [2] Interleaved Randomized Benchmarking (IRB) is used to characterize the performance of a specific gate. [3] Summarizing, this work opens the door to low-level access of the *Lagrange* quantum computer, offering a validation of high-level parameters and a solid ground to build future work on top and covering all the main aspects of a full-stack quantum system.

Chapter 1
Introduction

Over the last two decades, quantum computing has evolved towards sophisticated devices capable of executing non-trivial circuits. However, Quantum Processing Units (QPUs) nowadays operate within the Noisy Intermediate-Scale Quantum (NISQ) era: they are constrained by a limited number of physical qubits, resources are not sufficient for reliable error correction, and they still contain physical imperfections due to state preparation, operations, and measurements. Achieving large-scale, fault-tolerant quantum computing (FTQC) is certainly one of the main goal in the field, but also not a simple one: it requires logical information to be encoded across multiple qubits to suppress these errors. Furthermore, these QPUs are increasingly integrated into High-Performance Computing (HPC) environments alongside classical resources. This leads even more to the need of a deeper understanding of quantum hardware and the mechanisms through which it can be controlled and investigated. From a mathematical point of view, quantum gates are represented as unitary transformations acting on state vectors. In our physical world, a quantum processor cannot manipulate these abstract states directly; instead, operations are realized through physical interactions and external control fields. For example, in superconducting processors, operations are driven by microwave control fields to induce energy level transitions. The success of these implementations can be explained with the precision of control parameters like the frequency, amplitude, time interval, phase, and waveform of the applied pulses. The same reasoning can be applied to quantum measurements: the procedure of measuring does not directly output abstract states but they are extracted through physical readout processes and lower-level signal acquisition chains. Following the fact that physical implementations are different from ideal mathematical models, experimental characterization is vital to uncover a device's physical properties and operational imperfections. Complete information about a device is built by means of different tests which provide complementary properties and blocks: spectroscopy investigates qubit transition frequencies, coherence measurements track temporal behavior, and protocols like All-XY

and randomized benchmarking evaluate the performance of quantum gates. A comprehensive understanding of the processor requires combining these multiple diagnostic procedures and adapting them to the capabilities of the specific hardware and software infrastructure.

1.1. Structure of this work

This thesis adopts a broad perspective, with the aim of giving a complete overview, spanning from the physical principles of the qubits up through their control mechanisms, gate implementations, software infrastructure, and acquisition of experimental data. Standard high-level gate instructions are often insufficient for a deep characterization: pulse-level access is instead crucial. This is a lower-level control that enables to directly manipulate drive frequencies, realize custom waveforms, and access basic experimental signals. The primary focus of the thesis is the experimental characterization of the *Lagrange* QPU at Politecnico di Torino. The work is divided into five main sections:

In Chapter 2, the theoretical background required to understand the subsequent chapters is introduced, including the relevant concepts of quantum computing and the derivation of selected mathematical models, to provide an intuitive understanding of the framework of the experiments.

In Chapter 3, the architecture of the *Lagrange* quantum computer is described, starting from the high-level software interface down to the physical hardware. Particular attention is devoted to superconducting transmon qubits, their control and readout mechanisms, and the software infrastructure used to submit, compile, schedule, and execute quantum operations and experiments.

In Chapter 4, the diagnostic procedures investigated in this thesis are presented, along with their theoretical principles and experimental methodologies, establishing the basis for their implementation on the QPU.

In Chapter 5, the implementation of the procedures and the experimental results obtained from their execution on the Lagrange QPU are presented and discussed. The extracted parameters for the characterization are examined in

relation to the expected behavior of the device, considering also the practical aspects encountered during the experiments.

Finally, Chapter 6 summarizes the main contributions of the thesis, discusses the advantages and limitations identified during the experimental work, and outlines possible directions for future developments. These include further extensions of the characterization procedures and the investigation of more comprehensive calibration methodologies.

1.2. Use of Artificial Intelligence

During the preparation of this thesis, artificial intelligence was used as an assistive tool. Specifically, AI-based tools supported the generation of boilerplate code for data visualization and plotting, as well as the proofreading of the manuscript to identify typographical errors and improve stylistic consistency. All AI-generated code and text were reviewed, verified, and edited by the author.

Chapter 2
Theoretical Framework

In this chapter, an intuition on basic concepts will be provided, as well as a coarse mathematical overview. Many details will be left uncovered as not strictly mandatory for the appreciation of the work, suggested reading to deepen the topic are [4] and, for a more computer scientist oriented description, [5].

2.1. Quantum States

The framework in which quantum information is described is very well established and here briefly reported.
In a classical framework, information is the property of a probabilistic event, related only to the probability of its outcomes, returning the average *surprise* when happens. The concept of surprise intended here, is the logarithm of the probability of each outcome: $-\log(p)$, an impossible event ($\mathbb{P} = 0$) would have an infinite surprise if happens, conversely a certain event ($\mathbb{P} = 1$) would be in no way surprising. Therefore for a random variable X its information is

$$\langle X \rangle = \sum -\log(p_i)p_i \tag{2.1}$$

where i iterates over all the possible outcomes. It is clear that the smallest random variable to have information must have at least 2 outcomes.[1] All the relevant classical computation is performed exploiting binary (boolean) systems therefore the logarithm is intended in base 2, resulting in binary digits: *bits*.

The smallest amount of quantum information, analogously as classical information, is hosted in a 2 state system that now plays a whole different game: it follows the rules of quantum mechanics. Mathematically such state is a normalized complex vector embedded in a Hilbert space of dimension 2.

The most intuitive way to label such states naturally follows classical computation, so the *computational basis* is defined: basis vectors are

[1] This description is valid only for discrete random variables but it can be extended for countinuous ones.

$$|0\rangle = \begin{pmatrix} 1 \\ 0 \end{pmatrix} \qquad |1\rangle = \begin{pmatrix} 0 \\ 1 \end{pmatrix} \tag{2.2}$$

The generic 2 level quantum state is represented as

$$|\psi\rangle = \alpha|0\rangle + \beta|1\rangle = \begin{pmatrix} \alpha \\ \beta \end{pmatrix} \tag{2.3}$$

Being the framework for quantum mechanics built upon complex numbers, $\alpha, \beta \in \mathbb{C}$ and, to fullfull the normalization condition, $|\alpha|^2 + |\beta|^2 = 1$. This vector is the simplest element of quantum information: the quantum bit (Qubit).

A qubit can be well visualized by taking the two basis vectors ($|0\rangle$ and $|1\rangle$) and posing them as two poles of a sphere. This very useful tool is called Bloch sphere, shown in Figure 1.

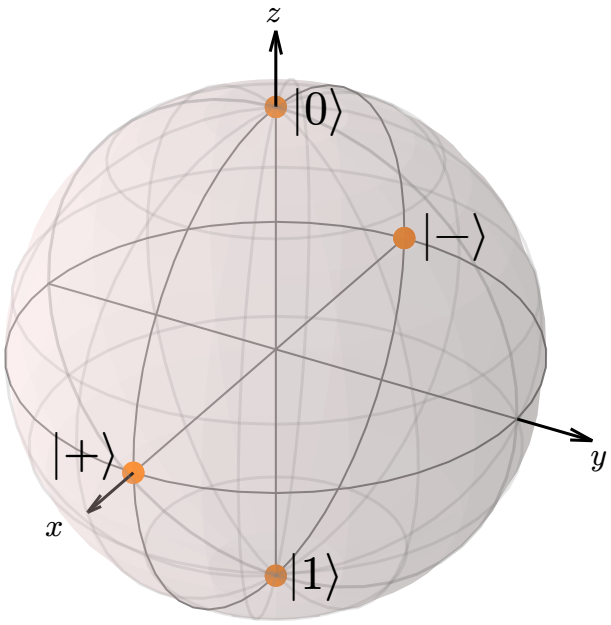


Figure 1: A representation of the Bloch sphere, made with QuTip.

A very common alternative to the computational basis (poles on the z-axis) is the *Fourier basis* or *Hadamard basis*, in which basis vectors are the ones lying

on the x-axis, they are conveniently labelled as $|+\rangle$ and $|-\rangle$ and expressed in the computational basis as reported in Eq. (2.4). Also the y-axis has its states, used much less with respect to the previous, they are often labeled as $|+i\rangle$ and $|-i\rangle$ but such notation may be confusing for multi qubit systems so they are also labeled as $|R\rangle$ and $|L\rangle$ recalling Poincaré sphere.

$$\begin{cases} |+\rangle = \dfrac{|0\rangle + |1\rangle}{\sqrt{2}} \\ |-\rangle = \dfrac{|0\rangle - |1\rangle}{\sqrt{2}} \end{cases} \qquad \begin{cases} |+i\rangle = |R\rangle = \dfrac{|0\rangle + i|1\rangle}{\sqrt{2}} \\ |-i\rangle = |L\rangle = \dfrac{|0\rangle - i|1\rangle}{\sqrt{2}} \end{cases} \tag{2.4}$$

In the universe, many quantum states exist simultaneously, how could someone write them as a single one? To answer this question let us start with an example: two independent qubits (i.e. no interaction between them): A, B so their states can be written in the general form as

$$\begin{cases} |\psi_A\rangle = a_0|0\rangle + a_1|1\rangle \\ |\psi_B\rangle = b_0|0\rangle + b_1|1\rangle \end{cases} \tag{2.5}$$

Then let us build all their possible combinations, by picking the first basis of the first state and iterating over all the basis of the second state. This operation can be thought as two nested loops (or if more states are considered, a recursive function, for which each state is a layer of recursion). Working with qubits allows to visualze such operation with a binary tree, as shown in Figure 2. This operation has created a bigger vector space starting from smaller ones, specifically the dimension of the output one is the product of the dimensions of the input two. This is no surprise because it should embed all the possibile combinations of basis vectors. Mathematically this operation is called *tensor product* ($\otimes$). Bra-Ket notation allows to implicitly use the tensor product when writing more bras one after another. Moreover it is widely adopted the `unsigned int` notation to label states in a multi-qubit system.

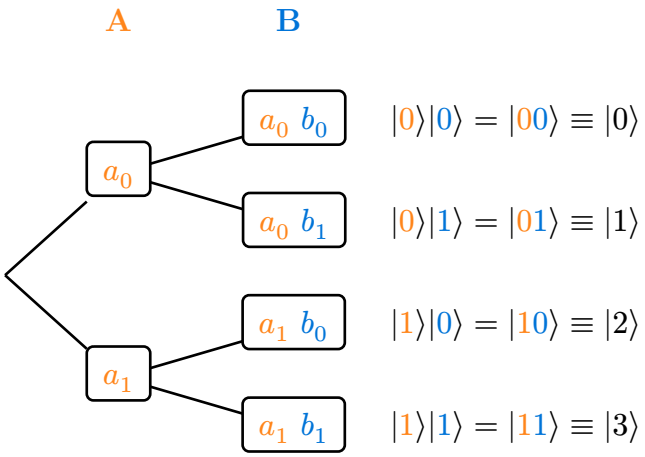


Figure 2: Binary tree as a visualization of the tensor product

Just like in probability theory, for independent distributions the joint one is the product of the marginals. But this is a specific case, joint distributions may have some correlations, in such cases marginal ones are no longer sufficient to precisely describe the phenomenon. In the same way, in quantum mechanics, when a state cannot be decomposed (i.e. written as tensor product) into smaller ones, it is said to be *entangled*.

As an example, consider the following state:

$$|\psi\rangle = \frac{|00\rangle + |11\rangle}{\sqrt{2}} \tag{2.6}$$

then suppose it can be written as

$$\begin{aligned} |\psi_A\rangle|\psi_B\rangle &= (a_0|0\rangle + a_1|1\rangle)(b_0|0\rangle + b_1|1\rangle) \\ &= a_0b_0|00\rangle + a_0b_1|01\rangle + a_1b_0|10\rangle + a_1b_1|11\rangle \end{aligned} \tag{2.7}$$

It would require that both $a_0b_1 = 0$ and $a_1b_0 = 0$ but this is impossible because if any of these coefficients is 0; Therefore Eq. (2.6) cannot be equal to Eq. (2.7), this is an example of an entangled state.

2.2. Quantum Gates

Evolution of quantum states is described by the *evolution postulate*:

The time evolution of a closed quantum system is described by the Schrödinger equation.

$$i\hbar\partial_t|\psi\rangle = \widehat{\mathcal{H}}|\psi\rangle \tag{2.8}$$

The main actor of such equation is the Hamiltonian operator ($\mathcal{H}$), containing all the information of the system (energetic landscapes, interactions…). This tool is very fundamental when describing the physical qubit evolution, coupled with an external system.

Although very powerful, this postulate works well in a *continuous time* domain, in contrast with the *discrete* evolution of most quantum computation. Most widely diffused quantum computers follow this kind of paradigm, known as *digital* quantum computing, in contrast with *analog* quantum computing in which qubits evolve continuously in time.

For such purpose an alternative, more generic, formulation of the postulate is considered:

The evolution of a closed quantum system is described by a unitary transformation.

$$|\psi_2\rangle = \hat{U}|\psi_1\rangle \tag{2.9}$$

As a notation standard, let us use a pedix with the state to indicate the discrete temporal index; it is equivalent of a continuous time system of $|\psi(t_i)\rangle$. For a better description of the concept of unitary transformation, see Appendix A.2.
What is relevant here is that it is possible to manipulate qubits to act precisely as desired, performing computations.

The very starting point is some gate that, when applied to states in the computational basis, does not transform them; in other words they must be eigenvectors of such gate: we are looking for a matrix which is diagonal in the computational basis. To avoid any problems related to degeneracy, its 2 eigenvalues λ_1, λ_2 should be different and recalling the property of unitary

matrices for which $\left|\det\left(\hat{U}\right)\right| = 1$, it is reasonable to pick 1 and -1. In this way the $\hat{Z}$ gate is defined:

$$\hat{Z} = \begin{pmatrix} \lambda_1 & 0 \\ 0 & \lambda_2 \end{pmatrix} = \begin{pmatrix} 1 & 0 \\ 0 & -1 \end{pmatrix} \tag{2.10}$$

When applied to a state, it acts as a phase flipper for $|1\rangle$.

$$\hat{Z}|\psi\rangle = \alpha|0\rangle - \beta|1\rangle \tag{2.11}$$

Its unitariety is easily checked since $\hat{Z}^\dagger = \hat{Z}$ and $\hat{Z}\hat{Z} = \mathbb{I}$.

What about classical gates?
Consider for example the classical `NOT` gate, if we want to have a quantum counterpart we should seek for a unitary operator that brings $|0\rangle \to |1\rangle$ and $|1\rangle \to |0\rangle$. It is possible to build such operator with Dirac notation by applying the $|\psi_{\text{end}}\rangle\langle\psi_{\text{start}}|$ concept on all input states:

$$\hat{X} = |0\rangle\langle 1| + |1\rangle\langle 0| = \begin{pmatrix} 0 & 1 \\ 1 & 0 \end{pmatrix} \tag{2.12}$$

its unitariety is easily checked since, akin to $\hat{Z}$, $\hat{X}^\dagger = \hat{X}$ and $\hat{X}^\dagger\hat{X} = \mathbb{I}$.

It is worth taking a moment to appreciate the difference between applying $\hat{X}$ then $\hat{Z}$ or the opposite.

$$\hat{X}\hat{Z}|\psi\rangle = \hat{X}(\alpha|0\rangle - \beta|1\rangle) = -\beta|0\rangle + \alpha|1\rangle \tag{2.13}$$

$$\hat{Z}\hat{X}|\psi\rangle = \hat{Z}(\beta|0\rangle + \alpha|1\rangle) = \beta|0\rangle - \alpha|1\rangle \tag{2.14}$$

Therefore $\hat{X}\hat{Z}|\psi\rangle = -\hat{Z}\hat{X}|\psi\rangle$. Starting from these two a third gate can be defined: $\hat{Y} = i\hat{X}\hat{Z}$. All of them are Hermitian and Unitary and correspond to 180° rotations in the Bloch sphere around their axis. They are also denoted as σ_i where i is the axis they refer to and they may be also found without their hat:

$$X = \hat{X} = \hat{\sigma}_x = \sigma_x \tag{2.15}$$

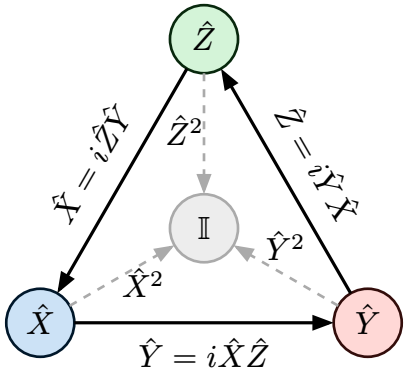


Figure 3: The Pauli algebra cycle, directed edges show cyclic permutations.

Another very important single qubit gate is the Hadamard gate $\hat{H}$, which creates a uniform superposition of $|0\rangle$ and $|1\rangle$, specifically it maps: $|0\rangle \to |+\rangle$ and $|1\rangle \to |-\rangle$. This transformation can be also seen as a rotation on the $x + z$ axis.

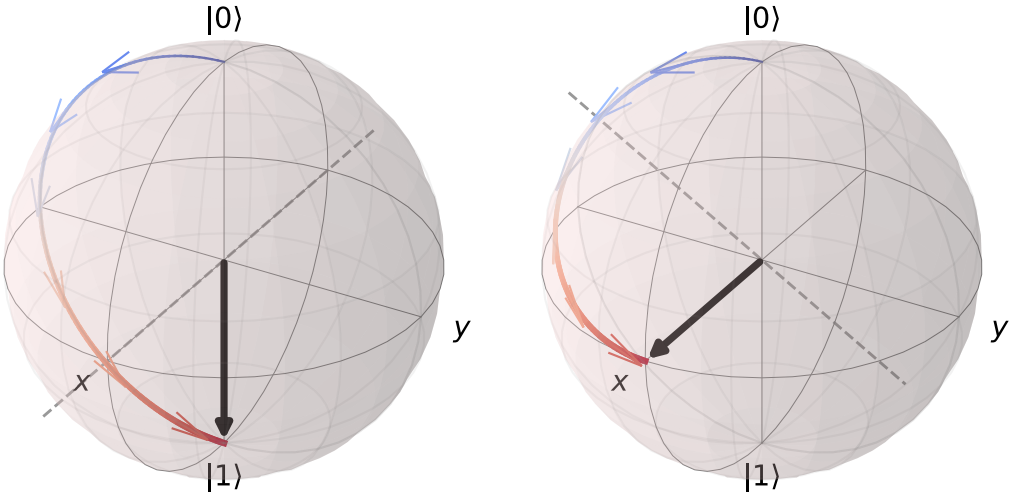


Figure 4: Representation on the Bloch sphere of the transformations $\hat{X}|0\rangle$ (left) and $\hat{H}|0\rangle$ (right)

All single qubit gates can be visualized as a rotation of the state on the Bloch sphere (technically speaking, $\mathrm{SU}(2)$ is locally isomorphic to $\mathrm{SO}(3)$).

For multi-qubit systems, quantum gates need to operate in a bigger vector space: Eq. (2.9) tells that for n qubits (therefore, for states embedded in a 2^n Hilbert space) evolution of the states are dictated by a unitary matrix of dimension $2^n \times 2^n$. Starting from single qubit gates, the evolution gate is simply constructed as the tensor product ($\otimes$) of the two unitary matrices. When dealing with the numerical matrices (instead of the mathematical concept of a matrix) this is called *Kronecker product*.
As a shorthand notation when combining single qubit gates, identity matrix is often omitted. It is also useful to label as pedices the qubit indeces on which gates are acting, to build some intuition let us see the case $\hat{X}_1\hat{Z}_2$.
Starting from independent qubits (A, B) evolving in an independent fashion with an $\hat{X}$ gate on the first and $\hat{Z}$ on the second:

$$\begin{cases} |\psi_{\mathrm{A},2}\rangle = \hat{X}|\psi_{\mathrm{A},1}\rangle \\ |\psi_{\mathrm{B},2}\rangle = \hat{Z}|\psi_{\mathrm{A,B}}\rangle \end{cases} \tag{2.16}$$

It is always possible to write the composite state $|\psi\rangle = |\psi_\mathrm{A}\psi_\mathrm{B}\rangle$.
Since its components are evolving independently, the unitary matrix describing the evolution of $|\psi\rangle$ must describe the 4 coefficients as the combination of their independent evolution. Coefficients for the first qubit are swapped, the sign of the second is flipped when the state is $|1\rangle$.

$$|\psi_1\rangle = \begin{pmatrix} a_0b_0 \\ a_0b_1 \\ a_1b_0 \\ a_1b_1 \end{pmatrix} \xrightarrow{\hat{X}_1\hat{Z}_2} |\psi_2\rangle = \begin{pmatrix} a_1b_0 \\ -a_1b_1 \\ a_0b_0 \\ -a_0b_1 \end{pmatrix} \tag{2.17}$$

By analizing where each basis vector moved after the evolution, it is possible to build the matrix describing it. It can be noticed that, if written by blocks, such matrix looks like $\hat{Z}$ on the antidiagonals.

$$\begin{pmatrix} 0 & 0 & 1 & 0 \\ 0 & 0 & 0 & -1 \\ 1 & 0 & 0 & 0 \\ 0 & -1 & 0 & 0 \end{pmatrix} = \begin{pmatrix} 0 & \hat{Z} \\ \hat{Z} & 0 \end{pmatrix} \tag{2.18}$$

This second form looks like an $\hat{X}$ gate but instead of ones, it has $\hat{Z}$ gates. It is really the case: entries of the $\hat{X}$ gates are taken and multiplied with a $\hat{Z}$

matrix, in this way they give birth to a 4×4 matrix.
This example also shows how the Kronecker product is evaluated.

$$\hat{X} \otimes \hat{Z} = \begin{pmatrix} x_{1,1}\hat{Z} & x_{1,2}\hat{Z} \\ x_{2,1}\hat{Z} & x_{2,2}\hat{Z} \end{pmatrix} = \begin{pmatrix} x_{1,1}z_{1,1} & x_{1,1}z_{1,2} & x_{1,2}z_{1,1} & x_{1,2}z_{1,2} \\ x_{1,1}z_{2,1} & x_{1,1}z_{2,2} & x_{1,2}z_{2,1} & x_{1,2}z_{2,2} \\ x_{2,1}z_{1,1} & x_{2,1}z_{1,2} & x_{2,2}z_{1,1} & x_{2,2}z_{1,2} \\ x_{2,1}z_{2,1} & x_{2,1}z_{2,2} & x_{2,2}z_{2,1} & x_{2,2}z_{2,2} \end{pmatrix} \tag{2.19}$$

Any succession of quantum gates applied to specific qubits is commonly called a *quantum circuit* and diagrams are built to describe them. Such diagrams are matrix-like shaped with lines referring to qubits and columns representing discrete time steps. Classical bits are also used, at least to store measurement results, and indicated with two closeby lines.

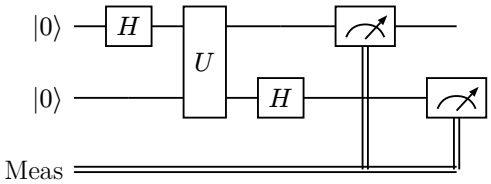


Figure 5: Representation of a quantum circuit

In Figure 5 a simple quantum circuit is reported: Hadamard gate is applied to qubit 0 (first row) followed by a generic 2-qubit unitary operation which is applied to the two qubits, then an Hadamard gate is applied to qubit 1 (second row) and finally the state is measured on the z basis.

Not all 2-qubit quantum gates can be obtained by combining single qubit ones. Such missing gates represent interacting evolutions.

Among them, *controlled operations* are rather useful and important examples: suppose to apply a general transformation U on the second qubit only if the first is in state $|1\rangle$ (and nothing if in state $|0\rangle$). Dirac notation and Kronecker product can be combined to understand how to build such operations: $|1\rangle\langle 1| \otimes \hat{U} + |0\rangle\langle 0| \otimes \mathbb{I}$.
In matrix form this looks like $\begin{pmatrix} \mathbb{I} & 0 \\ 0 & 0 \end{pmatrix} + \begin{pmatrix} 0 & 0 \\ 0 & \hat{U} \end{pmatrix} = \begin{pmatrix} \mathbb{I} & 0 \\ 0 & \hat{U} \end{pmatrix} = \begin{pmatrix} 1 & \cdot & \cdot & \cdot \\ \cdot & 1 & \cdot & \cdot \\ \cdot & \cdot & u_{1,1} & u_{1,2} \\ \cdot & \cdot & u_{2,1} & u_{2,2} \end{pmatrix}$,
here dots are used instead of zeroes only to simplify the notation.

Fundamental examples of this kind of operations are: CX (or CNOT) and CZ, those two gates are not only intuitive but also very close to what state of the art quantum hardware can perform.

It would be tempting to look for an analogous to classical logic gates as `OR, AND, XOR, ...` but one should keep in mind how at least reversibility must be respected in unitary evolutions. Consider the `XOR`, classically it is a perfect *bit-mixer*: by knowing only the result, there is no information gain on the input values, it would be equivalent to toss a fair coin and assign the value to one of the bits. Some information is still present though, output of that gate is `1` (`0`) only if the two input bits are different (equal). If in addition to the output, one of the two input bits were carried out, information would have been been conserved.

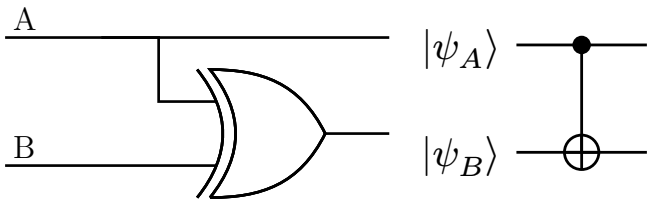


Figure 6: Left: Reversible XOR circuit, Right: CNOT circuit symbol

Such exotic `XOR` can be seen as a controlled `NOT` in which A acts as control and B as a target, and this is exactly the classical counterpart of the `CNOT` quantum gate. To be fair, this was a lucky example: among classical gates it is the only non trivial one[2] that can be made reversible by simply bringing out one line (since its output are two `0`s and two `1`s, so that all 4 inputs can be reconstructed by having 2 bits). To overcome this limitation an extra line, referred as an *ancilla*, is also employed bringing the fan-out to 3. As an example the `AND` gate can be made reversible by adding an ancilla bit, in which the result of the operation can be stored. Unfortunately, by simply having the result in one line it would not be possible to have a reversible gate since the whole input space cannot be spanned if even a single line is not balanced (`0` for half of the inputs and `1` for the remaining ones). Here the ancilla plays a fundamental role: by simply adding the third bit and xoring it with the ouput of the `AND`, the

[2] Also identity, `NOT` and logical equivalent to the `XOR` such as `XNOR`. This is strictly linked to the linear nature of such operations.

line becomes balanced. Moreover, it can be used to negate the result allowing to use such gate both as a `AND` and as a `NAND`. Such gate is very important in classical computing as it forms a universal set. Alternatively, it can be seen as a `NOT` operation applied on the ancilla, only if the two control bits are `1`. Again, this is an excelent starting point to build its quantum counterpart, $\hat{X}$, only if the first two qubits are $|11\rangle$ and nothing in the remaining cases:

$$|11\rangle\langle 11| \otimes \hat{X} + |10\rangle\langle 10| \otimes \mathbb{I} + |01\rangle\langle 01| \otimes \mathbb{I} + |00\rangle\langle 00| \otimes \mathbb{I} \tag{2.20}$$

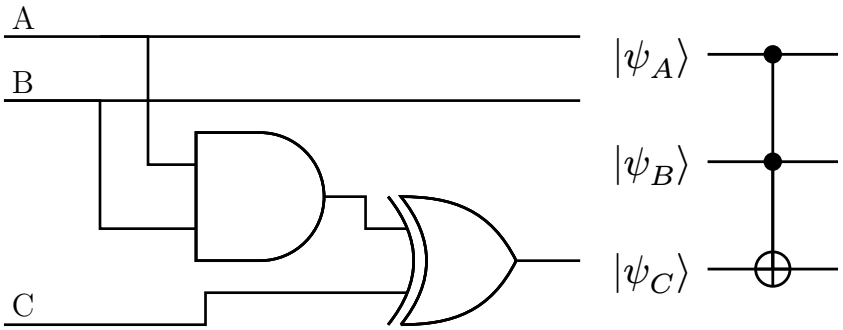


Figure 7: Left: Reversible NAND circuit, Right: Toffoli circuit symbol

2.3. Universal computation and Clifford Gates

Akin to classical computers, a quantum computer must be able to perform any desirable elaboration of the input. For an n-qubit system (with $N = 2^n$ states) the set of all unitary matrices (describing all its possible evolutions), is

$$U(N) = \left\{\hat{U} \in \mathbb{C}^{N\times N} : \hat{U}^\dagger \hat{U} = \hat{U}\hat{U}^\dagger = \mathbb{I}\right\} \tag{2.21}$$

All matrices $\hat{U} \in U(N)$ have $\det\left(\hat{U}\right) = e^{i\theta}$, but only a fraction of them have $\det\left(\hat{U}\right) = 1$, those are part of a special group of unitary matrices called $\mathrm{SU}(N)$, describing evolutions disregarding any global phase factor, undetectable by measurements.

State of the art hardware employed in digital quantum computing poses major limits: application of gates is imperfect, interactions among more qubits are difficult to be perfectly executed or even achieved causing limitations in most of the systems to 2-qubit gates. The employed mathematical framework should be empowered to overcome some limitations.

Classically, many gates exist and may be devised but it resulted technologically convenient to develop and deeply optimize only a few of them, which are combined to build any desired combination.

A remarkable result is that every $\hat{U} \in \mathrm{SU}(2^n)$ can be decomposed into elements from $\mathrm{SU}(2^{n-1})$ and their tensor product. [6]
This procedure is also known as KAK decomposition, following the form in which the unitary is decomposed: $\hat{U} = K_1 A K_2$. To better grasp how powerful this is, let us have a quick look at a small and superficial example. Suppose a 3-qubit gate $\hat{U}_{3q} \in \mathrm{SU}(8)$, acting on $|\psi_A\psi_B\psi_C\rangle$. The goal here is to reduce its complexity to the leftmost part of the system by having a generic $\hat{U} \in \mathrm{SU}(4)$ acting on $|\psi_a\psi_B\rangle$ and some easier gates *linking* $|\psi_B\rangle$ and $|\psi_C\rangle$, usually CNOTs. KAK decomposition allows to write $\hat{U}_{3q} = K_1 A K_2$ where $K_1, K_2 \in \mathrm{SU}(8)$ are controlled unitaries $\hat{U} \in \mathrm{SU}(4)$ for which the control is $|\psi_C\rangle$, as desired. The core A matrix is an exponential of a weighted sum of specific products of single qubit gates acting on the three qubits

$$A = e^{-i\sum c_i \hat{\sigma}_i \otimes \hat{\sigma}_i \otimes \hat{\sigma}_i} \tag{2.22}$$

which is good but could still require a 3 qubit operation (e.g. $\hat{X}_1\hat{Y}_2\hat{Z}_3)^3$, this can be further simplified by another powerful tool known as *CNOT staircase* or *Pauli gadget*: all Pauli rotations are moved to a common basis by local operations on the qubits (using the computational basis for the previous example allows for the third qubit to remain untouched while for the first and second qubits it respectively requires that $\hat{X} \to \hat{R}_y(-\frac{\pi}{2})\hat{X}$ and $\hat{Y} \to \hat{R}_x(\frac{\pi}{2})\hat{Y}$). Now it is sufficient to propagate the parity with a staircase of CNOTs down to a target qubit on which the rotation $R_{z(2c_i)}$ is performed (coefficient c_i in the A matrix of KAK decomposition) and undo the computation: apply the CNOT staircase and bring back the qubits in their intended base.

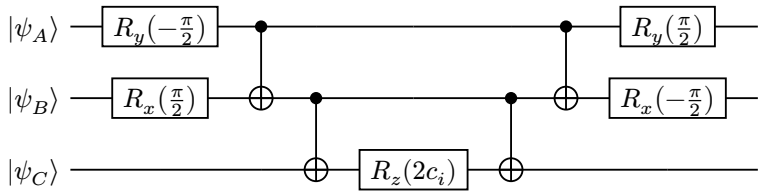


Figure 8: Representation of the $e^{-ic_i\hat{X}_1\hat{Y}_2\hat{Z}_3}$ transformation

It is worth highlighting the fundamental point: it is possible to exactly decompose an arbitrary gate $\hat{U} \in \mathrm{SU}(2^n)$ into 1-qubit gates and CNOTs, this is a great step towards our universal set of gates.

Let us now seek for a set of gates that can be used to work in $\mathrm{SU}(2)$. The Pauli group for 1 qubit is defined as the set of Pauli matrices, combined with 90° phase factors:

$$\mathcal{P}_1 = \left\{\pm\mathbb{I}, \pm i\mathbb{I}, \pm\hat{X}, \pm i\hat{X}, \pm\hat{Y}, \pm i\hat{X}, \pm\hat{Z} \pm i\hat{Z}\right\} \tag{2.23}$$

or, more generally:

$$\mathcal{P}_n = \left\{cP_1 \otimes \cdots \otimes P_n : c \in \{\pm 1, \pm i\}, P_i \in \left\{\mathbb{I}, \hat{X}, \hat{Y}, \hat{Z}\right\}\right\} \tag{2.24}$$

The issue concerning this group is that, starting from any state, only its orthogonal can be visited, with some phase difference at most. A nice property of elements in $\mathcal{P}_n$ is that either they commute or they anti-commute, specifically

[3]This combination is not part of the ones possibly appearing in the A matrix, but it shows how all Pauli gates can be implemented.

depending on the number of commuting gates, qubit by qubit; this property is rather useful when dealing with quantum error correction.

The next step is adding the possibility to span the eigenstates of Pauli operators:

$$\{|0\rangle, |1\rangle, |+\rangle, |-\rangle, |L\rangle, |R\rangle\} \tag{2.25}$$

The same problem can be posed by looking for a change of basis in which the 3 axis are shuffled.

Let us take a closer look to all the possible changes of basis mapping elements from the 1-qubit Pauli group into elements of the same group.

$$\mathcal{C}_1 = \left\{\hat{U} \in \mathrm{U}(2) : UPU^\dagger = P' \text{ with } P, P' \in \mathcal{P}_1\right\} \tag{2.26}$$

It is straightforwardly generalized to the n-qubit by working in $U(2^n)$ and with $\mathcal{P}_n$. Formally this is called the *Normalizer* of the Pauli group in $\hat{U}$. Defined in this way it has uncountably infinite elements, since also a phase difference $e^{i\theta}$ generates a new possible element of $\mathcal{C}_n$. Since in quantum mechanics a global phase has no measurable effects, the very core of $\mathcal{C}_1$ can be obtained by aggregating gates differing only by a phase factor, corresponding to a set that has only 24 elements.

Beside the identity matrix, 3 types of rotations can be visualized:

- Around the axis, $\pm 90°$ and $180°$: 3 angles $\times$ 3 rotations = 9 gates.
- Around a combination of two axis, $180°$: 6 combinations of axis.
- Around a combination of the three axis, $\pm 120°$: 2 angles $\times$ 4 combinations = 8 gates.

The single-qubit Clifford group is perfectly isomorphic to the rotational symmetries of a cube inscribed in the Bloch sphere.

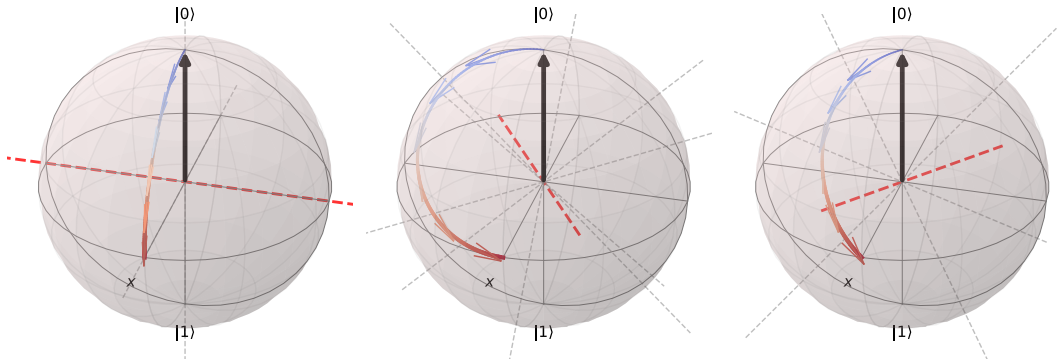


Figure 9: Examples of gates from $\mathcal{C}_1$ mapping $|0\rangle \to |+\rangle$. Left: 90° around y. Center: 180° around $x + z$. Right: 120° around $x + y + z$.

This set of gates, beside not being able to fully span the $U(2)$ set, would not offer any quantum advantage because algorithms composed only of Clifford gates can be classically simulated in polynomial times. [7]

Among these 24, how many gates are really needed? To answer this question, in this context, it is useful to define a 90° rotation gate, specifically around z : $\hat{S}$ axis. It is also called square root gate since $\hat{S}^2 = \hat{Z}$.

$$\hat{S} = \begin{pmatrix} 1 & 0 \\ 0 & e^{i\frac{\pi}{2}} \end{pmatrix} = \begin{pmatrix} 1 & 0 \\ 0 & i \end{pmatrix} \tag{2.27}$$

Suppose starting in $|0\rangle$ and wanting to visit any state on the equator: it is sufficient to apply an $\hat{H}$ gate to move on $|+\rangle$ and then rotate by 90° with $\hat{S}$, furthermore when visiting $|-\rangle$ if an $\hat{H}$ gate is applied the state ends in $|1\rangle$. Moving the computational basis to the $\{|+\rangle, |-\rangle\}$ or to the $\{|R\rangle, |L\rangle\}$ is done by applying $\hat{H}$ and eventually rotating it again with $\hat{S}$. It can be rigorously proved that they are enough to generate all $\mathcal{C}_1$. When scaling up to 2-qubits, it is sufficient to add a CNOT (or, equivalently a CZ) to generate $\mathcal{C}_2$, since it allows to distribute the Pauli operators. Generalizing to the n-qubit case, no other gate is required to build all the possible elements in the Clifford set.[7]

Recovering the whole $U(2^n)$ starting from $\mathcal{C}_n$ may seem a long journey, indeed it requires 1 new gate and a theorem.

Recalling the idea of rotating along the equator, let us define an even smaller rotation around z axis. Akin to the definition of $\hat{S}$ it is possible to define a new gate $\hat{T}$. This latter gate when applied twice should perform the $\hat{S}$ gate: $\hat{T}^2 = \hat{S}$.

$$\hat{T} = \begin{pmatrix} 1 & 0 \\ 0 & e^{i\frac{\pi}{4}} \end{pmatrix} \tag{2.28}$$

By simply adding this gate to the Clifford group, it is possible to efficiently approximate any arbitrary unitary evolution. [8] To better appreciate how powerful this is, by picking an error ϵ the number of gates required to approximate it scales as $\log^c\left(\frac{1}{\epsilon}\right)$ where c is a constant depending on the actual approximation algorithm. To grasp an idea of the scale, c can be around 4.

Summarizing, it is possible to construct any arbitrary quantum gate for n qubits by decomposing it with KAK decomposition up to single qubit gates and CNOTs, and then approximating such single qubit gates merely with $\hat{H}$ and $\hat{T}$. This is the very smallest set of quantum gates that should be implemented to achieve universal quantum computation: $\left\{\hat{H}, \hat{T}, \text{CNOT}\right\}$.
Although this is the minimal number of gates, it is often also included the $\hat{S}$ gate because $\hat{T}$ is *expensive* in terms of error correcting codes. This section is intended from the circuital standpoint, hardware implementation widely differ, offering some equivalent variations.
For example a PRX gate is defined as the combination of an arbitrary rotation around x axis and an added phase difference. This gate is very versatile having 2 continuous degrees of freedom, but for the circuital point of view it is more convenient to think of it as a combination of gates from $\left\{\hat{H}, \hat{S}, \hat{T}\right\}$.

$$\begin{aligned} \text{PRX}(\theta, \phi) &= R_z(\phi) R_x(\theta) R_z(-\phi) \\ &= \begin{pmatrix} e^{-i\frac{\phi}{2}} & 0 \\ 0 & e^{i\frac{\phi}{2}} \end{pmatrix} \begin{pmatrix} \cos\left(\frac{\theta}{2}\right) & -i\sin\left(\frac{\theta}{2}\right) \\ -i\sin\left(\frac{\theta}{2}\right) & \cos\left(\frac{\theta}{2}\right) \end{pmatrix} \begin{pmatrix} e^{i\frac{\phi}{2}} & 0 \\ 0 & e^{-i\frac{\phi}{2}} \end{pmatrix} \\ &= \begin{pmatrix} \cos\left(\frac{\theta}{2}\right) & e^{-i(\phi+\frac{\pi}{2})}\sin\left(\frac{\theta}{2}\right) \\ e^{i(\phi-\frac{\pi}{2})}\sin\left(\frac{\theta}{2}\right) & \cos\left(\frac{\theta}{2}\right) \end{pmatrix} \end{aligned} \tag{2.29}$$

A brief recap of some widely used quantum gates is reported in Table 1 and Table 2.

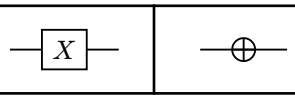
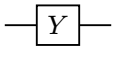
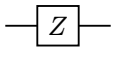
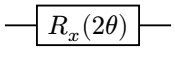
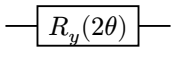
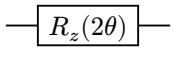
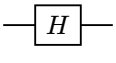
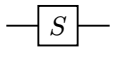
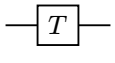
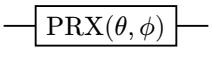
Name	Symbol(s)	Matrix
Pauli $\hat{X}$, $\hat{\sigma}_x$		$\begin{pmatrix} 0 & 1 \\ 1 & 0 \end{pmatrix}$
Pauli $\hat{Y}$, $\hat{\sigma}_y$		$\begin{pmatrix} 0 & -i \\ i & 0 \end{pmatrix}$
Pauli $\hat{Z}$, $\hat{\sigma}_z$		$\begin{pmatrix} 1 & 0 \\ 0 & -1 \end{pmatrix}$
$\hat{R}_x(2\theta)$		$\begin{pmatrix} \cos(\theta) & -i\sin(\theta) \\ -i\sin(\theta) & \cos(\theta) \end{pmatrix}$
$\hat{R}_y(2\theta)$		$\begin{pmatrix} \cos(\theta) & -\sin(\theta) \\ \sin(\theta) & \cos(\theta) \end{pmatrix}$
$\hat{R}_z(2\theta)$		$\begin{pmatrix} e^{-i\theta} & 0 \\ 0 & e^{i\theta} \end{pmatrix}$
Hadamard $\hat{H}$		$\frac{1}{\sqrt{2}}\begin{pmatrix} 1 & 1 \\ 1 & -1 \end{pmatrix}$
Square root $\hat{S}$		$\begin{pmatrix} 1 & 0 \\ 0 & i \end{pmatrix}$
$\hat{T}$		$\begin{pmatrix} 1 & 0 \\ 0 & e^{i\frac{\pi}{4}} \end{pmatrix}$
PRX		$\begin{pmatrix} \cos\left(\frac{\phi}{2}\right) & -ie^{-i\theta}\sin\left(\frac{\phi}{2}\right) \\ -ie^{i\theta}\sin\left(\frac{\phi}{2}\right) & \cos\left(\frac{\phi}{2}\right) \end{pmatrix}$

Table 1: Some relevant 1-qubit quantum gates

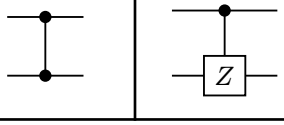
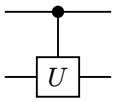
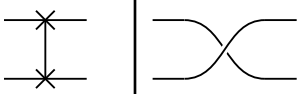
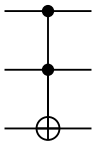
Name	**Symbol(s)**	**Matrix**
CNOT, CX		$\begin{pmatrix} 1 & \cdot & \cdot & \cdot \\ \cdot & 1 & \cdot & \cdot \\ \cdot & \cdot & \cdot & 1 \\ \cdot & \cdot & 1 & \cdot \end{pmatrix}$
CZ		$\begin{pmatrix} 1 & \cdot & \cdot & \cdot \\ \cdot & 1 & \cdot & \cdot \\ \cdot & \cdot & 1 & \cdot \\ \cdot & \cdot & \cdot & -1 \end{pmatrix}$
Control unitary		$\begin{pmatrix} 1 & \cdot & \cdot & \cdot \\ \cdot & 1 & \cdot & \cdot \\ \cdot & \cdot & u_{1,1} & u_{1,2} \\ \cdot & \cdot & u_{2,1} & u_{2,2} \end{pmatrix}$
SWAP		$\begin{pmatrix} 1 & \cdot & \cdot & \cdot \\ \cdot & \cdot & 1 & \cdot \\ \cdot & 1 & \cdot & \cdot \\ \cdot & \cdot & \cdot & 1 \end{pmatrix}$
Toffoli		$\begin{pmatrix} 1 & \cdot & \cdot & \cdot & \cdot & \cdot & \cdot & \cdot \\ \cdot & 1 & \cdot & \cdot & \cdot & \cdot & \cdot & \cdot \\ \cdot & \cdot & 1 & \cdot & \cdot & \cdot & \cdot & \cdot \\ \cdot & \cdot & \cdot & 1 & \cdot & \cdot & \cdot & \cdot \\ \cdot & \cdot & \cdot & \cdot & 1 & \cdot & \cdot & \cdot \\ \cdot & \cdot & \cdot & \cdot & \cdot & 1 & \cdot & \cdot \\ \cdot & \cdot & \cdot & \cdot & \cdot & \cdot & \cdot & 1 \\ \cdot & \cdot & \cdot & \cdot & \cdot & \cdot & 1 & \cdot \end{pmatrix}$

Table 2: Some relevant quantum gates

2.4. Density Matrix and Kraus Formalism

Let us now turn to more complex scenarios, in which either the state is not precisely known or the applied gate is not perfect. In this context quantum mechanics borrows some tools from statistical mechanics, most notably the density matrix ρ. Within this alternative formulation, states are conceptually embedded in the density matrix instead of a vector.

Let us consider a system whose state is known only probabilistically: it is in state $|\psi_i\rangle$ with probability p_i. This set $\{p_i, |\psi_i\rangle\}$ is referred to as an ensemble of pure states, and the density operator describing this system is

$$\rho = \sum p_i |\psi_i\rangle\langle\psi_i| \tag{2.30}$$

For a qubit in the general known state $|\psi\rangle = \alpha|0\rangle + \beta|1\rangle$ its density matrix representation is $\rho = |\psi\rangle\langle\psi| = \begin{pmatrix} |\alpha|^2 & \alpha\beta^* \\ \alpha^*\beta & |\beta|^2 \end{pmatrix}$.

Suppose a perfect unitary is applied to the system, pure states would evolve according to Eq. (2.9) therefore their mixture evolves as

$$\rho = \sum p_i |\psi_i\rangle\langle\psi_i| \xrightarrow{\hat{U}} \sum p_i \hat{U}|\psi_i\rangle\langle\psi_i|\hat{U}^\dagger = \hat{U}\rho\hat{U}^\dagger \tag{2.31}$$

A very important property directly follows from the probabilistic definition of the operator: its trace is 1.

Starting from an example to show the difference between a mixture of states and a superposition of states, suppose a device that randomly outputs a state between $|0\rangle$ and $|1\rangle$ in a balanced way (50% each). Such state is written as

$$\rho = \frac{1}{2}|0\rangle\langle 0| + \frac{1}{2}|1\rangle\langle 1| = \frac{1}{2}\begin{pmatrix} 1 & 0 \\ 0 & 1 \end{pmatrix} = \frac{\mathbb{I}}{2} \tag{2.32}$$

This state evolves both as a $|0\rangle$ and a $|1\rangle$ would, but is not a superposition of them. In fact, consider the $|+\rangle$ state, its density matrix representation would be $\rho = |+\rangle\langle+| = \frac{1}{2}\begin{pmatrix} 1 & 1 \\ 1 & 1 \end{pmatrix}$. Notice how in this case, elements off diagonal appeared and the two matrices differ.

A *pure state* (i.e. a perfectly known quantum state) can be discerned by a mixed one by evaluating $\mathrm{Tr}(\rho^2)$ (in the previous example 0.5 for the mixture and 1 for $|+\rangle\langle+|$).

A way to better visualize this concept is by noticing that all the 1-qubit density matrices can be written as weighted combinations of Pauli matrices:

$$\rho = \frac{1}{2}\big(\mathbb{I} + r_x\hat{\sigma}_x + r_y\hat{\sigma}_y + r_z\hat{\sigma}_z\big) = \frac{1}{2}(\mathbb{I} + \overline{\boldsymbol{r}} \cdot \overline{\boldsymbol{\sigma}}) \tag{2.33}$$

Where $\overline{\boldsymbol{\sigma}} = \big(\hat{\sigma}_x, \hat{\sigma}_y, \hat{\sigma}_z\big)$ is a vector containing Pauli operators in this specific order and $\overline{\boldsymbol{r}} = \big(r_x, r_y, r_z\big)$ is a real valued vector whose components turn out to be expected values when observing the state in each of $\{x, y, z\}$ basis.
This way of thinking single qubit states simplifies also the evaluation of the purity since

$$\mathrm{Tr}(\rho^2) = \frac{1}{2}(1 + |\overline{\boldsymbol{r}}|^2) \tag{2.34}$$

Consequently all pure states must have $|\overline{\boldsymbol{r}}| = 1$ therefore they live on the surface of the Bloch sphere and mixed states are contracted inside of it. As a limit, a state can collapse to the center of the sphere ($|\overline{\boldsymbol{r}}|^2 = 0$) therefore $\rho = \frac{1}{2}\mathbb{I}$, this is also referred as a *maximally mixed state*.

To better appreciate how this framework extends the state vector formalism, let us consider an entangled state: a particle in system A is brought into interaction with a particle in system B in such a way that their state is an entangled one.
Suppose it corresponds to the previously described state $|\psi\rangle = \frac{|00\rangle + |11\rangle}{\sqrt{2}}$ that is a pure state represented by

$$\rho = \frac{1}{2}(|00\rangle + |11\rangle(\langle 00| + \langle 11|) = \frac{1}{2}\begin{pmatrix} 1 & \cdot & \cdot & 1 \\ \cdot & \cdot & \cdot & \cdot \\ \cdot & \cdot & \cdot & \cdot \\ 1 & \cdot & \cdot & 1 \end{pmatrix} \tag{2.35}$$

But now there is the possibility to investigate what can be observed by looking only at the subsystem A, ignoring B. This is achieved with the partial trace: the density matrix is evaluated at all eigenstates not of interest. In this case simply $|0\rangle_B$ and $|1\rangle_B$.

$$\rho_A = \mathrm{Tr}_B(\rho) = \frac{1}{2}\begin{pmatrix} 1 & 0 \\ 0 & 1 \end{pmatrix} = \frac{\mathbb{I}}{2} \tag{2.36}$$

This is the very same state previously described, an equal mixture of computational basis. This example shows how an entangled state, even when pure, can be a mixed state when observed from the perspective of a single subsystem.

Within this framework it is possible to describe evolution of the qubit when it cannot be considered any more a closed system (e.g. because of interactions with its surroundings) and the trick is rather easy: an environment is defined and coupled to the system; hence, together they form a closed system whose evolution can be described by a unitary operator.
Let us consider a qubit as the system of interest $|\psi\rangle_S$ and an environment described as a 2 level system in its ground state $|\psi\rangle_E = |0\rangle$. The composite system is

$$|\psi\rangle = |\psi\rangle_S |\psi\rangle_E = |\psi\rangle_S |0\rangle \tag{2.37}$$

Prepared in this way it is the independent combination of two closed systems in pure states, remaining a pure state. Let us create its unitary evolution according to what most commonly happens in real systems. When the system is in its ground state, no energy can be transferred so

$$\hat{U}(|0\rangle_S |0\rangle_E) = |0\rangle_S |0\rangle_E \tag{2.38}$$

Then, the phisically unavoidable interaction between the system and the environment may lead the energy of the qubit be dissipated to the environment (with a probability γ) or kept by the qubit $(1-\gamma)$:

$$\hat{U}(|1\rangle_S |0\rangle_E) = \sqrt{\gamma}|0\rangle_S |1\rangle_E + \sqrt{1-\gamma}|1\rangle_S |0\rangle_E \tag{2.39}$$

Even though we discard by construction the possibility for the environment to start in an excited state, to build the unitary operator we need to discuss what would happen also in such cases. To ensure a reversible evolution, the relaxation process should be able to happen also in the opposite direction, with the same probability:

$$\hat{U}(|0\rangle_S |1\rangle_E) = -\sqrt{\gamma}|1\rangle_S |0\rangle_E + \sqrt{1-\gamma}|0\rangle_S |1\rangle_E \tag{2.40}$$

where a - sign is necessary to ensure phase conservation. Finally for the fully excited system

$$\hat{U}(|1\rangle_S |1\rangle_E) = |0\rangle_S |1\rangle_E \tag{2.41}$$

So the unitary evolution is built as

$$\hat{U} = \begin{pmatrix} 1 & \cdot & \cdot & \cdot \\ \cdot & \sqrt{1-\gamma} & \sqrt{\gamma} & \cdot \\ \cdot & -\sqrt{\gamma} & \sqrt{1-\gamma} & \cdot \\ \cdot & \cdot & \cdot & 1 \end{pmatrix} \tag{2.42}$$

Let us finally evaluate this interaction starting with $|\psi_0\rangle = \begin{pmatrix} \alpha \\ 0 \\ \beta \\ 0 \end{pmatrix}$

$$|\psi_1\rangle = \hat{U}|\psi_0\rangle = \begin{pmatrix} \alpha \\ \beta\sqrt{\gamma} \\ \beta\sqrt{1-\gamma} \\ 0 \end{pmatrix} \tag{2.43}$$

In this model the γ parameter, dictating the probability of relaxation, evolves in time starting from the "initialization" of the experiment:

$$\gamma(t) = 1 - e^{-t/T_1} \tag{2.44}$$

Here a T_1 parameter is defined: it is connected to real world dynamics and corresponds to the *characteristic time* of this process for a qubit. Moreover this model, known as *amplitude damping* does not fully describe the whole interaction of a qubit with its thermal bath, but it is a very good approximation of what really happens in most of the hardwares.

Up to now no density matrix was required since the whole system was assumed as closed (with the addition of an ancilla qubit as environment) and remained in a pure state.
But what could be seen by simply working with the qubit subsystem? The system cannot be factorized so the partial trace should be evaluated:

$$\rho = |\psi_1\rangle\langle\psi_1| = \begin{pmatrix} |\alpha|^2 & \alpha^*\beta\sqrt{\gamma} & \alpha^*\beta\sqrt{1-\gamma} & 0 \\ \alpha\beta^*\sqrt{\gamma} & |\beta|^2\gamma & |\beta|^2\sqrt{\gamma(1-\gamma)} & 0 \\ \alpha\beta^*\sqrt{1-\gamma} & |\beta|^2\sqrt{\gamma(1-\gamma)} & |\beta|^2(1-\gamma) & 0 \\ 0 & 0 & 0 & 0 \end{pmatrix} \tag{2.45}$$

Therefore, by tracing out the environment

$$\rho_S = \mathrm{Tr}_E(\rho) = \begin{pmatrix} |\alpha|^2 + |\beta|^2\gamma & \alpha^*\beta\sqrt{1-\gamma} \\ \alpha\beta^*\sqrt{1-\gamma} & |\beta|^2(1-\gamma) \end{pmatrix} \tag{2.46}$$

$$\rho_S^2 = \begin{pmatrix} (|\alpha|^2 + |\beta|^2\gamma)^2 + |\alpha|^2|\beta|^2(1-\gamma) & \alpha^*\beta\sqrt{1-\gamma} \\ \alpha\beta^*\sqrt{1-\gamma} & |\alpha|^2|\beta|^2(1-\gamma) + |\beta|^4(1-\gamma)^2 \end{pmatrix} \tag{2.47}$$

$$\mathrm{Tr}\left(\rho_S^2\right) = 1 - 2\gamma|\beta|^4(1-\gamma) < 1 \tag{2.48}$$

Purity of the state is smaller than 1, indicating a mixed state.

Let us retrace this example to develop a much more powerful notation. To do so, the state shall be recast in the density matrix formalism according to Eq. (2.31)

$$\rho_1 = \hat{U}(\rho_S \otimes |0\rangle\langle 0|_E)\hat{U}^\dagger \tag{2.49}$$

Now that the whole system has evolved, to evaluate the evolution of the system of interest let us trace out the environment

$$\begin{aligned} \mathrm{Tr}_E(\rho_1) &= \langle 0|_E\hat{U}(\rho_S \otimes |0\rangle\langle 0|_E)\hat{U}^\dagger|0\rangle_E + \\ &+\langle 1|_E\hat{U}(\rho_S \otimes |0\rangle\langle 0|_E)\hat{U}^\dagger|1\rangle_E \\ &= \langle 0|_E\hat{U}|0\rangle_E\rho_S\langle 0|_E\hat{U}^\dagger|0\rangle_E + \\ &+\langle 1|_E\hat{U}|0\rangle_E\rho_S\langle 0|_E\hat{U}^\dagger|1\rangle_E \end{aligned} \tag{2.50}$$

Paying attention to the elements surrounding the density matrix, it can be noticed that they are the same block, differentiated by a adjoint operation. By defining $E_0 = \langle 0|_E\hat{U}|0\rangle_E$ and $E_1 = \langle 1|_E\hat{U}|0\rangle_E$, it follows that $E_0^\dagger = \langle 0|_E\hat{U}^\dagger|0\rangle_E$ and $E_1^\dagger = \langle 0|_E\hat{U}^\dagger|1\rangle_E$, leading to

$$\rho_{\mathrm{S},1} = \mathrm{Tr}_E(\rho_1) = E_0\rho_S E_0^\dagger + E_1\rho_S E_1^\dagger \tag{2.51}$$

In matrix form

$$E_0 = \begin{pmatrix} 1 & 0 \\ 0 & \sqrt{1-\gamma} \end{pmatrix} \qquad E_1 = \begin{pmatrix} 0 & \sqrt{\gamma} \\ 0 & 0 \end{pmatrix} \tag{2.52}$$

E_0 represents the system evolution when the environment is in the $|0\rangle$ state and E_1 represents the relaxation of the qubit to the environment, bringing the latter in the $|1\rangle$ state.
It can also be recast in the general form as

$$\mathcal{E}(\rho) = \sum E_i\rho E_i^\dagger \tag{2.53}$$

This alternative way of formulating an open system evolution is called *operator sum* representation or *Kraus* notation. By analizing the new density matrix of the system of interest after the evolution ($\rho_{S,1}$) the Pauli vector evolved as

$$\begin{cases} r_x \to r_x\sqrt{1-\gamma} \\ r_y \to r_y\sqrt{1-\gamma} \\ r_z \to r_z(1-\gamma)\gamma \end{cases} \tag{2.54}$$

So it is now possible to conceive a set of points on the Bloch sphere and see how this non unitary evolution affects them (Figure 10).

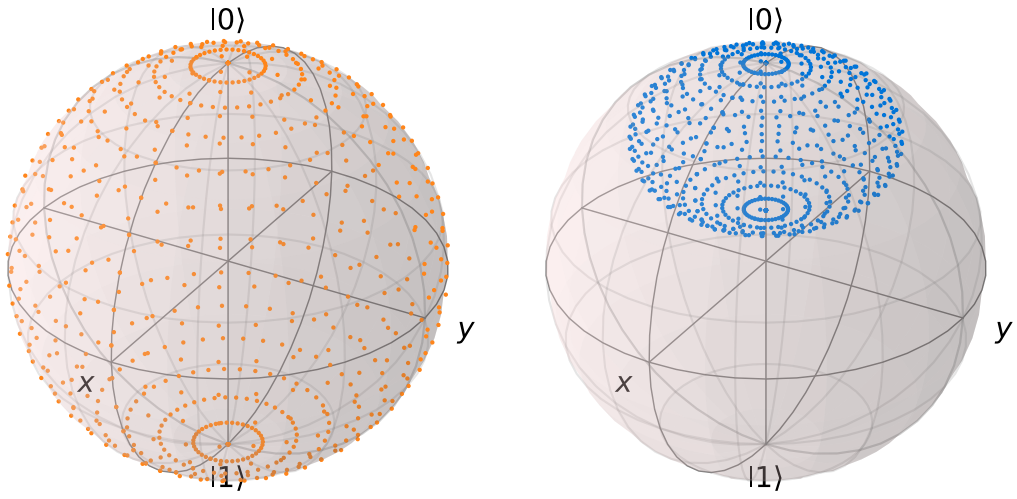


Figure 10: Left: set of states on the Bloch sphere
Right: the same set of points after a time $2T_1$, under amplitude damping.

With Kraus notation it is possible to describe the local evolution of a system even if it is entangled with some other one. It should be noticed that both E_0 and E_1 are not unitary operators, but they obey a very fundamental constraint:

$$\sum E_i^\dagger E_i = \mathbb{I} \tag{2.55}$$

2.5. Error Models

In the previous section, the model of amplitude damping describing the tendency of a qubit to relax towards the $|0\rangle$ state is briefly derived, in order to introduce Kraus notation. Now a set of very important noise models are reported, to have the mathematical tools required to describe non-idealities that state of the art hardware is dealing with.

Three macro categories of errors are described in this section:

- **Incoherent errors**: This kind of error degrades the quantum information, causing decoherence and reducing the purity of the state.
- **Coherent errors**: Unlike the incoherent ones, coherent errors still represent unitary evolution of the state but with a deviation with respect to the ideal and devised one.
- **Hardware errors**: The mathematical description of hardware specific non-idealities, which cause an incorrect interpretation of the results of quantum algorithms.

Incoherent errors	**Coherent errors**	**Hardware errors**
Bit flip	Under/over rotation	SPAM errors
Phase flip		Crosstalk
Depolarization		Leakage
Amplitude damping		

Table 3: Different types of errors

Errors may occur in a continuum of intensities and times, an exhaustive description would require the Lindblad master equation to describe evolution of open systems. For this work a simpler error model in which errors occur or do not in a Bernoullian way is sufficient. All the information regarding the time is embedded in the probability for such error to occurred. A very common technique in quantum error correction is to discretize time by considering physical gate durations and embed errors as gates in a quantum circuit.

To begin with something very familiar to computer scientists and telecommunications engineers, let us start describing the *bit flip*. As simple as it can be, this error flips the state of a qubit: it performs an $\hat{X}$ gate with a certain

probability p_x and does not alter the state with the residual probability. Its evolution can be described by the following two elements.

$$E_0 = \sqrt{p_x}\hat{X} \qquad E_1 = \sqrt{(1-p_x)}\mathbb{I} \tag{2.56}$$

Therefore the error model is

$$\mathcal{E}(\rho) = (1-p_x)\rho + p_x\hat{X}\rho\hat{X} \tag{2.57}$$

For this error, it exists a pair of states completely resistant: $|+\rangle$ and $|-\rangle$, indeed for them, flipping their α and β coefficients has no impact (global phase added for $|-\rangle$ has no observable impact). This can be also apreciated in Figure 11 where the Bloch sphere collapses on the x axis.

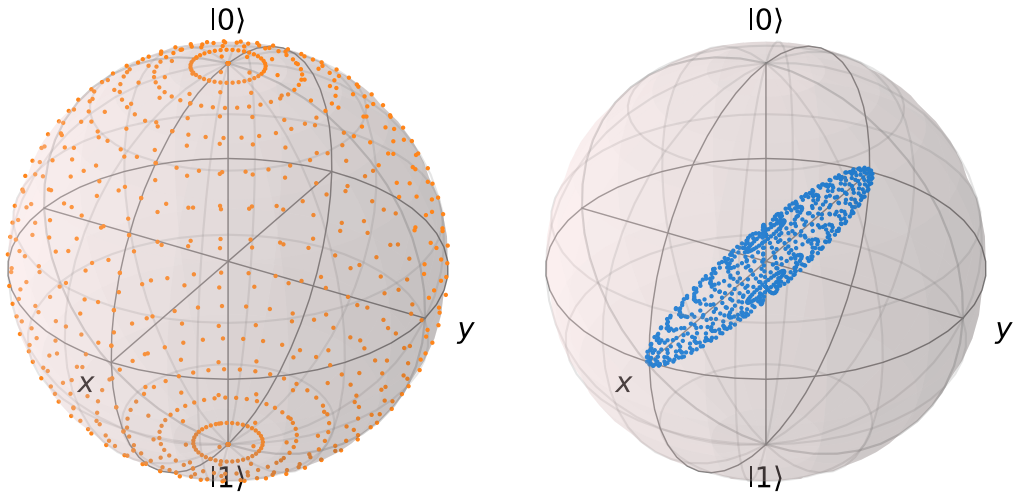


Figure 11: Evolution of a set of states on the Bloch sphere under bit flip error with $p_d \approx 86.5\%$.

Let us now describe a whole new kind of error which is conceptually the same but occurring on the second degree of freedom for qubits: the phase. This error, a *phase flip*, can be visualized as a 180° rotation around the z axis. Akin to the previous case, the error acts by flipping the phase of $|1\rangle$ with a probability p_z and leaves the state untouched otherwise.

$$E_0 = \sqrt{p_z}\hat{Z} \qquad E_1 = \sqrt{(1-p_z)}\mathbb{I} \tag{2.58}$$

Therefore,

$$\mathcal{E}(\rho) = (1 - p_z)\rho + p_z \hat{Z}\rho\hat{Z} \tag{2.59}$$

In this case, the states $|+\rangle$ and $|-\rangle$ would be the ones suffering the most since it swaps them, indeed the computational basis remains untouched, beside a global phase factor for just $|1\rangle$ that, again, has no physical effect on its own.

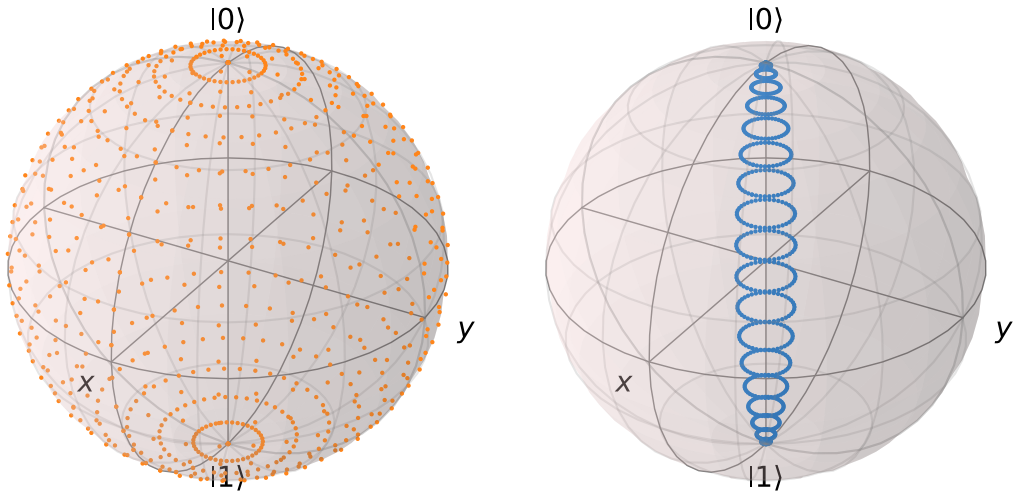


Figure 12: Evolution of a set of states on the Bloch sphere under phase flip error with $p_d \approx 86.5\%$.

This model can also be used to describe the continuous process of dephasing (i.e. loss of phase coherence), to do so the probability becomes a function of time.

$$p_z = \frac{1 - e^{-t/T_\phi}}{2} \tag{2.60}$$

Where the T_ϕ parameter is a typical parameter of qubits, representing characteristic time of the pure dephasing process.

Bit flip and phase flip are fundamentally identical, up to a change of basis; for both of them the Bloch sphere is shrunk down to an axis. By combining them, recalling commutation of Pauli operators, a $\hat{Y}$ error can be defined as a *bit-phase* flip. Another very powerful error model is the *depolarization*: this offers an isotropic degradation of information by combining the previous models. Defining again the probability of such error occuring p_d it brings the state into the maximally mixed state with such probability.

$$\begin{aligned}\mathcal{E}(\rho) &= (1-p_d)\rho + p_d\frac{\mathbb{I}}{2} \\ &= (1-p_d)\rho + \frac{p_d}{4}\left(\hat{X}\rho\hat{X} + \hat{Y}\rho\hat{Y} + \hat{Z}\rho\hat{Z} + \mathbb{I}\rho\mathbb{I}\right)\end{aligned} \tag{2.61}$$

The operator sum representation better allows to understand why this error is isotropic: the probability to take place is the same for every Pauli operator.

$$\begin{aligned} E_0 &= \sqrt{\frac{p_d}{4}}\hat{X} \qquad E_1 = \sqrt{\frac{p_d}{4}}\hat{Y} \\ E_2 &= \sqrt{\frac{p_d}{4}}\hat{Z} \qquad E_3 = \sqrt{\frac{p_d}{4}}\mathbb{I} \\ E_4 &= \sqrt{1-p_d}\mathbb{I}\end{aligned} \tag{2.62}$$

Among Pauli elements there is also the identity, therefore there is a probability $p_d/4$ that when error occurs the state still ends up in the initial state.

A more aggressive model can be defined starting directly from the definition in the Kraus notation, changing the meaning of p_d. Instead of interpreting p_d as the probability of ending in the maximally mixed state, it should be understood as the sum of equal probabilities of an $\hat{X}$, $\hat{Y}$ or $\hat{Z}$ to occur.

$$\mathcal{E}(\rho) = (1-p_d)\rho + \frac{p_d}{3}\left(\hat{X}\rho\hat{X} + \hat{Y}\rho\hat{Y} + \hat{Z}\rho\hat{Z}\right) \tag{2.63}$$

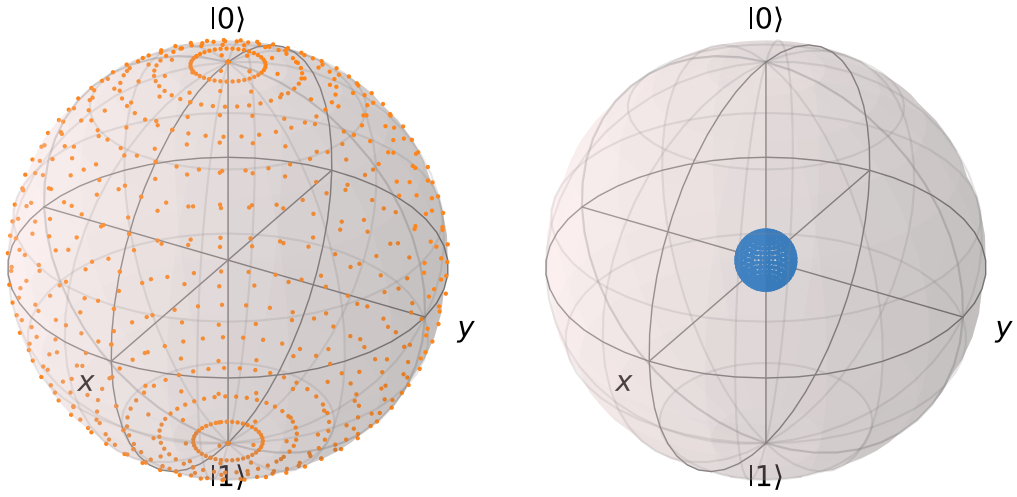


Figure 13: Evolution of a set of states on the Bloch sphere under depolarizing error with $p_d \approx 86.5\%$.

In the previous section, a description of the amplitude damping process is derived. Such model is widely used and an excellent first order approximation of real processes. The assumption of the environment being in $|0\rangle$ is fairly valid for a qubit in a very cold thermal bath but considering a finite temperature ($T > 0K$) there still exist a residual chance of excitation for the qubit by the system. This makes a big difference because in this case even starting in $|0\rangle$ does not guarantee anymore to end up there.

The simplest way to build such generalization is by defining the fraction of ground state population at thermal equilibrium (p) and applying an amplitude damping with probability p, in the remaining cases an inverse amplitude damping to represent an energy transfer from the environment to the qubit.

Such probability can be physically evaluated with the Boltzmann's distribution, by knowing the temperature (T) of the thermal bath with which qubit interacts and the difference of energy between $|1\rangle$ and $|0\rangle$ (ΔE):

$$p = \frac{1}{1 + e^{-\frac{\Delta E}{k_b T}}} \tag{2.64}$$

So the whole evolution is described by the Kraus operator of amplitude damping, weighted by the probability p and inverse amplitude damping with probability $1-p$.

$$\begin{aligned} E_0 &= \sqrt{p}\begin{pmatrix} 1 & 0 \\ 0 & \sqrt{1-\gamma} \end{pmatrix} \qquad E_1 = \sqrt{p}\begin{pmatrix} 0 & \sqrt{\gamma} \\ 0 & 0 \end{pmatrix} \\ E_2 &= \sqrt{1-p}\begin{pmatrix} \sqrt{1-\gamma} & 0 \\ 0 & 1 \end{pmatrix} \qquad E_3 = \sqrt{1-p}\begin{pmatrix} 0 & 0 \\ \sqrt{\gamma} & 0 \end{pmatrix} \end{aligned} \tag{2.65}$$

It is worth noticing that for $T \to 0, p \to 1$ obtaining the amplitude damping and for $T \to \infty, p \to \frac{1}{2}$ the evolution will end in mixed state.

Amplitude damping (T_1) and dephasing (T_ϕ) are characteristic errors of the free evolution of the qubit, depending on time in a continuous way. At this point it is worth noticing that losing amplitude coherence leads also to a loss in phase coherence, this can be seen on the off-diagonal elements of the density matrix when both noises are applied[4]

$$\dot{\rho}_{01} = -\frac{\Gamma_1}{2}\rho_{01} - \Gamma_\phi \rho_{01} \tag{2.66}$$

Where Γ are the rates at which such processes evolve, $\Gamma = \frac{1}{T}$. Derivation of this expression is out of the scope of this work but the result is useful to appreciate why a new variable to describe the phenomenon is introduced.

Loss of phase coherence ultimately depends on both T_φ and T_1 so a T_2 parameter is introduced to collect these effects:

$$\Gamma_2 = \frac{\Gamma_1}{2} + \Gamma_\phi \Rightarrow \frac{1}{T_2} = \frac{1}{2T_1} + \frac{1}{T_\phi} \tag{2.67}$$

This parameter better captures the relation between amplitude and phase coherence. Even if a device would suffer no pure dephasing $T_\phi \to \infty$, the phase coherence would still be limited by amplitude damping $T_2 \leq 2T_1$.

When coming down to quantum circuits it is rather useful to treat such errors in discrete points in the circuits, in which they are applied as if they were gates.

[4]This expression is evaluated evolving the system in the continuous domain with the Lindblad equation

As will be discussed in Section 3.3 quantum gates require a finite time amount to be physically executed on qubits, let us call this time t_g. If such duration is small enough compared to the characteristic parameters of amplitude and phase coherence times (T_1, T_2) it is possible to conceptually pack the continuous error in gates applied to the circuit.

It can be seen that applying the dephasing $\mathcal{E}_{\text{deph}}$ and then the amplitude damping $\mathcal{E}_{\text{AD}}$ is exactly the same as applying them in the swapped order.

$$\mathcal{E}_{\text{deph}}(\mathcal{E}_{\text{AD}}(\rho)) = \mathcal{E}_{\text{AD}}\big(\mathcal{E}_{\text{deph}}(\rho)\big) \tag{2.68}$$

This commutation relation allows to discretize the two operations without introducing second order errors.

The evolution of the state Eq. (2.68) is described by these Kraus operators

$$\begin{gathered} E_0 = \begin{pmatrix} \sqrt{1-p_z} & 0 \\ 0 & \sqrt{(1-p_z)(1-\gamma)} \end{pmatrix} E_1 = \begin{pmatrix} 0 & \sqrt{\gamma(1-p_z)} \\ 0 & 0 \end{pmatrix} \\ E_2 = \begin{pmatrix} \sqrt{p_z} & 0 \\ 0 & -\sqrt{p_z(1-\gamma)} \end{pmatrix} \quad E_3 = \begin{pmatrix} 0 & \sqrt{\gamma p_z} \\ 0 & 0 \end{pmatrix} \end{gathered} \tag{2.69}$$

Therefore

$$\mathcal{E}_{\text{tot}}(\rho) = \sum_{k=0}^{3} E_k \rho E_k^\dagger \tag{2.70}$$

The probability for the two sources of noise depends only on gate duration

$$p_z = \frac{1 - e^{-t_g/T_\phi}}{2} \qquad \gamma = 1 - e^{-t_g/T_1} \tag{2.71}$$

Each gate $\hat{U}$ suffers this noise so instead of the ideal evolution $\rho_1 = \hat{U}\rho_0\hat{U}^\dagger$ the state evolves as

$$\tilde{\rho}_1 = \mathcal{E}_{\text{tot}}\big(\hat{U}\rho_0\hat{U}^\dagger\big) \tag{2.72}$$

Quantum gates may suffer of several imperfections, mainly due to the hardware (non-perfect calibration, finite resolution time of the machinery, numerical approximations…). Although the evolution of the state is still unitary the actual ending point is not the desired one. This can be modeled as a perturbative term in the evolution.

$$\hat{U}_{\text{real}} = e^{-i\left(\widehat{\mathcal{H}}_{\text{id}}+\widehat{\mathcal{H}}_{\text{err}}\right)t} \rightarrow \hat{U}_{\text{real}} = \hat{U}_{\text{err}}\hat{U}_{\text{id}} \tag{2.73}$$

Suppose an $\hat{X}$ gate that should rotate the state around the x axis by a π angle, the error may lead to an unwanted under/over rotation so the gate becomes an $\hat{R}_x(\pi+\epsilon)$. Another very likely event is a rotation around the wrong axis, suppose a very strong mis-calibration leading to a rotation around the $(x+z)/\sqrt{2}$ axis, the $\hat{X}$ gate would result being a $\hat{H}$.

Considering a general 1-qubit rotation of an angle θ around the $\overline{n}$ axis as

$$\hat{U}_{\text{id}} = e^{-i\frac{\theta}{2}\overline{n}\cdot\overline{\sigma}} \tag{2.74}$$

the general coherent error acts as

$$\hat{U}_{\text{real}} = e^{-i\frac{\theta'}{2}\overline{n}'\cdot\overline{\sigma}} \tag{2.75}$$

$$\theta' = \theta + \epsilon \qquad \overline{n}' = \frac{\overline{n}+\overline{\delta}}{\sqrt{1+\left\|\overline{\delta}\right\|^2+2\overline{\delta}\cdot\overline{n}}} \tag{2.76}$$

where ϵ is the error on the angle and $\overline{\delta}$ the error on the axis around which the state rotates.

For small and almost orthogonal errors, second term in Eq. (2.76) can be simplified.

$$\begin{cases} \left\|\overline{\delta}\right\| \ll 1 \\ \\ \overline{\delta}\cdot\overline{n} \approx 0 \end{cases} \Longrightarrow \overline{n}' \approx \overline{n}+\overline{\delta} \tag{2.77}$$

The gate $\hat{U}_{\text{err}}$ can be evaluated starting from Eq. (2.73)

$$\hat{U}_{\text{err}} = \hat{U}_{\text{real}}\hat{U}_{\text{id}}^{\dagger} \tag{2.78}$$

A remarkable difference between these and incoherent errors lies in their propagation: coherent deviations preserve the purity of the state, allowing for errors to interfere. Infidelity for incoherent error (with probability p) propagates with the number of gates (N) as a random walk $\mathcal{O}(pN)$, whereas for the worst case scenario the statevector rotates by an angle differing of $N\epsilon$ acting on the amplitude rather than classical probability causing the infidelity to increase as $\mathcal{O}(\epsilon^2N^2)$.

Another family of errors are more hardware related, in the following a brief description will be given mantaining a good degree of generality.

Quantum algorithms must interface the classical world at least at their beginning (when preparing the starting state) and at their end (when performing the readout). A class of errors is identified in this context: State Preparation And Measurement *(SPAM)*.

With no loss of generality all quantum algorithms can be considered starting in $|0\rangle$ state, but not always hardware can fulfil this need. Generally speaking, this error acts on $|0\rangle$ in a non unitary way:

$$\rho = \mathcal{E}_{\mathrm{SP}}(|0\rangle\langle 0|) \tag{2.79}$$

In many technologies to implement qubits there are two main techniques to initialize the system in the ground state: *passive wait* or *active reset*. For the first one the amplitude damping process is exploited to thermalize a qubit to its ground state. Nevertheless, a residual probability of it being excited is still present, this is modeled as a bit flip with probability p

$$\mathcal{E}_{\mathrm{PW}}(|0\rangle\langle 0|) = (1-p)|0\rangle\langle 0| + p|1\rangle\langle 1| \tag{2.80}$$

Alternatively, active reset, performs measurements and operations in a feedback loop allowing for shorter reset times. In a simple model this can be seen as a measure and direct operation of a $\hat{X}$ gate depending on the result of the measurement. This operation starts on a general unknown state (even mixed)

$$\mathcal{E}_{\mathrm{AR}}(\rho) = E_0 \rho E_0^\dagger + E_1 \rho E_1^\dagger \tag{2.81}$$

where the application of $E_0 = \mathbb{I}$ or $E_1 = \hat{X}$ depends on the result of the measurement. This method ensures shorter initialization times but would require a perfect measurement and a perfect $\hat{X}$ gate, but none of these two operations are perfect resulting in an unprecise state preparation.

Measurement errors, in their most basic approach, can be modeled as a Markov process in which there exists a probability of measuring `0` when the state was $|1\rangle$ and vice versa.

This can be represented in a matrix in which columns denote the actual state and rows are the measured ones. In each cell the conditional probability of such measure is evaluated.

	State $\|0\rangle$	State $\|1\rangle$
Meas `0`	$\mathbb{P}(0\|0)$	$\mathbb{P}(0\|1)$
Meas `1`	$\mathbb{P}(1\|0)$	$\mathbb{P}(1\|1)$

Table 4: Confusion matrix of quantum state against measured state.

Ideally this confusion matrix Λ should match with the identity, but errors add off-diagonal terms.

$$\Lambda = \begin{pmatrix} 1-\epsilon_{1|0} & \epsilon_{0|1} \\ \epsilon_{1|0} & 1-\epsilon_{0|1} \end{pmatrix} \tag{2.82}$$

A first approximation consists in assuming all qubits as independent, therefore each one will have its own confusion matrix Λ_i and the composite one for the whole system is constructed as the tensor product of the local ones:

$$\Lambda = \bigotimes \Lambda_i \tag{2.83}$$

This technique looses cross correlations between qubits, which are very dominant when simultaneously measuring more of them.

This matrix, once characterized, can be used to enhance the readout performance by creating the Readout Error Mitigation (REM) matrix which is applied as post processing step to the raw measured statistic. Once algorithms are executed the distribution for the states is collected in p_{noisy} then, to retrieve the mitigated one the inverse of Λ is applied.

$$p_{\text{mitigated}} = \Lambda^{-}1 p_{\text{noisy}} \tag{2.84}$$

Hardware limitations also lead to *two-qubit interactions* strongly depending on the employed technology. One of the most common issues is a *ZZ* coupling: dynamics in which a qubit's state influences the state of a coupled qubit by adding extra $R_z(\theta)$ rotations. For two qubits i and j their *ZZ* crosstalk evolves following $\hat{Z}_i\hat{Z}_j$ dynamics with a strength ζ:

$$\hat{U} = e^{-i\frac{\zeta t}{2}\hat{Z}_i\hat{Z}_j} = R_{\text{zz}}(\theta) \tag{2.85}$$

Here the unwanted rotation increases linearly with time when the two qubits are interacting, $\theta = \zeta t$. This coupling may be always on if qubits are directly coupled or may be greatly reduced with ad hoc couplers. From the point of view of a single qubit, this can be seen as a $R_z(\theta)$ rotation when its coupled counterpart is in $|0\rangle$ and $R_z(-\theta)$ when in $|1\rangle$.

Ultimately qubits are embedded in quantum systems with typically more than 2 states, therefore if quantum gates are not properly calibrated they may excite a transition $|1\rangle \rightarrow |2\rangle$ causing *leakage* to larger Hilbert spaces. Depending on the physical source generating this error, different models can be derived. For the case of interest in this work, it is convenient to think of it as a unitary error, not caused by spurious thermal excitations and therefore reversible.

Its unitary evolution is described by:

$$\hat{U} = |0\rangle\langle 0| + \cos(\theta)(|1\rangle\langle 1| + |2\rangle\langle 2|) - i\sin(\theta)(|2\rangle\langle 1| + |1\rangle\langle 2|) \quad (2.86)$$

The $|0\rangle$ state remains untouched but the $|1\rangle$ may jump to $|2\rangle$ depending on the effective mixing angle θ.

Chapter 3
System Architecture

3.1. The *Lagrange* Quantum Computer

Lagrange is a IQM Spark quantum computer, jointly acquired by *Politecnico di Torino*, *Fondazione LINKS* and Italian National Institute of Metrological Research *(INRiM)*. It has been installed in Politecnico di Torino in Quantum Computing and Simulation (QCS) Lab in mid-2025 and actively maintained by Fondazione LINKS. [9]

IQM Spark machines are based on superconducting technology, specifically they consist of 5 transmon qubits, interconnected in a star topology by means of tunable couplers allowing for on-demand coupling among qubits.

3.2. Transmon Qubits

During the years many ideas for 2 Level Systems (2LS) have been proposed, spin of atoms, polarization of photons, energy state of electrons and many more. Among these, superconducting materials allow to easily fabricate and test devices in which quantum effects were exhibited. This technology makes it possible to work with circuits similar to classical ones, exploiting quasi-lumped or even lumped elements diagrams. Schrödinger picture of quantum mechanics, with its unitary operators, does not allow energy losses out of the system in any form, including heat. This is of course a limitation and, at least to describe some part of the universe (such as the chip in a laboratory), may not be the most accurate description. In this formalism, no resistors can exist in the circuits, which will be composed of inductors and capacitors. If a more general description is desired the open-system formalism is required, but it is often enough to suppose the system closed.

2LS are good approximations of systems in which only two states are observed and controlled, therefore an intrinsic requirement for working with this hypothesis is the ability to stay in this 2-fold of states.

3.2.1. Josephson Junction

The Josephson Junction (JJ) played a crucial role in exploiting superconducting technology to devise qubits. Following the Ginzburg-Landau theory or macroscopic quantum model, a macroscopic wavefunction can be built to describe coherent motion of couples of electrons with opposite spins known as *Cooper pairs*. These pairs act as bosons and their macroscopic wavefunction is:

$$\Psi(x) = \sqrt{n_s(x)}e^{i\phi(x)} \tag{3.1}$$

Where $n_s = |\Psi|^2$ is the Cooper pairs density and ϕ is the macroscopic phase. These two quantities represent the spatial distribution of charge and their momentum (therefore current).

JJs consist of a thin layer of insulator (I) between two superconducting (S) chunks, akin to a capacitor, resulting in a Superconductor-Insulator-Superconductor (SIS) junction. Thickness of insulator d layer must be smaller with respect to the penetration length of the Cooper pair wavefunction λ_D to allow Cooper pairs to tunnel between the extremities.

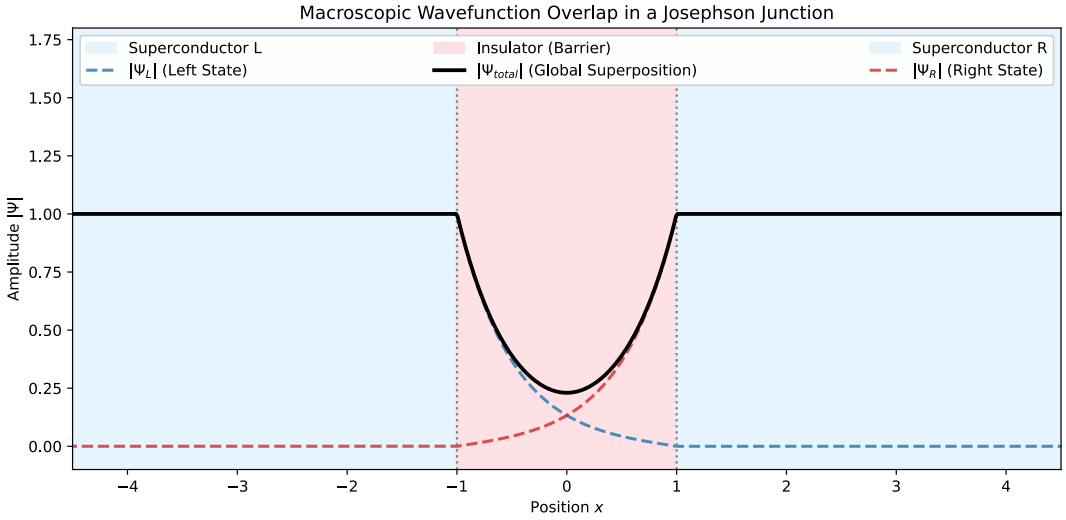


Figure 14: Plot of the macroscopic quantum wavefunction in a SIS junction.

Difference in the macroscopic phases $\Delta\phi = \phi_L - \phi_R$ plays a crucial role in the Josephson phase relation: this is described in the Josephson phase and current equations.

$$\frac{d\phi}{dt} = \frac{2\pi}{\Phi_0} V \qquad I = I_c \sin(\phi) \tag{3.2}$$

where I_c is the critical current, a device fabrication specific parameter determining the maximum current below which the junction mantains the zero resistance state. It is possible to combine Eq. (3.2), to separate voltage across the junction and current traversing it:

$$V = \frac{\Phi_0}{2\pi I_c \cos(\phi)} \frac{dI}{dt} \tag{3.3}$$

This is the constitutive relation of an inductor, but instead of being constant like classical coils it has a variable inductance:

$$L(\phi) = \frac{\Phi_0}{2\pi I_c \cos(\phi)} \tag{3.4}$$

When the phases are forced to misalign ($\Delta\phi$ increased), a potential energy is accumulated. Such potential energy can be evaluated as

$$\begin{aligned} U_L &= \int P(t)\ \mathrm{dt} = \int V(t) I(t)\ \mathrm{dt} \\ &= \frac{\Phi_0}{2\pi} \int \frac{d\phi}{\mathrm{dt}} I_c \sin(\phi)\ \mathrm{dt} \\ &= \frac{I_c \Phi_0}{2\pi} \int \sin(\phi) d\phi = -\frac{I_c \Phi_0}{2\pi} \cos(\phi) \end{aligned} \tag{3.5}$$

Which can be conveniently recast in

$$U_L = -E_J \cos(\phi) \tag{3.6}$$

by conveniently introducing the Josephson energy term E_J which includes device specific value I_c. This is the core of a JJ, but is not the full story: although Cooper pairs tunneling is the very heart of this dynamics, it is implemented in real devices which are fabricated and may have other effects.

Being fabricated as an insulator between two (super)conducting materials, real junctions have also somewhat a capacitance between the plates. This is another device-specific parameter and can be slightly tuned during fabrication.

$$I = C_J \frac{\mathrm{dV}}{\mathrm{dt}} = \frac{\Phi_0}{2\pi} \frac{d^2\phi}{dt^2} \tag{3.7}$$

Planning to trap charges to build qubits, a fundamental quantity is the charging energy E_c: the amount of energy required to move a single electron from one plate to the other:

$$E_c = \frac{e^2}{2C_J} \tag{3.8}$$

Starting from the neutral condition in the capacitor, after n charges (Cooper pairs) have been transferred, the potential energy due to capacitive effects becomes

$$U_C = nE_c = \frac{(2ne)^2}{2C_J} = 4E_c n^2 \tag{3.9}$$

When exiting the superconducting regime, a shunt resistance must be considered but in this approximation JJs are devices which behaves both as a capacitors and as non-linear inductors:

$$U_J = E_c 4n^2 - E_J \cos(\varphi) \tag{3.10}$$

The lumped element symbol of a JJ in superconducting regime is reported in Figure 15.

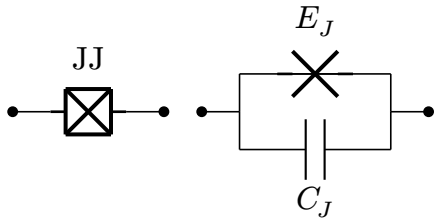


Figure 15: Lumped element representation of Josephson junction.

3.2.2. Charge qubit

Charge qubits implement 2LS by encoding information in the presence of an *extra* charge in a confined superconducting island.

The island can be thought as the superconducting region between a JJ and its voltage source capacitively coupled. The basic working principle is based on quantum tunneling: Cooper pairs tunnel into the island through the JJ. The applied gate voltage V_g tunes the electrostatic energy landscape, controlling the preferred number of excess Cooper pairs on the island.

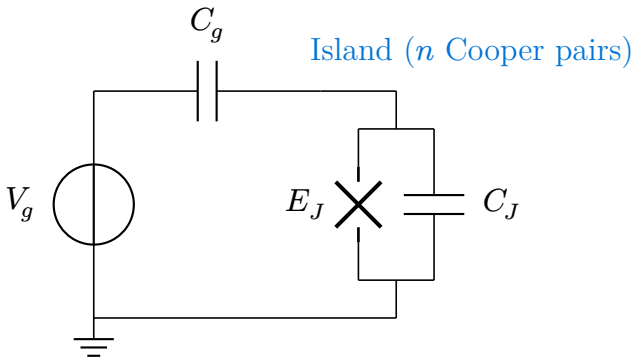


Figure 16: Circuit representation of a charge qubit

The gate capacitance C_g contributes to the total capacitance of the island, which defines the single-electron charging energy:

$$E_c = \frac{e^2}{2(C_J + C_g)} \tag{3.11}$$

The hamiltonian of the circuit becomes

$$\mathcal{H} = 4E_c(n - n_g)^2 - E_J \cos(\phi) \tag{3.12}$$

It is possible to use DC component of V_g to tune the n_g parameter (tipically in its sweet spot $n_g = 0.5$) and by bringing the AC frequency to resonate with the energy levels of this qubit, gates can be applied. For this system, number of charges n and phase ϕ are conjugate variables:

$$[n, \phi] = i \tag{3.13}$$

It follows that these two quantities must obey the uncertainty relation

$$\Delta n \Delta \phi \geq \frac{1}{2} \tag{3.14}$$

The energetic landscape of the charge qubit is plotted in Figure 17, for the case in which $E_J/E_c = 1$. In the left subplot the first 4 eigenvalues of the hamiltonian are plotted, at different valus of induced gate charge n_g. It can be appreciated why the $n_g = 0.5$ sweetspot is important: it is the point for which fluctuations on gate charge cause the smallest energy differences. In the right plot the potential term created by the JJ is depicted, as well as eigenstates in the ϕ space. None of the states is confined in this space.

In can be thought as a pendulum which occupy angles with different probabilities. As a limit case when the number of charges is perfecly defined ($E_J = 0$), the probability of being in each angle is equal (constant $|\Psi|^2$).

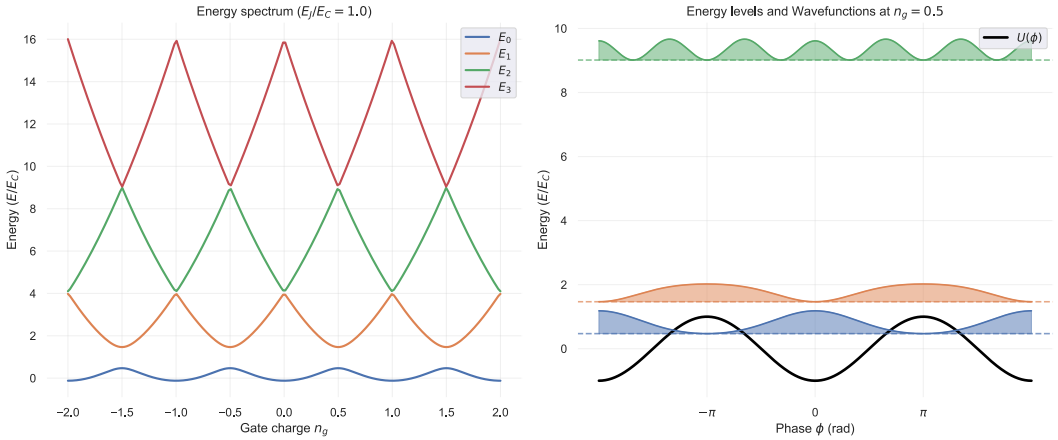


Figure 17: Plot of energetic landscape for a charge qubit $E_J/E_c = 1$.

Unfortunately many imperfections (e.g. material defects, fabrication processes...) lead to instability in n_g, known as *charge noise* affecting the effective energy separation between the first two states E_{01}.

3.2.3. Transmon qubit

To understand which path could be taken to improve the charge qubit, two fundamental quantities are introduced.

Relative anharmonicity: To quantify how different the two transitions $|0\rangle \rightarrow |1\rangle$ and $|1\rangle \rightarrow |2\rangle$ are, it is usually normalized against the first transition).

$$\alpha = E_{21} - E_{10} \qquad \alpha_r = \frac{E_{21} - E_{10}}{E_{10}} \tag{3.15}$$

Charge dispersion: When varying n_g the energy difference for each state between maximum and minimum is:

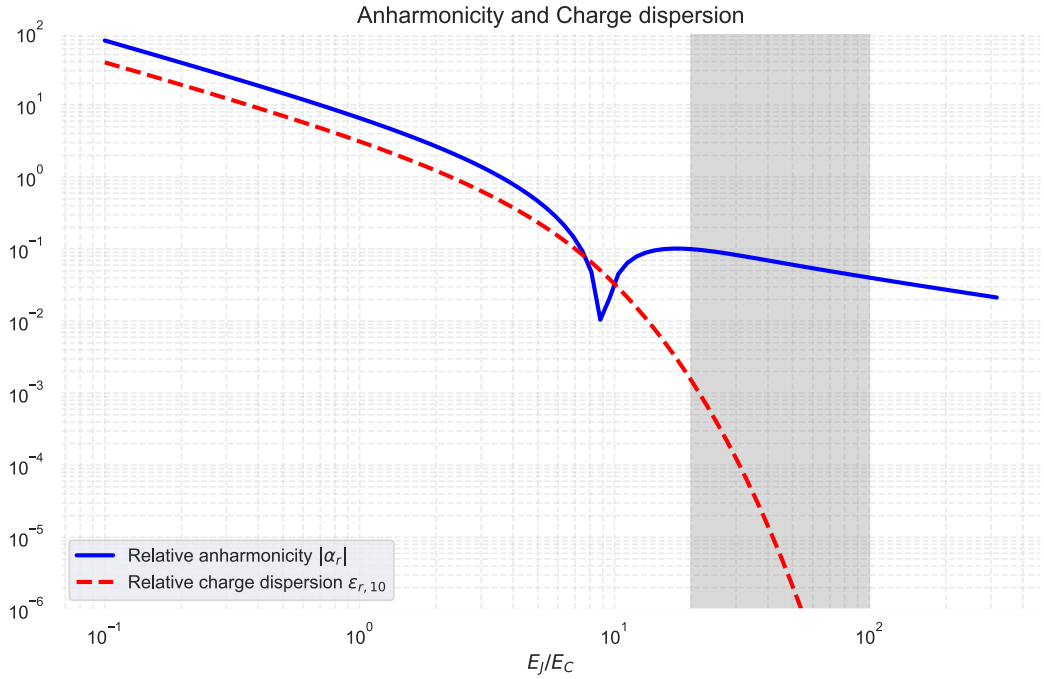
$$\epsilon_n = E_n\big(n_g = 0.5\big) - E_n\big(n_g = 0\big) \tag{3.16}$$

Looking for the $|0\rangle \rightarrow |1\rangle$ transition, ϵ_1 is of particular interest as it represents the stability of a state against charge noise. What becomes particularly

interesting is to evaluate this stability in the transition instead of in the single levels, this value is usually normalized with the actual transition energy.

$$\epsilon_{10} = \epsilon_1 - \epsilon_0 \qquad \epsilon_{\mathrm{r},10} = \frac{\epsilon_1 - \epsilon_0}{E_{10}} \tag{3.17}$$

Let us evaluate these two parameters by varying the E_J/E_c ratio:



For $E_J/E_c \approx 8.5$ the anharmonicity drops to 0, behaving as an harmonic oscillator. In Figure 18 a region is identified, for E_J/E_c between 20 and 100. For such values charge dispersion is exponentially suppressed whereas anharmonicity decreases algebraically.

To reduce the charging energy, island capacitance should be decreased. This can be achieved by introducing a large shunt capacitor to the JJ, a typical value is $E_J/E_c = 50$ for which anharmonicity is $\approx -6\%$, which for typical resonance frequencies (few GHz) is in the order of hundreds of MHz.

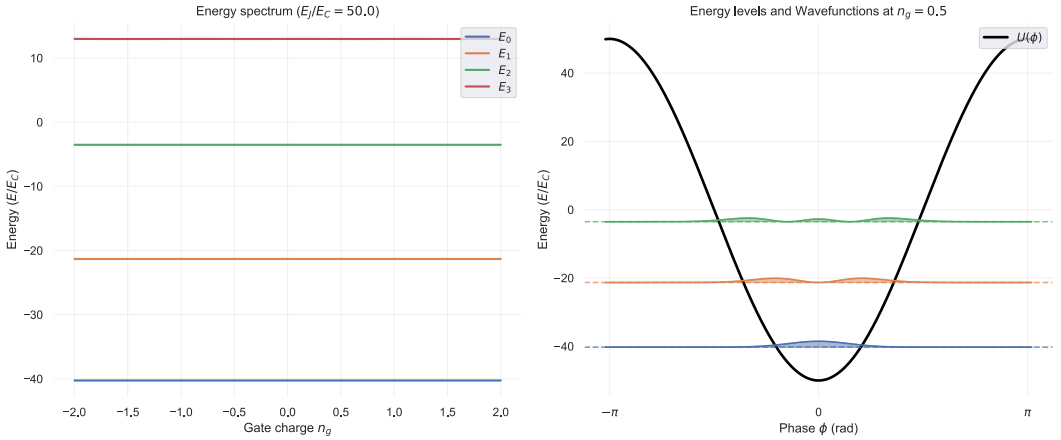


Figure 19: Plot of energetic landscape for a charge qubit $E_J/E_c = 50$.

A fundamental improvement is achieved by placing a second JJ in parallel to the first one. By doing so, a special configuration called Superconducting QUantum Interference Device (SQUID) is created, where the Josephson energy term can be tuned by applying a magnetic field inside the loop created between the two junctions.

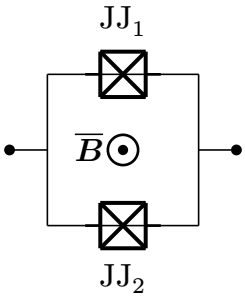


Figure 20: Schematic of a SQUID with an applied magnetic field $\overline{\boldsymbol{B}}$.

Each JJ is uniquely characterized by its critical current I_c defined during the fabrication process, possibly different for each of them. An asymmetry parameter is defined as:

$$d = \frac{E_{\mathrm{J1}} - E_{\mathrm{J2}}}{E_{\mathrm{J1}} + E_{\mathrm{J2}}} = \frac{I_{\mathrm{c1}} - I_{\mathrm{c2}}}{I_{\mathrm{c1}} + I_{\mathrm{c2}}} \tag{3.18}$$

with the convenient introduction of the total Josephson energy

$$E_{J\Sigma} = E_{\mathrm{J}1} + E_{\mathrm{J}2} \Longrightarrow E_{\mathrm{J}1} - E_{\mathrm{J}2} = E_{J\Sigma} d \tag{3.19}$$

and a change of variables

$$\begin{cases} \delta = \phi_1 - \phi_2 \\ \phi = \frac{\phi_2 + \phi_1}{2} \end{cases} \Longrightarrow \begin{cases} \phi_1 = \phi + \frac{\delta}{2} \\ \phi_2 = \phi - \frac{\delta}{2} \end{cases} \tag{3.20}$$

allows to rewrite the energy

$$U = -E_{\mathrm{J}1} \cos(\phi_1) - E_{\mathrm{J}2} \cos(\phi_2) \tag{3.21}$$

as

$$\begin{aligned} U &= -E_{\mathrm{J}1} \cos\left(\phi + \frac{\delta}{2}\right) - E_{\mathrm{J}2} \cos\left(\phi - \frac{\delta}{2}\right) \\ &= -(E_{\mathrm{J}1} + E_{\mathrm{J}2}) \cos\left(\frac{\delta}{2}\right) \cos(\phi) + (E_{\mathrm{J}1} - E_{\mathrm{J}2}) \sin\left(\frac{\delta}{2}\right) \sin(\phi) \end{aligned} \tag{3.22}$$

Which can be recast to explicitly isolate the ϕ variable in a cosine, by recognizing it as a linear sum of $\sin(\phi)$ and $\cos(\phi)$.

$$U = A \cos(\phi) + B \sin(\phi) = -R \cos(\phi - \phi_0) \tag{3.23}$$

Where

$$\begin{cases} A = E_{J\Sigma} \cos\left(\frac{\delta}{2}\right) \\ B = E_{J\Sigma} d \sin\left(\frac{\delta}{2}\right) \end{cases}$$

$$\begin{aligned} R &= \sqrt{A^2 + B^2} = E_{J\Sigma} \sqrt{\cos^2\left(\frac{\delta}{2}\right) + d^2 \sin^2\left(\frac{\delta}{2}\right)} \\ \phi_0 &= \tan^{-1}\left(\frac{B}{A}\right) = \tan^{-1}\left(d \tan\left(\frac{\delta}{2}\right)\right) \end{aligned} \tag{3.24}$$

It should be noted that ϕ_0 is just an offset for the coordinate ϕ, and it can be omitted.[5]. Therefore, after renaming $R = E_J^{\mathrm{eff}}$:

$$U = -E_J^{\mathrm{eff}} \cos(\phi - \phi_0) \tag{3.25}$$

which has the exact same form of the energy of a *single* JJ. The real advantage emerges when noticing that E_J^{eff} is a function of δ and the asymmetry parameter d. While the latter is fixed during the fabrication, the former depends on the

[5]Formally, this should be a traslation of the system represented by the change of variable $\tilde{\phi} = \phi - \phi_0$, but $\tilde{\phi}$ and ϕ are confused for ease of handling.

applied flux. To understand how to control this parameter let us get back to its definition:

$$\delta = \phi_1 - \phi_2 \tag{3.26}$$

In a continuous superconducting loop, the total concatenated magnetic flux Φ is quantized: $\Phi_{\text{ext}} = n\Phi_0$. Where Φ_0 is the quantum of flux.

$$\Phi_0 = \frac{h}{2e} \qquad \frac{\Phi_{\text{ext}}}{\Phi_0} = n \tag{3.27}$$

When breaking the continuous superconducting loop, this relation changes to take into account how the phase varies in the discontinuities: for the JJ case this happens because of the insulator part of SIS junctions. This quantization relation becomes

$$2\pi\frac{\Phi_{\text{ext}}}{\Phi_0} + \phi_2 - \phi_1 = 2\pi n \tag{3.28}$$

which, disregarding the periodicity, is exactly

$$\delta = \phi_1 - \phi_2 = 2\pi\frac{\Phi_{\text{ext}}}{\Phi_0} \tag{3.29}$$

Inserting this physical relation into the mathematical derivation for the potential energy of the SQUID, it becomes clear how the external magnetic field can be exploited to tune the hamiltonian.

$$\begin{gathered} U = -E_J^{\text{eff}}(\Phi_{\text{ext}})\cos(\phi) \\ E_J^{\text{eff}}(\Phi_{\text{ext}}) = E_{J\Sigma}\sqrt{\cos^2\left(\pi\frac{\Phi_{\text{ext}}}{\Phi_0}\right) + d^2\sin^2\left(\pi\frac{\Phi_{\text{ext}}}{\Phi_0}\right)} \end{gathered} \tag{3.30}$$

Therefore, it is convenient to introduce a SQUID instead of a single JJ because it allows to tune the hamiltonian by applying an external magnetic field. Practically speaking, a magnetic field $\overline{\boldsymbol{B}}$ is produced by a DC current flowing in a coplanar line parallel to the SQUID plane. Specifically, the range in which effective Josephson energy can vary depends on the asymmetry parameter: $E_J^{\text{eff}} \in [d, E_{J\Sigma}]$. For two perfectly symmetrical JJs this results in a range from 0 up to $2E_J$. On the other hand a slight asymmetry reduces the range in which E_J^{eff} lives, reducing the sensitivity to fluctuations in the applied control magnetic field.

To illustrate how the external magnetic field changes the way a transmon can be controlled, an example (values in Table 5) is reported. For this example the gate charge is set in the sweetspot $n_g = 0.5$, with an asymmetry $d \approx 0.5$ and the ratio between Josephson energy and charge energy is $E_J/E_c \approx 50$.

	$\mathbf{JJ_1}$		$\mathbf{JJ_2}$		
C_g	C_{J1}	I_{c1}	C_{J2}	I_{c2}	C_s
1 fF	1.5 fF	18.8 nA	0.5 fF	6.3 nA	74.4 fF

Table 5: Parameters for the analyzed transmon qubit.

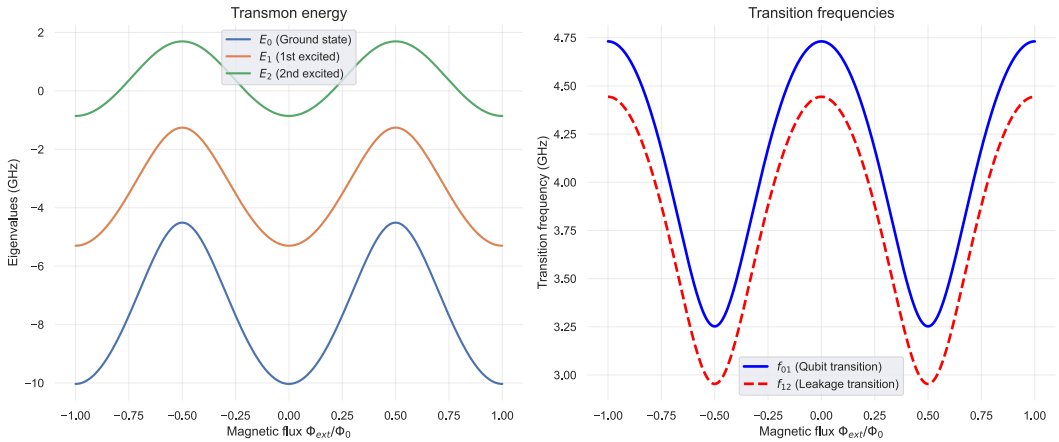


Figure 21: Left: Energy levels of the transmon as function of the external magnetic flux Φ_{ext}. Right: First two transition energies as function of Φ_{ext}.

This plots offer a rough idea for the amount of tuning that can be performed, and the energetic difference between levels. Operatively to maximize coherence times transmons spend most of the time at $\Phi_{\text{ext}} = 0$ preserving their anharmonicity, then to couple them (e.g. to have ZZ interactions) they are brought at the same frequency by varying the applied flux. As a valid approximation, eigenvalues of the transmons' hamiltonian can be evaluated by approximating the cosine potential with its Taylor expansion:

$$\cos(\phi) = 1 - \frac{\phi^2}{2} + \frac{\phi^4}{24}... \tag{3.31}$$

Therefore, the hamiltonian of the transmon

$$\widehat{\mathcal{H}} = 4E_c\big(\hat{n} - n_g\big)^2 - E_J^{\text{eff}}(\Phi_{\text{ext}})\cos\big(\hat{\phi}\big) \tag{3.32}$$

can be approximated as

$$\widehat{\mathcal{H}} \approx 4E_c\hat{n}^2 + E_J^{\text{eff}}(\Phi_{\text{ext}})\left(-\frac{\hat{\phi}^2}{2} + \frac{\hat{\phi}^4}{24}\right) \tag{3.33}$$

The first two terms are exactly an harmonic oscillator

$$\widehat{\mathcal{H}}_o = 4E_c\hat{n}^2 - \frac{\hat{\phi}^2}{2}E_J^{\text{eff}}(\Phi_{\text{ext}}) \tag{3.34}$$

with eigenvalues

$$f = \frac{\sqrt{8E_J^{\text{eff}}E_c}}{h} \tag{3.35}$$

The quartic perturbative term can be added to this harmonic oscillator

$$\widehat{\mathcal{H}} = \widehat{\mathcal{H}}_o + \widehat{\mathcal{H}}_p \tag{3.36}$$

Introducing a state dependent shift in the eigenvalues:

$$E_k \approx k\sqrt{8E_J^{\text{eff}}E_c} - \frac{E_c}{2}(k^2 + k) \tag{3.37}$$

Therefore the energy gap between states k and $k+1$ is

$$\Delta E \approx \sqrt{8E_J^{\text{eff}}E_c} - E_c(k+1) \tag{3.38}$$

This approximation holds for the first few eigenstates, so evalutating the whole spectrum would not give accurate results. Nevertheless willing to work in a 2LS, this result can be considered a solid ground on top of which transmon qubits can be described.

Transmon qubits can be schematized in a lumped element circuit as follows:

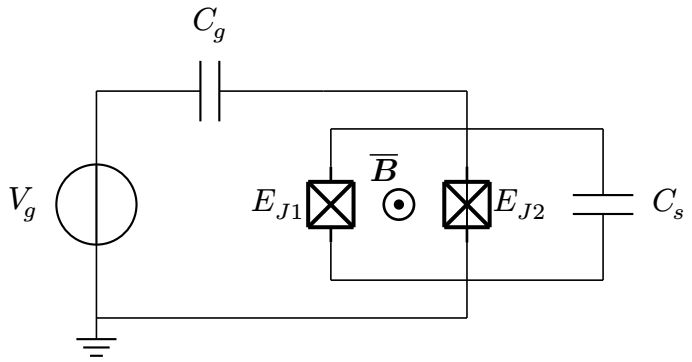


Figure 22: Schematic of a transmon qubit with an applied magnetic field $\overline{\boldsymbol{B}}$.

3.3. Qubits control

Transmon qubits have two dynamical degrees of freedom, namely *flux* and *drive*. For each of the 5 transmon qubits in *Lagrange* dedicated lines carry control signals for these two parameters. Both flux and drive are implemented as coplanar waveguides arriving directly near to the qubit, but in profoundly different ways. They are typically implemented in the superconducting layer by etching the two sidewalls (or trenches) down to the insulating substrate. Flux lines must pass close to the SQUID, so that the DC supercurrent generates a magnetic field perpendicular to the plane: this is the $\overline{\boldsymbol{B}}$ component reported in Figure 22. This line is short-ended on the ground plane of the chip to maximize the current flow. It can also be used to deliver pulses at qubits resonance frequencies between the first two states ω_{10} to perform two-qubit gates. Drive lines are the main access point for controlling the qubits: RF voltage signals at ω_{10} propagate along the lines towards their open-ended terminations, located close to the qubit islands. Through capacitive coupling, the resulting electric field drives the island charges, enabling the implementation of quantum gates. This coupling is represented schematically by the voltage source V_g in Figure 22. As an example, Figure 23 shows two coupled qubits (blue on the left, orange on the right). In particular, also drive line in purple and flux line in dark green are shown.

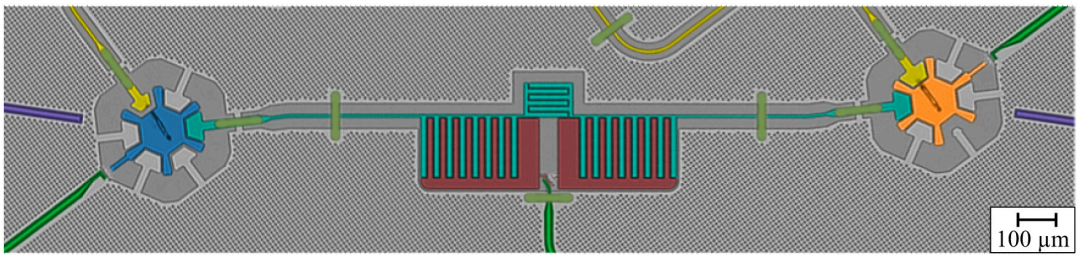


Figure 23: A false-colored micrograph of a qubit-coupler-qubit system. Image from [10]

Qubits in *Lagrange* are disposed in a star topology, as shown in Figure 24 so the central qubit *QB3* must be able to interact with all other qubits. In a static regime, this interaction would be deleterious for quantum information stored in the system, therefore *tunable couplers* (TC) are introduced between interconnected pairs. Such couplers are particular implementations of transmons, employed to selectively couple and decouple pairs of qubits by altering their resonance frequency with a flux line (as can be seen in Figure 23). The tunable coupler operates by exploiting interference between different coupling contributions to suppress the effective interaction between the qubits. By appropriately tuning its resonance frequency through the flux line, the coupler can bring the effective coupling close to zero, effectively decoupling the qubits. When an interaction is required, the flux bias is adjusted to restore a finite effective coupling, enabling controlled interactions between the qubits. In the same picture flux lines in red and drive lines in blue can be seen.

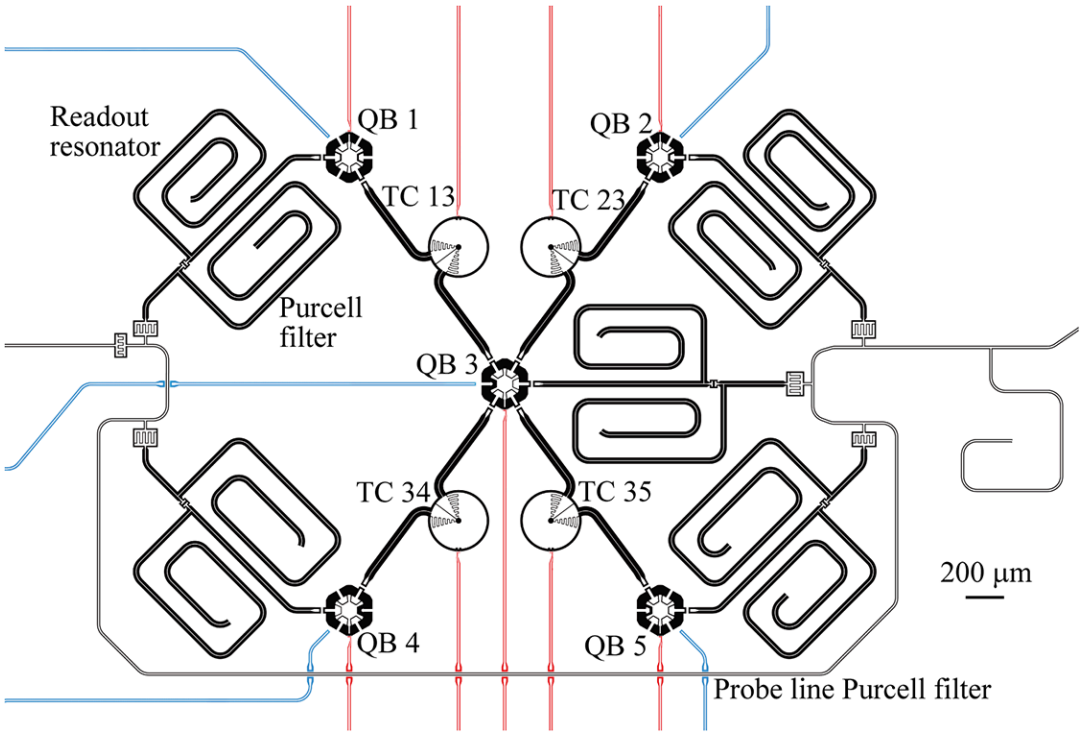


Figure 24: Design of the QPU for an IQM Spark machine.
Image from [1]

Let us understand how the drive line interacts with the qubit with a semi-classical model: signal in the line is treated as a classical voltage which interacts with the transmon. A useful approximation is to consider just the first two states of the transmon, leading to the following hamiltonian:

$$\widehat{\mathcal{H}} = -\frac{\hbar\omega_q}{2}\hat{\sigma}_z + \hbar\Omega V_d(t)\hat{\sigma}_y \tag{3.39}$$

Some useful system-parameter are introduced: $V_d(t)$ is the drive voltage signal sent through the drive line and Ω which can be thought as a coupling factor between the drive line and the transmon.

$$\Omega = \frac{C_d}{C_\Sigma}\sqrt{\frac{1}{2\hbar Z}} \qquad Z = \sqrt{\frac{L}{C}} \tag{3.40}$$

The 2LS hypothesis can be later relaxed by considering the craved anharmonicity and therefore other excited states, allowing to evaluate leackage phenomena.

Jumping back to Eq. (3.39), this hamiltonian is written by looking at the qubit from an external reference frame. It is way more convenient to anchor our point of view to a rotating reference frame with the qubit. Such new hamiltonian, denoted with $\sim$ to remember it refers to the rotating frame, is recast as:

$$\widetilde{\mathcal{H}} = \hbar\Omega V_d(t)\big(\cos\big(\omega_q t\big)\hat{\sigma}_y - \sin\big(\omega_q t\big)\hat{\sigma}_x\big) \tag{3.41}$$

The $V_d(t)$ signal is conveniently decomposed by a time independent amplitude V_0 and its dimensionless envelope $v(t)$. Working with Amplitude Modulation concepts, the envelope can be thought as a carrier tone (at a frequency ω_d) with both an in-phase (I) and quadrature-phase (Q) components

$$\begin{aligned} v(t) &= s(t)\cos(\omega_d t + \phi) \\ &= s(t)(\cos(\phi)\cos(\omega_d t) - \sin(\phi)\sin(\omega_d t)) \\ &= s(t)(I\cos(\omega_d t) - Q\sin(\omega_d t)) \end{aligned} \tag{3.42}$$

where $I = \cos(\phi)$ and $Q = \sin(\phi)$. Then by inserting Eq. (3.42) in Eq. (3.41):

$$\widetilde{\mathcal{H}} = \hbar\Omega V_0 s(t)(I\cos(\omega_d t) - Q\sin(\omega_d t))\big(\cos\big(\omega_q t\big)\hat{\sigma}_y - \sin\big(\omega_q t\big)\hat{\sigma}_x\big) \tag{3.43}$$

By expanding the products, applying the trigonometric sum and difference identities, and neglecting the rapidly oscillating terms at frequencies $\omega_q + \omega_d$ within the rotating-wave approximation (RWA), the hamiltonian can be expressed in terms of the detuning $\delta\omega = \omega_q - \omega_d$:

$$\begin{aligned} \widetilde{\mathcal{H}} = \frac{1}{2}\hbar\Omega V_0 s(t)\Big(&\hat{\sigma}_y(I\cos(\delta\omega t) + Q\sin(\delta\omega t)) \\ &-\hat{\sigma}_x(I\sin(\delta\omega t) - Q\cos(\delta\omega t))\Big) \end{aligned} \tag{3.44}$$

Which, in matrix form is

$$\widetilde{\mathcal{H}} = \frac{1}{2i}\hbar\Omega V_0 s(t)\begin{pmatrix} 0 & e^{-i(\delta\omega t-\phi)} \\ -e^{i(\delta\omega t-\phi)} & 0 \end{pmatrix} \tag{3.45}$$

It is rather useful to discuss what happens if the drive pulse has the same frequency of the qubit:

$$\delta\omega = 0 \Longrightarrow \widetilde{\mathcal{H}} = \frac{1}{2}\hbar\Omega V_0 s(t)\big(Q\hat{\sigma}_x + I\hat{\sigma}_y\big) \tag{3.46}$$

Showing how the Q component of the drive signal rotates the qubit around x axis and the I around the y axis.

The amount of rotation can be quantified, for example considering a purely Q pulse. To do so, the evolution operator after a time t can be written as:

$$\begin{aligned}\hat{U}(t) &= \exp\left(-\frac{i}{\hbar}\int_0^t \widehat{\mathcal{H}}(t')\mathrm{d}t'\right) \\ &= \exp\left(-i\frac{\Omega V_0}{2}\int_0^t s(t')\mathrm{d}t'\hat{\sigma}_x\right) \\ &= \exp\left(-\frac{i}{2}\Theta(t)\hat{\sigma}_x\right)\end{aligned} \tag{3.47}$$

Which is exacty the unitary evolution associated to a $\hat{R}_x(\Theta)$ gate, where the amount of rotation is

$$\Theta(t) = \Omega V_0 \int_0^t s(t')\mathrm{d}t' \tag{3.48}$$

Analogous reasoning can be done to perform rotations around y axis. Being Θ the amount of rotation around the given axis, a common definition is given for those pulses in which:

$$\Omega V_0 \int_{t_0}^{t_1} s(t')\mathrm{d}t' = \pi \tag{3.49}$$

such pulses are said π-pulse and, analogously, $\pi/2$ pulses are defined.

Regarding the z axis rotations, a very elegant solution allows to implement them flawlessly. [11] The core idea is to shift the phase of drive signal (rotation on the IQ) plane, so that rotations subsequently applied around x or y axis will carry this shift in their rotation, performing de facto the previous $\hat{R}_z(\alpha)$. This is easily achieved in modern systems, in which drive signal is digitally generated by adding the desired rotation α to the global phase register/variable

[6] Limited by numerical precision of the DSP.

in the DSP. In this way an instantaneous and almost perfect[6] z rotation is implemented. Consider the hamiltonian of a general resonant pulse:

$$\widetilde{\mathcal{H}}_d = \frac{\hbar\Omega V_0}{2} s(t)\big(\sin(\phi)\hat{\sigma}_x + \cos(\phi)\hat{\sigma}_y\big) \tag{3.50}$$

If an extra phase term was also present:

$$\widetilde{\mathcal{H}}'_d = \frac{\hbar\Omega V_0}{2} s(t)\big(\sin(\phi+\alpha)\hat{\sigma}_x + \cos(\phi+\alpha)\hat{\sigma}_y\big) \tag{3.51}$$

It would be equivalent to the original hamiltonian in a new reference frame, in which a $\hat{R}_z(\alpha)$ rotation has been applied before.

$$\begin{aligned} R_z(-\alpha)\widetilde{\mathcal{H}}_d R_z(\alpha) = \frac{\hbar\Omega V_0}{2} s(t)\Big(& \\ & \cos(\phi)\big(\hat{\sigma}_x \sin(\alpha) + \hat{\sigma}_y \cos(\alpha)\big) + \\ & \sin(\phi)\big(\hat{\sigma}_x \cos(\alpha) - \hat{\sigma}_y \sin(\alpha)\big)\Big) \\ = \frac{\hbar\Omega V_0}{2} s(t)\big(\sin(\phi+\alpha)\hat{\sigma}_x + \cos(\phi+\alpha)\hat{\sigma}_y\big) & \\ = \widetilde{\mathcal{H}}'_d & \end{aligned} \tag{3.52}$$

In Eq. (3.42) shape of I and Q component has been fixed to lighten the derivation. Gnerally speaking it is convenient to work with the IQ components as time-varying signals. This does not change the core results, however when evaluating the unitary operator associated with a time varying sum of $\hat{\sigma}_x$ and $\hat{\sigma}_y$, a term should be added to compensate their non commutativity. Such term, $\mathcal{T}$ is known as the time ordering operator.

Physically, after shaping $I(t)$ and $Q(t)$, the signal is sent through the attenuation and filtering stages down to the QPU. Many system used to rely on analog IQ mixing, typical of RF engineering, nowadays RF signals are digitally synthetized on specialized hardware. This allows to reduce errors due to asymmetries in the I and Q channels, as well as delays in the lines and LO leakage due to a limited suppression of I and Q signals.

Control pulses are designed to be as short as possible, allowing as many quantum gates as possible to be executed within the limited coherence time of a qubit. Beside hardware limitations, a short pulse carries an high frequency content, therefore some components of its spectrum may excite the $|0\rangle \rightarrow |2\rangle$

transition. Therefore smooth envelopes with compact spectra, such as gaussian or rased cosine, are often employed. To reduce leakage to $|2\rangle$, it is possible to add the derivative of the pulse in the orthogonal component. Consider for example a $\hat{R}_x(\alpha)$ rotation, in combination with the $Q(t)$ pulse, the attenuated version of its derivative is sent on the other quadrature as shown in Figure 25. This technique is called Derivative Removal by Adiabatic Gate (DRAG) and it is a widely used pulse-shaping technique that enables faster quantum gates while suppressing leakage to non-computational states.

Formally, relation between quadratures is

$$I(t) = \frac{\lambda}{\alpha}\dot{Q} \tag{3.53}$$

Where α is the anharmonicity of the transmon and λ is result of a derivation when considering the 3-levels hamiltonian driven by a DRAG pulse. Theoretically speaking, $\lambda = \frac{1}{2}$ but because of deviations from the ideal model it usually needs some fine tuning.

It can be noticed that rotation induced by the derivative cancels out at the end of the execution and moreover the compensation amount is maximum when the slope (instantaneous frequency) increases. For the described example, pulses are defined as:

$$\begin{cases} Q(t) = e^{-\left(\frac{t^2}{2\sigma^2}\right)} \\ I(t) = \frac{\lambda}{\alpha}\frac{\mathrm{dQ}}{\mathrm{dt}} = -\frac{\lambda}{\alpha}\frac{t}{\sigma^2}e^{-\left(\frac{t^2}{2\sigma^2}\right)} \end{cases} \tag{3.54}$$

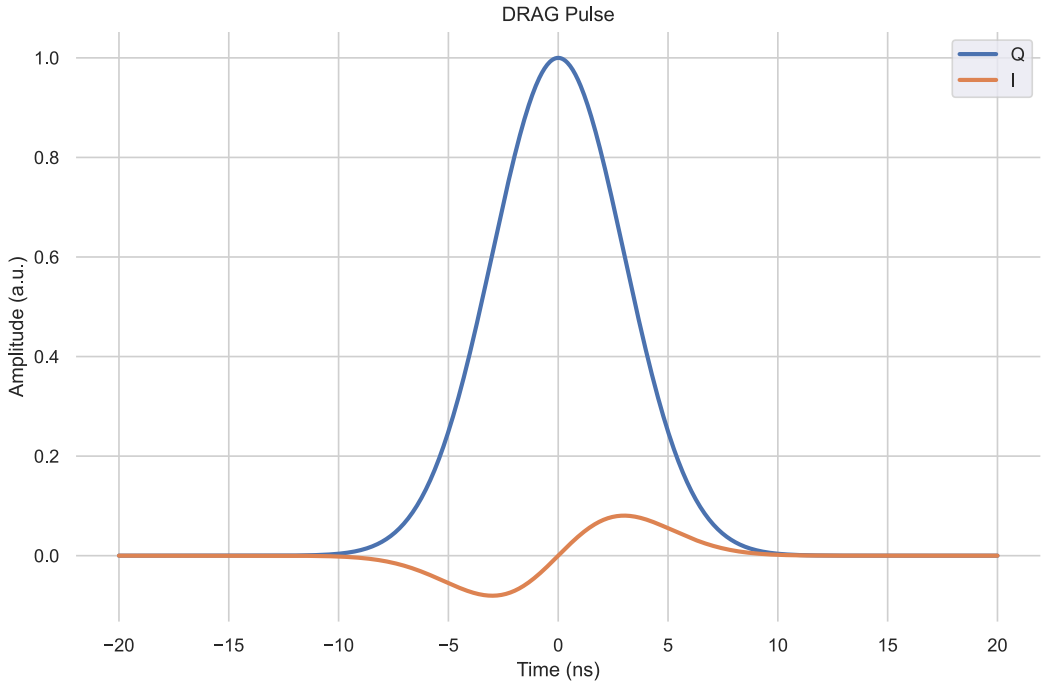


Figure 25: Example of a DRAG pulse for a $\hat{\sigma}_x$ rotation. The pulse lasts for 40 ns, on Q the gaussian shape with standard deviation 3, on I its derivative, considered anharmonicity of $\alpha = -200$ MHz.

3.4. Qubits Readout

To readout the state of the transmon qubit, a *probe line* (PB) is capacitively coupled to all qubits. Each PB-qubit coupling is mediated by a readout resonator (RR) and a Purcell filter (PF), to avoid strong interactions between the qubits and the PB. Both of the RR and PF are implemented as a coplanar waveguide, therefore their length defines the resonance frequency at which they will resonate. To occupy less chip space they are fabricated as $\lambda/4$ with meandering paths.

Operationally they can be seen as cascaded 1st order bandpass filters. This is shown in a quasi-lumped scheme reported in Figure 26.

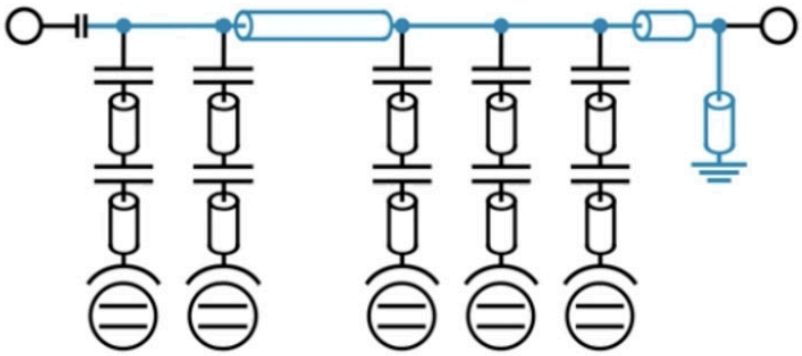


Figure 26: Quasi-lumped probe line scheme for *Lagrange*, qubits depicted as circles with two internal lines.
Image from [1]

The core idea beneath readout is to probe the resonator by sending a tone down to the PL and infer the state of the qubit by the distortion introduced and measured at the end of the PL.

This mechanism is known as *dispersive shift*. To understand it let us approximate the transmon as a perfect 2LS (energy of 3rd state $\to \infty$), its hamiltonian is:

$$\begin{aligned} \widehat{\mathcal{H}}_q &= \frac{1}{2}\omega_q \hat{\sigma}_z \\ &= \frac{1}{2}\omega_q (|0\rangle\langle 0| + |1\rangle\langle 1|) \end{aligned} \tag{3.55}$$

where ω_q is the resonance angular frequency of the qubit. The resonator can be described as a cavity in which photons with angular frequency ω_r live:

$$\widehat{\mathcal{H}}_r = \omega_r \left(\frac{1}{2} + \hat{a}^\dagger \hat{a} \right) \tag{3.56}$$

The hamiltonian describing the system is the sum of the two independent ones, with a term mediating their interaction: the qubit can be excited by absorbing the photon in the cavity or it can relax by emitting a photon in the cavity:

$$\begin{aligned} \widehat{\mathcal{H}} &= \hat{\sigma}_+ \hat{a} + \hat{\sigma}_- \hat{a}^\dagger \\ &= |1\rangle\langle 0|\hat{a} + |0\rangle\langle 1|\hat{a}^\dagger \end{aligned} \tag{3.57}$$

therefore by combining them:

$$\begin{aligned}\widehat{\mathcal{H}} &= \widehat{\mathcal{H}}_q + \widehat{\mathcal{H}}_r + g\widehat{\mathcal{H}}_{\text{int}} \\ &= \frac{1}{2}\omega_q\hat{\sigma}_z + \frac{1}{2}\omega_r\hat{a}^\dagger\hat{a} + g\big(\hat{\sigma}_+\hat{a} + \hat{\sigma}_-\hat{a}^\dagger\big)\end{aligned} \tag{3.58}$$

this is called *Jaynes-Cummings* hamiltonian and the g factor collects all terms contributing in the coupling strength between qubit and resonator.

Typically the readout is perfomed with a tone at much higher frequency with respect to the qubit, this is to prevent strong interactions (exciting or relaxing the transmon) but an interaction is still present and can be detected. For $\Delta = |\omega_q - \omega_r| \ll g$ the hamiltonian can be approximated in what is called *dispersive regime*:

$$\widehat{\mathcal{H}}_{\text{disp}} = (\omega_r \pm \chi\hat{\sigma}_z)\left(\frac{1}{2} + \hat{a}^\dagger\hat{a}\right) + \frac{1}{2}(\omega_q + \mp\chi)\hat{\sigma}_z \tag{3.59}$$

In this situation, the entangled system described by Eq. (3.58) is reduced to a shift in the energies of the qubit (*Lamb shift*) and in the resonator (*dispersive shift*) by a factor

$$\chi = \frac{g^2}{\Delta} \tag{3.60}$$

This result could be extended by also considering coupling to upper levels in the transmon, allowing to relax the 2LS hypothesis: hamiltonian of the transmon should take into account all three states with their energy:

$$\widehat{\mathcal{H}}_{\text{3LS}} = \omega_0|0\rangle\langle 0| + \omega_1|1\rangle\langle 1| + \omega_2|2\rangle\langle 2| \tag{3.61}$$

and by considering all the transitions mediated by a single photon in the interacting term, weighted by their coupling strenght:

$$\widehat{\mathcal{H}}_{\text{int}} = g_{01}\big(|1\rangle\langle 0|\hat{a} + |1\rangle\langle 0|\hat{a}^\dagger\big) + g_{12}\big(|2\rangle\langle 1|\hat{a} + |2\rangle\langle 1|\hat{a}^\dagger\big) \tag{3.62}$$

where two photon transitions are neglected, noticeably $g_{12} \approx g_{01}\sqrt{2}$. The remark is that, by considering the anharmonicity $\alpha = \omega_{12} - \omega_{01}$ the shift is

$$\chi \approx \frac{g_{01}^2\alpha}{\Delta(\Delta - \alpha)} \tag{3.63}$$

For the rest of the discussion, the transmon will be assumed as a 2LS, as all

relevant derivations can be performed with this hypothesis. What is important here is that if probing the system at ω_r allows to resolve if the system was in a $|0\rangle$ or a $|1\rangle$ state.

To maximise SNR a narrow linewidth in the resonator would be preferable, but the quality factor

$$Q = \frac{\omega_r}{\kappa_{\text{int}} + \kappa_{\text{ext}}} \tag{3.64}$$

the issue is that by increasing one of the two κ values (internal or external losses) heavily limits the coherence time of the qubit.

By analyzing the S_{21} scattering parameter, the phase is transmitted altered by a factor

$$\theta_{\pm} \approx \pm \tan^{-1}\left(2\frac{\chi}{\kappa_{\text{ext}}}\right) \mp \frac{\pi}{2} \tag{3.65}$$

leading to a typical working condition $\chi \approx \kappa_{\text{ext}}/2$.

This result is shown in the bottom left plot of Figure 27, in which the phase can be raised or lowered by the shift.

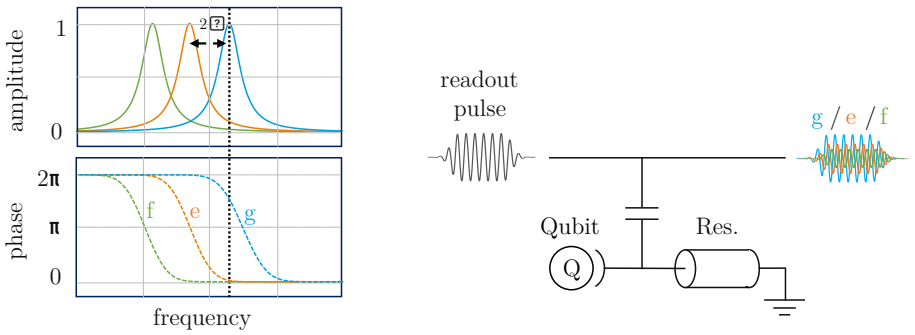


Figure 27: Dispersive shift in qubit readout.
Image from Zurich Instruments [12]

In modern systems, the signal is collected at the other end of the line where it meets a ultra fast analog to digital converter (ADC), see Figure 28. Then down conversion is performed and signal is filtered and integrated to result in a single complex-valued number.

$$S = \int_0^T (I(t) + iQ(t))W(t)\ \mathrm{dt} \tag{3.66}$$

Another possible technique is to use modulated matched filtering to directly embed the filtering and integration steps at the carrier frequency.

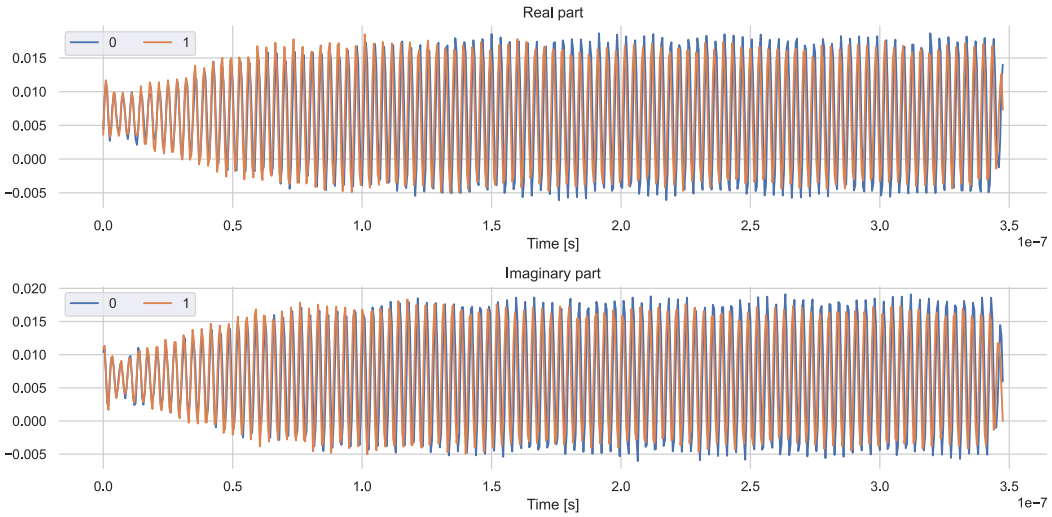


Figure 28: *Lagrange* averaged timetrace of the signal at the end of the PL showing both I and Q components for $|0\rangle$ and $|1\rangle$.

After points are collected, a discriminator function decides if the IQ value comes from a $|0\rangle$ or a $|1\rangle$. Such discriminator checks in which part of the IQ plane, divided by a straight line, the point is.

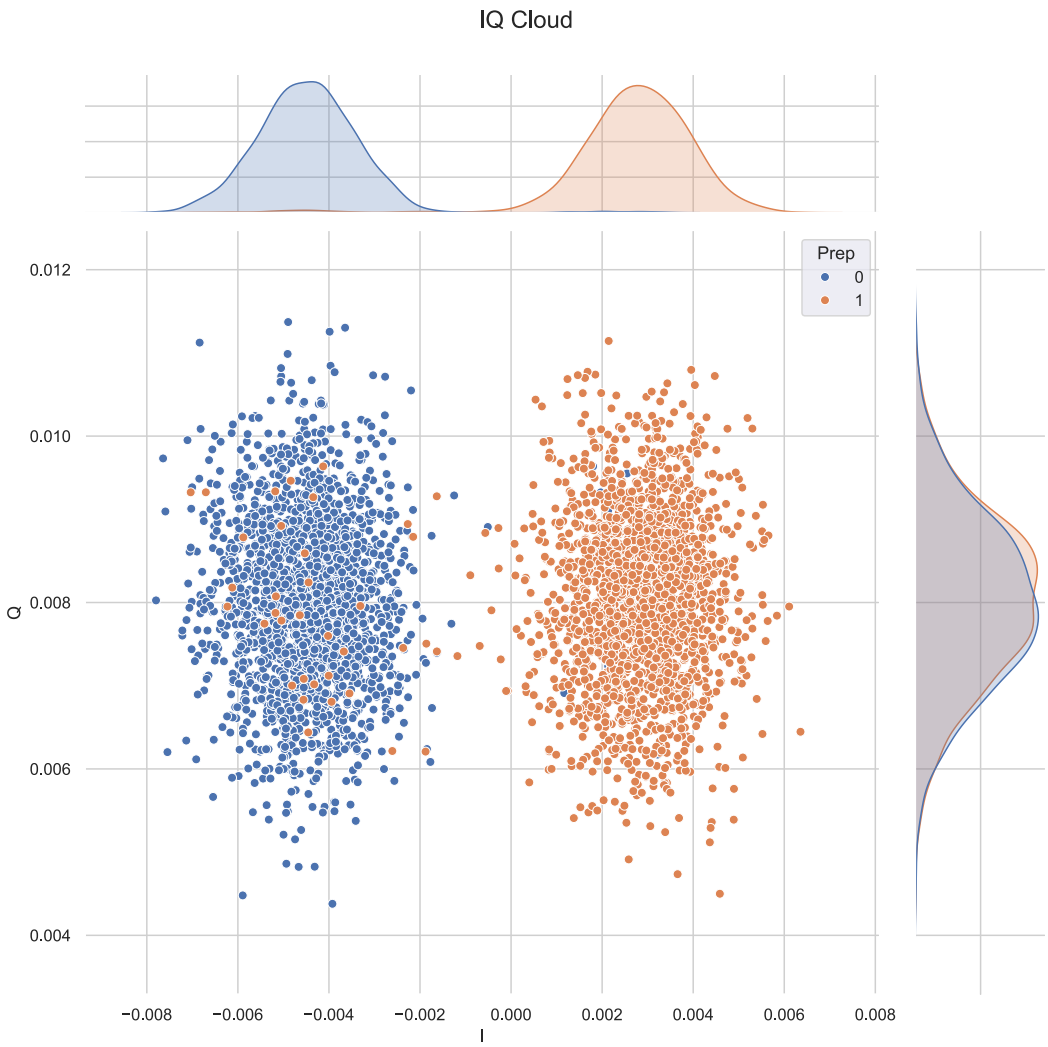


Figure 29: Integrated samples of several time traces of readouts perfomed on *Lagrange*.

3.5. The software stack

Executing quantum circuits on *Lagrange* can be done in different ways depending on the level of abstraction desired by the user. What at the end of the day matters for the quantum computer is receiving a sequence of controls to

send down to the QPU. This sequence of pulses represent quantum gates that can be directly executed on the QPU. Such gates compose what is known as the *native* gate set. A compilator orchestrates all the stages required to convert the quantum circuit into a sequence of pulses, usually also optimizing the final outcome.

Qiskit, Cirq and many more high-level libraries are supported by IQM python modules. Depending on the route one prefers to cross, the high-level circuit is processed in different ways. For example, considering Qiskit interoperability, compilation is dereferred to the compiler embedded in that external library.

Typically the compilation process is divided in passes, each with a specific purpose and some degree of optimization.
The first crucial decision a compiler must take is where to physically map qubits: it creates a translation table to associate physical objects (transmons, in our case) with their mathematical counterpart, the qubits. This step, known as *layout* is crucial since some qubit may need to perform several multi-qubit gates, therefore requiring high connectivity.

Whenever connectivity solutions do not allow for certain qubits to interact, the *routing* pass comes into play by placing costly `SWAP` operations so that all requested 2-qubit gates can be performed.

Then, typically, the translation pass is performed transforming mathematical gates into hardware available operations, for example an H gate decomposed as an application of R_z and a PRX.

Instead if one prefers to gain low-level control of gates and qubits, Pulla library offers the possibility to write sequences of operations and compile them into an executable job.

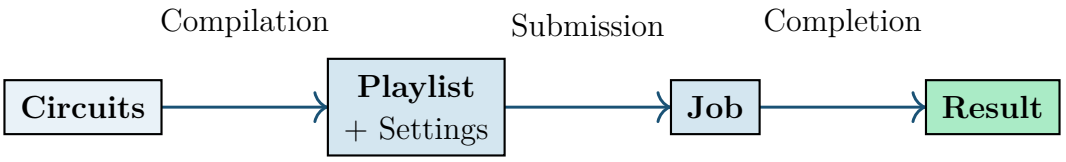


Figure 30: Main processing steps from the circuit definition to results extraction.

For the use case of *Lagrange*, authorized users can log with their credentials and download an access token valid for instantiating an `IQMClient` or a `Pulla`

object, both allowing to submit task to the backend where it will be scheduled for execution on the QPU.

When accessing pulse level defined jobs, users creates sequences of Operations each acting on one or more qubits (referred as *locus*) and sequentially combines them into a `Circuit` object. Such operations are native supported gates and measurement objects, each with its implementation. Pulla allows for defining different implementations for each operation. For IQM Spark quantum computers the native gate set is composed of $\mathrm{PRX}(\theta, \varphi)$, virtual z rotations R_z, CZ gate allowing two qubit operations and the measure primitive.

An `Operation` consists of a gate, the locus on which it acts and arguments, for example, to build the very basic entangling circuit implementing:

$$\mathrm{CX}_{1\to 2}\ \hat{H}_1|00\rangle = \frac{|00\rangle + |11\rangle}{\sqrt{2}} \tag{3.67}$$

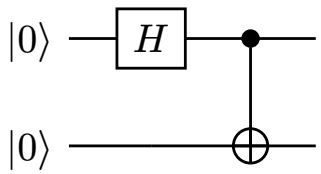


Figure 31: Entangling circuit.

it must be translated to native gates, this can be easily done by considering the following relation

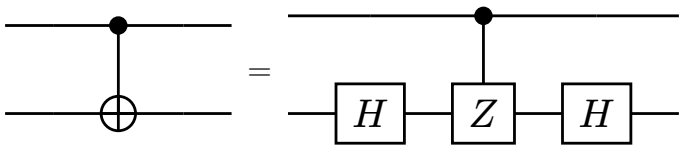


Figure 32: CX to CZ transformation.

and recalling that an H gate can be implemented as

$$\hat{H} = \mathrm{PRX}\Big(\frac{\pi}{2}, \frac{\pi}{2}\Big) R_{z(\pi)} \tag{3.68}$$

the circuit can be written as shown in Listing 1.

```python
from iqm.pulse import Circuit, CircuitOperation as Op
from numpy import pi

circuit = Circuit(
    name = "BellPair",
    instructions=(
        # H on QB1
        Op("rz", ("QB1",), args={"angle":pi}),
        Op("prx", ("QB1",), args={"angle":pi/2, "phase":pi/2}),

        # CX = IH CZ IH
        # H on QB3
        Op("rz", ("QB3",), args={"angle":pi}),
        Op("prx", ("QB3",), args={"angle":pi/2, "phase":pi/2}),
        # CZ
        Op("cz", ("QB1", "QB3")),
        # H on QB3
        Op("rz", ("QB3",), args={"angle":pi}),
        Op("prx", ("QB3",), args={"angle":pi/2, "phase":pi/2}),

        Op("measure", ("QB1", "QB3"), args={"key":"M"})
    )
)
```

Listing 1: Example of code to generate a Bell pair and measure it.

After the sequence of `Operations` is defined, they are collected in a `Circuit` which can be compiled. The compilation stage resolves all time dependencies, performs some optimization (such as deleting couples of adjacent gates that would cancel out), and most importantly, assigns for each control line its control signals.

These signals can be inspected with the `inspect_playlist()` method, generating an HTML page, as shown in Figure 33. There, single qubit gates implemented by PRX pulses can be seen, as well as how the flux line for the tunable coupler *TC-1-3* is biased to allow interaction between these two qubits.

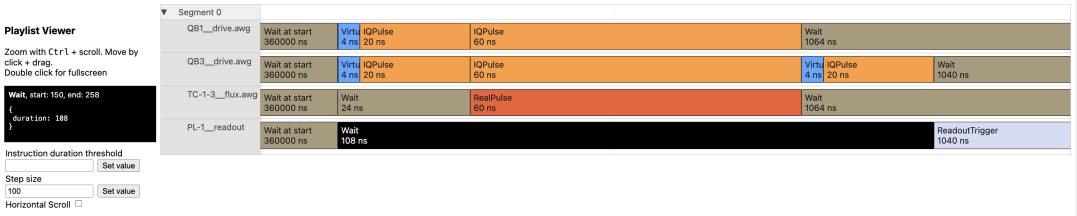


Figure 33: Generated HTML page inspecting a playlist implementing the circuit described in Listing 1.

When circuits are defined at such a low level, physical constraints are easily evaluated: to be valid the gate should have a valid implementation for that qubit, then upcoming gates will be executed afterwards, usually as soon as possible. Nonetheless when defining the circuit in this way no timing is considered, just sequentiality. These constraints are called TimeBoxes, recursive structures which are defined on a set of lines, a duration and their constraints.

What compiler still has to do is transforming such TimeBoxes into Schedules, containing information on when exactly pulses must be performed.

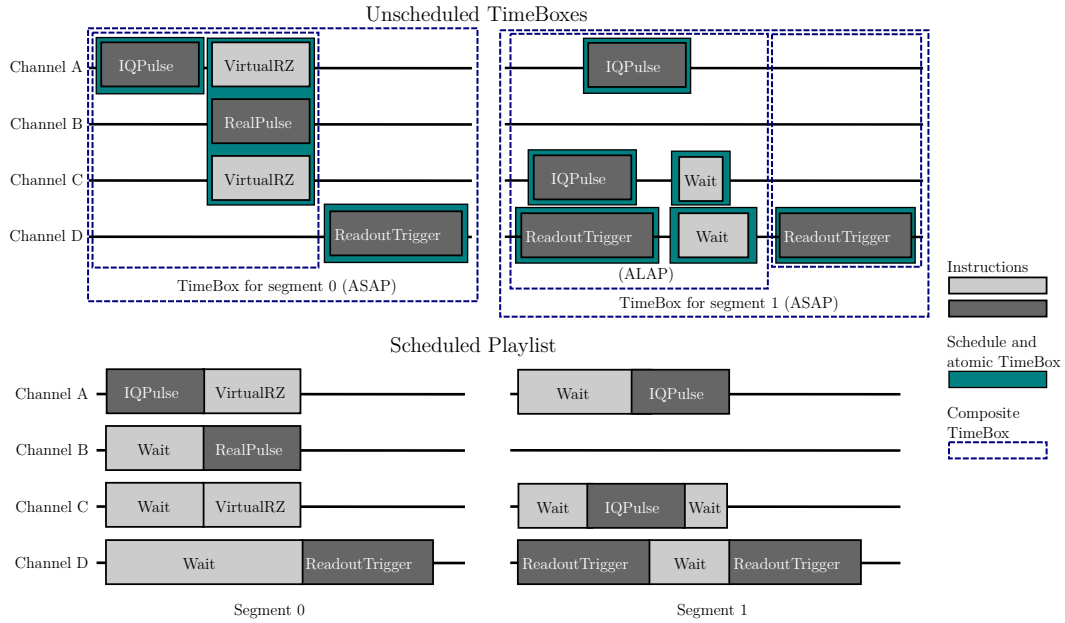


Figure 34: Example taken from [13] of TimeBoxes resolution.

Chapter 4
Experiments

In this chapter, a detailed description of the main principles behind each experiment is described. The first experiment aims to carefully analyze the reliability of measured results, preparing the ground for subsequent tests. Then, working at a physical level, the transition frequency of transmons is found by a spectroscopy. Characteristic times T_1, T_2^* and T_2 are derived by standardized experiments: Inversion Recovery(IR), Ramsey and Hahn-Echo. Finally gates quality is tested with three different experiments, from a very fast coarse test (All-XY) moving to more detailed experiments such as Randomized Benchmarking (RB) to have a rough idea of gates implementation quality. Finally some gates are specifically tested by means of the Interleaved Randomized Benchmarking (IRB) procedure.

4.1. SPAM Errors Characterization

4.1.1. Confusion Matrix

The confusion matrix can be characterized by preparing the basis states in the computational basis and measure them. This experiment needs the implicit hypothesis that $\hat{X}$ gates performed to prepare the $|1\rangle$ state are ideal.

For the case of *Lagrange*, it is possible and very convenient to characterize the whole confusion matrix Λ so it can be compared to the composition of single qubit ones Λ_i.

Then it is possible to apply the REM matrix to measured probability distribution of algorithms. In this context it is very useful to test how each basis state is affected, and hopefully corrected, by this post processing.

Finally, since sampling may lead to unphysical compensations (i.e. negative probabilities or exceeding sum), results are transformed by means of a Simplex Projection.

4.1.2. I-Q Cloud

Exploiting low level access to *Lagrange* it is possible to better characterize the readout results by analyzing measurements as points on the $I-Q$ plane (i.e. after their integration and before their discrimination). Having such values helps to evaluate SPAM errors, by allowing to separate them.

By sampling many states two clusters appear in the $I-Q$ plane: one referred to the $|0\rangle$ and the other to $|1\rangle$. These two *clouds* follow a normal distribution, in the general case each one has its own bivariate gaussian distribution. State preparation errors can be identified by checking for outliers in the distributions whereas measurements errors happens when the two clouds are too close each other, making discrimination harder and much more sensitive to fluctuations.

It is possible to evaluate the SNR at the end of the analog devices by evaluating how the two gaussians tails overlap. This is done by comparing the distance between the means with the variance of the signal:

$$\mathrm{SNR} = \frac{\|\overline{\mu}_1 - \overline{\mu}_0\|}{\sigma} \Longrightarrow \mathrm{SNR}_{\mathrm{power}} = \frac{\|\overline{\mu}_1 - \overline{\mu}_0\|^2}{\sigma^2} \tag{4.1}$$

To retrieve a comparable variance for the two distributions, the covariance matrices are projected on a single axis, allowing to retrieve a variance for each of them, then it is sufficient to average their variances. The axis on which distribution are projected is the signal axis

$$\overline{w} = \frac{\overline{\mu}_1 - \overline{\mu}_0}{\|\overline{\mu}_1 - \overline{\mu}_0\|} \tag{4.2}$$

therefore the variance is

$$\sigma_i^2 = \overline{w}^T \Sigma_i \overline{w} \Longrightarrow \sigma^2 = \frac{\sigma_0^2 + \sigma_1^2}{2} \tag{4.3}$$

Most of the noise is introduced by amplification steps, affecting uniformly both $|0\rangle$ and $|1\rangle$, therefore the two covariance matrices should be fairly identical $\Sigma_0 \approx \Sigma_1$.

Both I and Q signals are affected by the same noise in phase preserving amplifiers, therefore the Σ_i matrix should be mainly diagonal, ideally with no cross correlations among the two variables ($\Sigma_i \approx \sigma^2 \mathbb{I}$).

After having the two fitted gaussians, it is possible to find the line midway separating the space between them, therefore it is possible to evaluate the

probability for a point falling outside its region. This models a measurement error when considering only gaussian noise added to the point (i.e. neglecting measurement induced decays, T_1 relaxation…). Such probability can be evaluated as:

$$p_{\text{error}} = \frac{1}{2}\ \text{erfc}\left(\frac{\|\mu_1 - \mu_0\|}{2}\frac{1}{\sqrt{2}\sigma}\right) = \frac{1}{2}\ \text{erfc}\left(\frac{\text{SNR}}{2\sqrt{2}}\right) \tag{4.4}$$

4.2. Spectroscopy

This experiment aims to resolve the transition energy (i.e. frequency of the carrier microwave) to excite the $|0\rangle \rightarrow |1\rangle$ transition in the Transmon qubit.

This is fundamental to precisely control qubits reducing the detuning, causing unwanted rotations around the z axis.

Several techniques exist to resolve the frequency of a qubit, the *Two Tone Pulsed Spectroscopy* is here adopted for its ease of implementation. The transmon is prepared in $|0\rangle$, then a π pulse modulated at a frequency ω_d is applied and finally a measure is performed. This technique relies on having a precalibrated π, but does not require access to the continuous wave operation of control hardware. As discussed in Section 3.3, when a π pulse is applied at the exact same frequency of the qubit, it performs the transformation $|0\rangle \rightarrow |1\rangle$. When indeed ω_d is detuned, some spectral component of the drive pulse can still excite the $|0\rangle \rightarrow |1\rangle$ transition. A phenomenological approximation is here given, let us start by supposing to send a gaussian pulse with envelope

$$s(t) = \frac{1}{\sigma_t\sqrt{2\pi}}e^{-t^2/2\sigma_t^2} \tag{4.5}$$

so its spectral content has the exact same shape. The two level transmon can be approximated as a Dirac delta at ω_q. The overlap can be evaluated as

$$\begin{aligned} g_{\text{res}} &= \int_{-\infty}^{\infty} \frac{1}{\sigma\sqrt{2\pi}} e^{-(\omega-\omega_q)^2/2\sigma^2} \delta\big(\omega-\omega_q\big) d\omega \\ &= \frac{1}{\sigma\sqrt{2\pi}} \end{aligned} \tag{4.6}$$

It is important to notice that the introduced variable σ is the inverse of its time-domain counterpart denoted with t:

$$\sigma_t \sigma = 1 \tag{4.7}$$

Considering a γ factor that ensures the condition $\mathbb{P}(1) = 1$

$$\mathbb{P}(1) = \gamma g_{\text{res}} = 1 \Longrightarrow \gamma = \sigma\sqrt{2\pi} \tag{4.8}$$

When detuning the pulse by an amount ξ, the spectral overlap between the pulse and the qubit decreases following a gaussian like shape:

$$\begin{aligned} g_{\text{det}} &= \int_{-\infty}^{\infty} \frac{1}{\sigma\sqrt{2\pi}} e^{-(\omega-\omega_q+\xi)^2/2\sigma^2} \delta\big(\omega-\omega_q\big) d\omega \\ &= \frac{1}{\sigma\sqrt{2\pi}} e^{-\xi^2/2\sigma^2} \end{aligned} \tag{4.9}$$

Therefore, probability of measuring $|1\rangle$ follows:

$$\mathbb{P}(1,\xi) = e^{-\xi^2/2\sigma^2} \tag{4.10}$$

It is important to recall that this is a simple approximation: qubits have a finite linewidth concurring to spectral overlaps and moreover unwanted oscillations are induced when pulse carries too much energy.

It is crucial to also consider the Fourier limit, that is a fundamental limitation on the frequency resolution allowed with this technique. With a pulse lasting for t_p the minimum appreciable frequency difference is roughly

$$\Delta f = 1/t_p \tag{4.11}$$

which, for the gaussian shape can be linked to the Full Width at Half Maximum (FWHM) and ultimately to its standard deviation:

$$\text{FWHM} = 1/t_p = 2\sqrt{2\ln(2)}\sigma \tag{4.12}$$

As an example, using gaussian pulses 20 ns long, the expected linewidth is

$$\sigma = 1/\Big(t_p 2\sqrt{2\ln(2)}\Big) \approx 21 \text{ MHz} \tag{4.13}$$

4.3. Qubit coherence characterization

4.3.1. Inversion Recovery (T1)

To determin the T_1 characteristic time of amplitude damping process, the *inversion recovery* (IR) experiment is the standard: qubits are prepared in the $|1\rangle$ state and the system is left to idle for a time τ, then the state is measured.



Figure 35: Quantum circuit to perform IR experiment

Probability of measuring $|1\rangle$ should roughly follow the distribution reported in Eq. (2.44), exponentially decaying. To be more precise, an offset and a possible amplitude reduction should be considered resulting in

$$p_{|1\rangle}(\tau) = A + Be^{-\frac{\tau}{T_1}} \tag{4.14}$$

A is the probability of measuring $|1\rangle$ for $\tau \to \infty$, this value, close to 0, can be interpreted as the dark count rate, thermal equilibrium or statistically speaking false positives. For $\tau = 0$, probability of measuring the excited state is $A + B$, which is close to 1 but not exactly there because of several factors like imprecise π pulse or error in the measurement, but again it can be simply thought to be the true positive rate. B on its own carries very relevant information, being $B = p(0) - p(\infty)$ it represents the difference between the two extremes, how wide is the measuring window; it is also called *contrast* or *readout visibility*.
After measuring at different times the curve can be fitted. To comfortably propagate the uncertainty it is convenient to have a fixed amount of shots per delay time τ so the uncertainty on the estimated probability of excitation is described by the binomial distribution:

$$\sigma_i = \sqrt{\frac{y_i(1-y_i)}{N}} \tag{4.15}$$

To optimize the sampling space, it is possible to define two distinct regions: most of the variation happens in the first characteristic time T_1 then the rate of change slows down. After having a rough estimation of such parameter, a linear sampling space is defined from $0s$ to T_1 then a logarithmic one afterwards. A

second degree of freedom is the fraction of samples in the linear space and, therefore, the amount in the log one.

4.3.2. Ramsey experiment (T_2^*)

When characterizing the dephasing time, a distinction is done depending on the experiment performed to infer it. Following intuition from IR experiment, a change of basis can be performed to bring states in the Fourier basis and after a free evolution time, bring the states back on the computational basis to be measured. This can be conceptually thought as the $\hat{H}$ gate applied right before and after the idle time. For this experiment, characteristic time is referred as T_2^*.

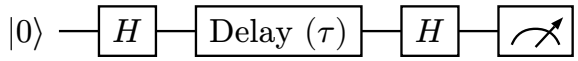


Figure 36: Quantum circuit to perform Ramsey experiment

This noise on the equatorial plane can be modeled as a phase flip acting with probability $p = \frac{1}{2}\left(1 - e^{-t/T_2^*}\right)$, following a white noise model. It should be noticed that noise may follow other distributions like a $1/f$ flicker noise and modeled by a gaussian shape $p = \frac{1}{2}\left(1 - e^{-(t/T_2^*)^2}\right)$.

In addition to this decay, unavoidable detuning ($\Delta\omega$) between qubit and pulses is present and causing a precession in the relative phase between $|0\rangle$ and $|1\rangle$. This difference evolves linearly, in proportion to the amount of detuning.

The first source of noise is an incoherent error whereas the latter is a coherent one, as it can be modeled by a unitary operation: $R_z(\Delta\omega t)$.

Recalling the phase flip Kraus operators:

$$\mathcal{E}_{\mathrm{PF}}(\rho) = (1 - p_z)\rho + p_z \hat{Z}\rho\hat{Z} \tag{4.16}$$

And defining the unitary evolution induced by the detuning as:

$$\hat{U}(\tau) = R_z(\Delta\omega\tau) = e^{-i\hat{Z}\Delta\omega\tau/2} \tag{4.17}$$

It can be noticed that these two operations commute, therefore they can be supposed as acting independently in parallel and the Kraus operators can absorb the unitary evolution terms:

$$\begin{aligned}\mathcal{E}(\rho,\tau) = \mathcal{E}_{\mathrm{PF}}\big(\hat{U}(\tau)\rho\hat{U}(\tau)^\dagger\big) = \\ = (1-p_z)\big(\hat{U}(\tau)\rho\hat{U}(\tau)^\dagger\big) + p_z\big(\hat{Z}\hat{U}(\tau)\rho\hat{U}(\tau)^\dagger\hat{Z}\big)\end{aligned} \tag{4.18}$$

By supposing the change of basis to happen fast enough (negligible with respect to the free evolution of the system), let us start with $\rho = |+\rangle\langle+|$ and see where the state will end.

By defining a common point in Eq. (4.18) as ρ':

$$\begin{aligned}\rho(\tau) = \hat{U}|+\rangle\langle+|\hat{U}^\dagger = R_z(\Delta\omega\tau)|+\rangle\langle+|R_z(-\Delta\omega\tau) = \\ = \frac{1}{2}\begin{pmatrix} 1 & e^{-i\Delta\omega\tau} \\ e^{i\Delta\omega\tau} & 1 \end{pmatrix}\end{aligned} \tag{4.19}$$

Action of $\hat{Z}$ on ρ' can be labeled as:

$$\rho'(\tau) = \hat{Z}\rho(\tau)\hat{Z} = \frac{1}{2}\begin{pmatrix} 1 & -e^{-i\Delta\omega\tau} \\ -e^{i\Delta\omega\tau} & 1 \end{pmatrix} \tag{4.20}$$

Therefore the free evolution of $|+\rangle$ state can be written down as

$$\begin{aligned}\mathcal{E}(|+\rangle\langle+|,\tau) = p_z\rho' + (1-p_z)\rho = \\ = \frac{1}{2}\begin{pmatrix} 1 & (1-2p_z)e^{-i\Delta\omega\tau} \\ (1-2p_z)e^{i\Delta\omega\tau} & 1 \end{pmatrix}\end{aligned} \tag{4.21}$$

Recalling the defined probability of phase flip:

$$p_z = \frac{1}{2}\big(1 - e^{-\tau/T_2^*}\big) \Longrightarrow (1-2p_z) = e^{-\tau/T_2^*} \tag{4.22}$$

Density matrix of the state after free evolution can be rewritten as:

$$\frac{1}{2}\begin{pmatrix} 1 & e^{-\tau/T_2^*}e^{-i\Delta\omega\tau} \\ e^{-\tau/T_2^*}e^{i\Delta\omega\tau} & 1 \end{pmatrix} \tag{4.23}$$

Therefore, after moving the state back to the computational basis the system will be in

$$\begin{aligned}\rho_f = \hat{H}\mathcal{E}(|+\rangle\langle+|,\tau)\hat{H} = \\ = \frac{1}{2}\begin{pmatrix} 1+\cos(\Delta\omega\tau)e^{-\frac{\tau}{T_2^*}} & i\sin(\Delta\omega\tau)e^{-\frac{\tau}{T_2^*}} \\ -i\sin(\Delta\omega\tau)e^{-\frac{\tau}{T_2^*}} & 1-\cos(\Delta\omega\tau)e^{-\frac{\tau}{T_2^*}} \end{pmatrix}\end{aligned} \tag{4.24}$$

Therefore probability of measuring the $|1\rangle$ state is

$$\mathbb{P}(|1\rangle)(\tau) = \langle 1|\rho_f|1\rangle = \frac{1}{2} - \frac{1}{2}\cos(\Delta\omega\tau)e^{-\frac{\tau}{T_2^*}} \tag{4.25}$$

This result allows to combine and estimate effects of detuning ($\Delta\omega$) and phase decoherence T_2^*. Moreover, a more general expression can be introduced to take into account SPAM errors, allowing for for better fitting.

$$\mathbb{P}(|1\rangle)(\tau) = A + B\cos(\Delta\omega\tau)e^{-\frac{\tau}{T_2^*}} \tag{4.26}$$

4.3.3. Hahn-Echo (T_2)

To remove the sinusoidal term introduced in the Ramsey experiment, a *refocusing* pulse can be used. The main reason for the oscillations of Ramsey experiment is tipically a static magnetic field altering qubit's resonance frequency, therefore having an unwanted rotation around z axis: $\hat{R}_z(\Delta\omega t)$.

By switching the direction of the magnetic field with respect to the Bloch sphere, the state rotates in the opposite direction. Unfortunately this magnetic field is often an unwanted effect, on which there is no control. What can be done is to "rotate the Bloch sphere" or, to keep a static reference, rotate the state.

Now, the idea is simple: to cancel out rotation induced by the static field it is sufficient to let the state evolve freely for a time $\tau/2$, apply this rotation and again wait for the remaining $\tau/2$ time so that the static field counter rotates the state.

A pictorial representation of the key evolution moments is reported in Figure 37, where a combination of $\hat{R}_x$ and $\hat{R}_y$ gates is used, instead of the $\hat{H}$ gate. Beside this choice of gates it illustrates the core idea of the experiment.

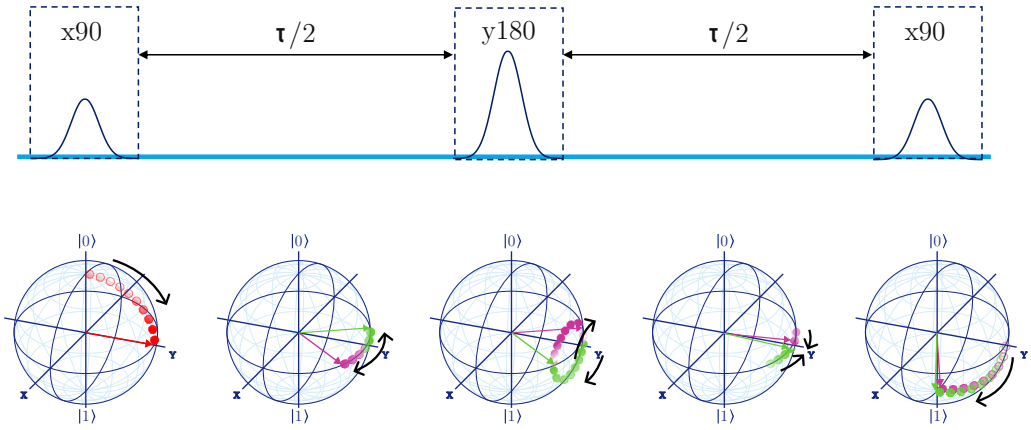


Figure 37: Hahn-Echo experiment key moments, image from Zürich Instruments. [14]

When measuring the state in the computational basis, the probability of an excited state can be evaluated similarly as the Ramsey experiment without the sinusoidal term:

$$\mathbb{P}(|1\rangle)(\tau) = \frac{1}{2} - \frac{1}{2}e^{-\frac{\tau}{T_2}} \tag{4.27}$$

By suppressing the sinusoidal term it is possible to perform hybrid sampling, as for the inversion recovery experiment.

For the sake of fitting stability, and to take into account SPAM errors, it is again convenient to include the degrees of freedom for the dark count rate A and contrast B.

$$\mathbb{P}(|1\rangle)(\tau) = A + Be^{-\frac{\tau}{T_2}} \tag{4.28}$$

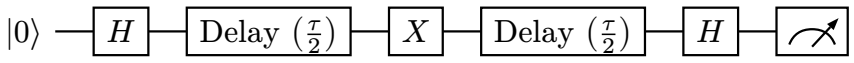


Figure 38: Quantum circuit to perform Hahn-Echo experiment.

4.4. Gates characterization

4.4.1. All-XY

The All-XY protocol aims for a lightweight, fast, gate characterization. Specifically, it aims to detect and roughly quantify coherent errors occurring during gates execution. It is useful to have a first rough evaluation of gate quality before spending many QPU time on specialized protocols as RB or GST to better characterize gates.

All-XY is composed by 21 quantum circuits, each of them made by just 2 gates carefully picked among:

$$\left\{X_\pi, Y_\pi, X_{\pi/2}, Y_{\pi/2}, \mathbb{I}\right\} \tag{4.29}$$

Detailed composition of the sequences is reported in Table 6, Table 7 and Table 8. Such circuits are collected in 3 distinct classes, based on the expected probability of measuring $|1\rangle$ which is designed to be either $0, 0.5$ or 1.

It can be noticed that, despite in principle there are $5^2 = 25$ sequences, All-XY is composed by 21 of them. In fact, the identity matrix is considered as a first gate only in Seq#1 in which it serves as baseline for evaluating SPAM errors ($\mathbb{P}(1|0)$).

In Seq#18 and Seq#19 the true positive probability can be evaluated $\mathbb{P}(1|1)$.

Sequence#	**1**	**2**	**3**	**4**	**5**
Pulse 1	$\mathbb{I}$	X_π	Y_π	X_π	Y_π
Pulse 2	$\mathbb{I}$	X_π	Y_π	Y_π	X_π
$\mathbb{P}_1$	0	0	0	0	0

Table 6: All-XY sequences with $\mathbb{P}_1 = 0$.

Sequence#	**6**	**7**	**8**	**9**	**10**	**11**	**12**	**13**	**14**	**15**	**16**	**17**
Pulse 1	$X_{\pi/2}$	$Y_{\pi/2}$	$X_{\pi/2}$	$Y_{\pi/2}$	$X_{\pi/2}$	$Y_{\pi/2}$	X_π	Y_π	$X_{\pi/2}$	X_π	$Y_{\pi/2}$	Y_π
Pulse 2	$\mathbb{I}$	$\mathbb{I}$	$Y_{\pi/2}$	$X_{\pi/2}$	Y_π	X_π	$Y_{\pi/2}$	$X_{\pi/2}$	X_π	$X_{\pi/2}$	Y_π	$Y_{\pi/2}$
$\mathbb{P}_1$	0.5	0.5	0.5	0.5	0.5	0.5	0.5	0.5	0.5	0.5	0.5	0.5

Table 7: All-XY sequences with $\mathbb{P}_1 = 0.5$.

Sequence#	**18**	**19**	**20**	**21**
Pulse 1	X_π	Y_π	$X_{\pi/2}$	$Y_{\pi/2}$
Pulse 2	$\mathbb{I}$	$\mathbb{I}$	$X_{\pi/2}$	$Y_{\pi/2}$
$\mathbb{P}_\mathbf{1}$	1	1	1	1

Table 8: All-XY sequences with $\mathbb{P}_1 = 1$.

After collecting circuit results they are methodically plotted in order with a bar plot. This allows to define the profile of the experiment, that ideally should be a step function: 0 for the first 5 experiments, 0.5 for the middle 12 and 1 for the remaining 4. By analyzing the deviation from this step, it is possible to infer information about the system performance.

Consider for example an extra phase term accumulating between two pulses. This can be analyzed by considering the 5 pairs: $(8,9),(10,11),(12,13),(14,15),(16,17)$. Such pairs consist of a $R_x(\alpha)$ followed by a $R_y(\beta)$ and its swapped version.

Among the aforementioned pairs, let us analyze $(8,9)$; if an extra phase is introduced they can be recast as:

$$\begin{cases} |\psi_{\#8}\rangle = R_y(\frac{\pi}{2})R_z(\theta_z)R_x(\frac{\pi}{2})|0\rangle \\ |\psi_{\#9}\rangle = R_x(\frac{\pi}{2})R_z(\theta_z)R_y(\frac{\pi}{2})|0\rangle \end{cases} \tag{4.30}$$

This evolution leads to

$$\begin{cases} |\psi_{\#8}\rangle = \frac{1}{2}\Big((1+ie^{i\theta_z})|0\rangle + (1-ie^{i\theta_z})|1\rangle\Big) \\ |\psi_{\#9}\rangle = \frac{1}{2}\Big((1-ie^{i\theta_z})|0\rangle + (-i+ie^{i\theta_z})|1\rangle\Big) \end{cases} \tag{4.31}$$

Therefore, probability of measuring $|1\rangle$ is:

$$\begin{cases} \mathbb{P}(1)_{\#8} = \frac{1}{2}(1+\sin(\theta_z)) \\ \mathbb{P}(1)_{\#9} = \frac{1}{2}(1-\sin(\theta_z)) \end{cases} \tag{4.32}$$

Therefore it is possible to evaluate coherent phase error as:

$$\theta_z = \sin^{-1}\big(\mathbb{P}(1)_{\#8} - \mathbb{P}(1)_{\#9}\big) \tag{4.33}$$

Similar reasoning can be performed on all interested pairs of sequences. When plotting this in an ordered bar plot, a zig-zag pattern of amplitude $\sin(\theta_z)$ will be present in sequences $\#8 - \#17$.

Consider now Seq#6, supposing an over rotation of ϵ. Instead of applying $R_x(\theta)$ the resulting gate is $R_x(\theta(1+\epsilon))$. The state simply evolves as

$$|\psi_{\#6}\rangle = R_x\Big(\frac{\pi}{2}(1+\epsilon)\Big)|0\rangle \tag{4.34}$$

leading to

$$\mathbb{P}(1)_{\#6} = 1 - \sin^2\Big(\frac{\pi}{4}(1+\epsilon)\Big) = \frac{1}{2} + \frac{1}{2}\sin\Big(\frac{\pi}{2}\epsilon\Big) \tag{4.35}$$

which can be conveniently linearized supposing the error to be small:

$$|\psi_{\#6}\rangle = \frac{1}{2} + \frac{\pi}{4}\epsilon \tag{4.36}$$

Analogously, supposing for Seq#10 the same error affecting orthogonal operations and defining effective rotations

$$\theta_x = \frac{\pi}{2} + \epsilon \qquad \theta_y = \pi + \epsilon \tag{4.37}$$

the state evolves as

$$|\psi_{\#10}\rangle = R_y(\theta_y)R_x(\theta_x)|0\rangle \tag{4.38}$$

Therefore the probability of measuring the excited state is

$$\mathbb{P}(1)_{\#10} = \sin^2\left(\frac{\theta_x}{2}\right)\cos^2\left(\frac{\theta_y}{2}\right) + \cos^2\left(\frac{\theta_x}{2}\right)\sin^2\left(\frac{\theta_y}{2}\right) \tag{4.39}$$

Defining a convenient way to parametrize the error:

$$\delta_x = \frac{\pi}{4}\epsilon \qquad \delta_y = \frac{\pi}{2}\epsilon \tag{4.40}$$

Eq. (4.39) becomes

$$\begin{aligned}\mathbb{P}(1)_{\#10} &= \sin^2\Big(\frac{\pi}{4}+\delta_x\Big)\cos^2\Big(\frac{\pi}{2}+\delta_y\Big) + \cos^2\Big(\frac{\pi}{4}+\delta_x\Big) + \sin^2\Big(\frac{\pi}{2}+\delta_y\Big) \\ &= \sin^2\Big(\frac{\pi}{4}+\delta_x\Big)\sin^2(\delta_y) + \cos^2\Big(\frac{\pi}{4}+\delta_x\Big) + \cos^2(\delta_y) \\ &\approx \Big(\frac{1}{2}+\delta_x\Big)\delta_y^2 + \Big(\frac{1}{2}-\delta_x\Big)(1-\delta_y^2)\end{aligned} \tag{4.41}$$

By supposing errors to be small enough the trigonometric terms are expanded to their second order term. Then, by considering only linear terms, probability of measuring an excited state will be:

$$\mathbb{P}(1)_{\#10} \approx \frac{1}{2} - \delta_x = \frac{1}{2} - \frac{\pi}{4}\epsilon \tag{4.42}$$

Similar reasoning can be done for Seq#14 (or Seq#15), for which probability of measuring $|1\rangle$, under the rotation error ϵ, is

$$\mathbb{P}(1)_{\#14} \approx \frac{1}{2} + \frac{3\pi}{4}\epsilon \tag{4.43}$$

By comparing Eq. (4.36), Eq. (4.42) and Eq. (4.43) it is possible to find the angle ϵ affecting the gates. The exact same approach allows to derive the same result considering sequences starting with R_y.

Moreover sequences Seq#10 - Seq#13, composed by unbalanced rotations on different axis can be used to tune DRAG pulses.

4.4.2. Randomized Benchmarking

Randomized Benchmarking (RB) aims to evaluate the average gate quality for gates in the Clifford group. This limit is intrinsically dictated by the experimental procedure: classical simulability must always be possible. To understand why this is mandatory, let us see how the experiment is constituted.

In this context, the depth of the circuit is the amount of applied gates $\hat{U}_i \in \mathcal{C}_n$, therefore no optimization is performed so that the number of gates is exactly m. The resulting circuits are therefore in the form of

$$\hat{U}_m = \prod_{i=1}^{m} \hat{U}_i \tag{4.44}$$

For such circuit, it is computationally easy to evaluate its inverse $\hat{U}^\dagger$ to bring the state back to $|0\rangle$. To build the sequence $\hat{U}_i$, gates are uniformly sampled from $\mathcal{C}_m$.

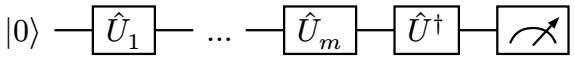


Figure 39: Quantum circuit for the RB experiment.

Eq. (4.44) describes an ideal quantum circuit, indeed each gate may have an error. By assuming the same error $\mathcal{E}$ acting on each gate the circuit is written as:

$$\prod_{i=1}^{m} \mathcal{E}\left(\hat{U}_i\right) \tag{4.45}$$

Considering an error and evaluating it on all the gates in the Clifford group, allows to build an average error. The procedure of applying the same error to the whole group is also called *twirling*.

$$\mathcal{E}_{\text{twirl}} = \frac{1}{\|\mathcal{C}_n\|} \sum_{\hat{U} \in \mathcal{C}_n} \hat{U}^\dagger \mathcal{E} \hat{U} \tag{4.46}$$

A nice feature of this error is that it models exactly a depolarizing error, depending therefore only on the probability p_d. By preparing a large enough batch of K circuits, one for each sweep of $m \in [1...M]$, it is possible to average the $\mathcal{E}$ into the twirled error $\mathcal{E}_{\text{twirl}}$.

For all circuits in the k-th batch, the probability of correct execution (measuring 0) is measured. Supposing each gate has a probability p_d of being faulty, after m gates the probability of not having any faulty gates is p_d^m. Therefore, after collecting results, the per-gate average error can be evaluated by fitting

$$\mathbb{P}(0) = Ap^m + B \tag{4.47}$$

Remarkably, this procedure allows to focus on the gate characterization, collecting SPAM errors in A and B coefficients, so that all the relevant information for quantum gates is in p.

Finally, the average error per gate r is found:

$$r = \frac{d-1}{d}(1-p) \tag{4.48}$$

Here d is the dimension of the hilbert space, for n qubits $d = 2^n$.

Once this value has been found, it is possible to evaluate the mean time to failure by looking at the geometric distribution with probability r:

$$\mathbb{P}(k) = (1-r)^{k-1} r \tag{4.49}$$

This distribution gives the probability that the depolarization error happens in the first k gates. The expected value of such distribution returns the average number of attempts before the first success

$$\mathbb{E}(\text{Geom}(r)) = \frac{1}{r} \tag{4.50}$$

This value can be therefore interpreted as the maximum circuit size, when considering only tested gates. Moreover, a correcting term should be taken into account to match the mathematical abstraction to the physical quantum gates implementation: in superconducting technologies Z gates are free but CX require more gates. It is therefore introduced the distinction between Error Per Gate (EPG) and Error Per Clifford (EPC). The conversion factor between these two quantities is exactly the average amount of pulses to implement a Clifford gate.

As an example, $\mathcal{C}_1$ has 24 elements, among which there is the identity, the 180° hat(Z) and the ±90° hat(Z) which are all istantaneous and perfect gates. Therefore the average number of pulses per Clifford gate for 1-qubit gates with this technology is $\frac{20}{24} \approx 0.833$.

4.4.3. Interleaved Randomized Benchmarking

RB allows to extract a gate fidelity averaged on all gates from the Clifford group. If instead one is interested in a specific gate, Interleaved Randomized Benchmarking (IRB) allows to extract the average gate fidelity for that specific Gate Under Test (GUT).

The experiment is rather similar to RB as it consists of running batches of k circuits each, for various depths m. Then survival probability of $|0\rangle$ is fitted with Eq. (4.47).

The nuance that allows to analyze single gates resides in the procedure to build the circuit: between each uniformly sampled Clifford gate, the GUT is inserted. This interleaving pattern breaks the hypothesis of isotropic noise acting on the circuit, errors will be strongly biased from GUT quality.

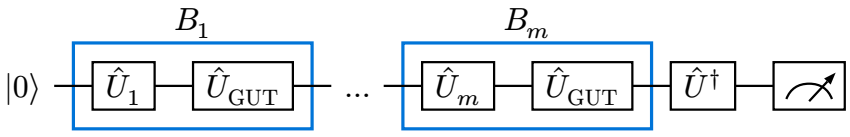


Figure 40: Quantum circuit for the IRB experiment.

To write out the circuit, let us start by writing noisy gates as

$$\tilde{U}_i = \mathcal{E}\big(\hat{U}_i\big) \qquad \tilde{U}_{\mathrm{T}} = \mathcal{E}_{\mathrm{T}}\big(\hat{U}_{\mathrm{T}}\big) \tag{4.51}$$

where $\mathcal{E}_{\mathrm{T}}$ is the specific noise for the GUT.

For ease of notation, let us upgrade the operators of the statevector notation to their equivalent superoperators acting on density matrices.

$$\hat{U} \to \mathcal{U}(\rho) = \hat{U}\rho\hat{U}^\dagger \Longrightarrow \tilde{\mathcal{U}} = \mathcal{E} \circ \mathcal{U} \tag{4.52}$$

Each block B is therefore:

$$\begin{aligned} B &= \tilde{\mathcal{U}}_T \tilde{\mathcal{U}}_i \\ &= \mathcal{E}_T \circ \mathcal{U}_T \circ \mathcal{E}_i \circ \mathcal{U}_i \\ &= \mathcal{E}_T \circ \mathcal{U}_T \circ \mathcal{E}_i \circ \mathcal{U}_T^{-1} \circ \mathcal{U}_T \circ \mathcal{U}_i \end{aligned} \tag{4.53}$$

It is possible to define a gate $\hat{U}_i' = \hat{U}_T \hat{U}_i$ which, being the product of elements of $\mathcal{C}$, must be itself in the Clifford group and moreover, being the product of a fixed gate with a uniformly sampled one, results in a uniformly sampled gate of $\mathcal{C}_n$.

$$B = \mathcal{E}_T \circ \left(\mathcal{U}_T \circ \mathcal{E}_i \circ \mathcal{U}_T^{-1}\right) \circ \mathcal{U}_i' \tag{4.54}$$

The part of the block B in the parenthesis can be seen as a change of basis for the noise acting on all gates, as it would be perceived in the GUT perspective. Ultimately, it is possible to pack the two errors in a single one

$$\mathcal{E}_i' = \mathcal{E}_T \circ \left(\mathcal{U}_T \circ \mathcal{E}_i \circ \mathcal{U}_T^{-1}\right) \Longrightarrow B = \mathcal{E}_i' \circ \mathcal{U}_i' \tag{4.55}$$

Supposing the noise acting on GUT as a depolarizing error with probability p_T, then thanks to the twirling process $\mathcal{E}_i$ averages as a depolarizing error too. Therefore $\mathcal{E}_i'$ is also a depolarizing error with probability

$$p' = p \cdot p_T \tag{4.56}$$

After performing a RB experiment, resolving its probability p and the IRB with its probability p', it is possible to evaluate the probability associated to the GUT:

$$p_T = \frac{p'}{p} \tag{4.57}$$

Then, akin to RB, it is possible to compute the average GUT fidelity:

$$F_T = 1 - \frac{d-1}{d}\left(1 - \frac{p'}{p}\right) \tag{4.58}$$

This result is obtained by approximating the GUT error as a depolarizing channel, that is not always the case but as shown in [3] the error associated to this approximation is bounded and decreases for better gates.

Chapter 5
Implementation and Results

In this chapter, details needed to execute and reproduce previously described experiments are given. Results of execution on *Lagrange* are reported, accompanied by relevant considerations.

5.1. SPAM Errors

5.1.1. Confusion Matrix

For the local matrices, qubits are prepared in $|0\rangle$ or in $|1\rangle$, all in separate experiments, and measured to resolve the local confusion matrices. Pseudo inverse matrix Λ_i^{-1} is evaluated to ensure stability of the algorithm. Then to evaluate how well the algorithm performed, each qubit is prepared and measured once again this time adding as a post processing step the multiplication by Λ_i^{-1}. Finally, simplex projection is performed to ensure probabilities validity and results are plotted (Figure 41).

Analogously, the 32 basis states for the 5 qubits are prepared and measured keeping track of the distribution, to fill the global confusion matrix. Measures are multiplexed, as it would likely be in a real world scenario. Then the pseudoinverse Λ^{-1} is evaluated and used with a whole new set of measures to compare how the matrix corrects each element of the basis (Figure 42).

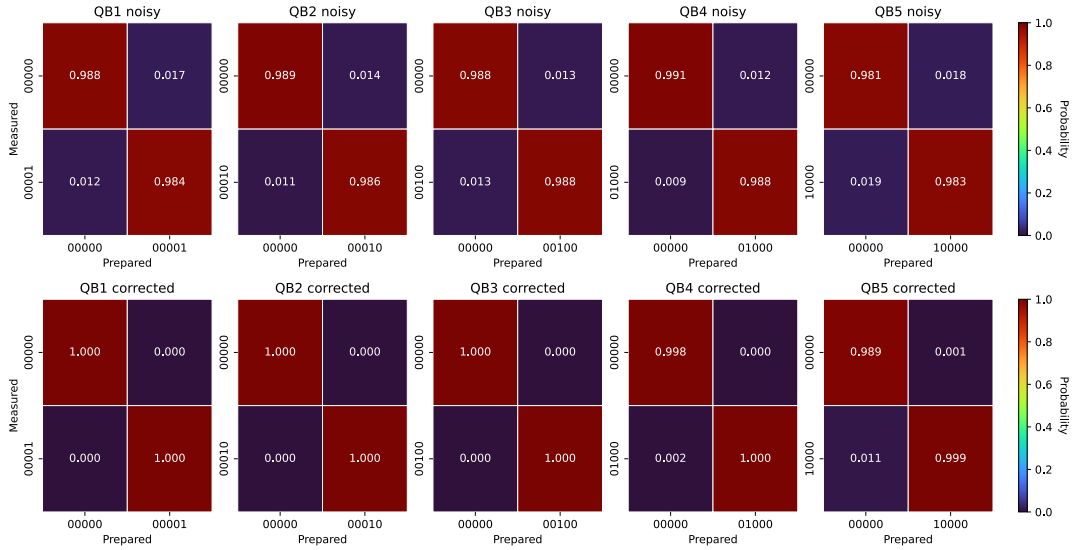


Figure 41: Top: Measure local confusion matrices.
Bottom: New set of measures after applying REM.

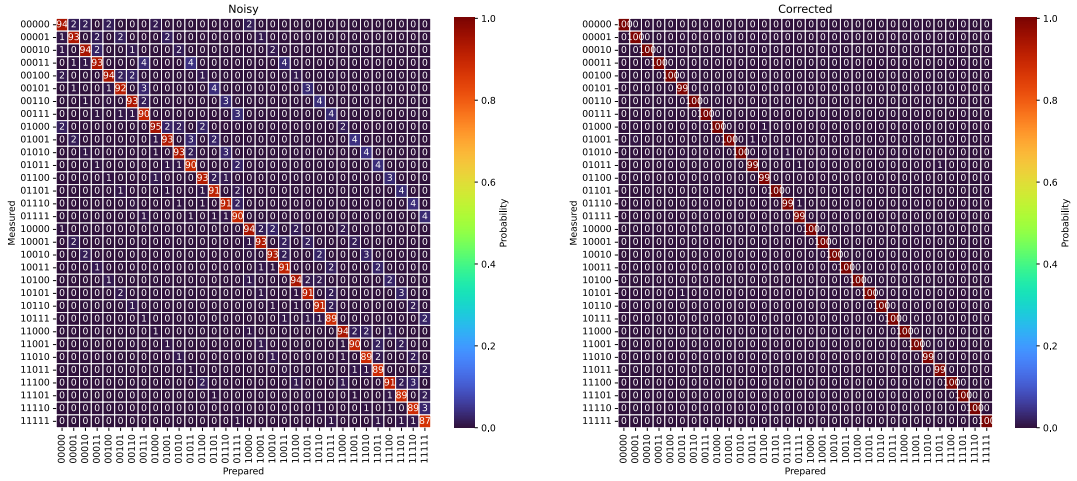


Figure 42: Left: Measured global confusion matrix for all qubits (values in percent points).
Right: New set of measures after applying REM.

As a last step, inverses of local matrices are combined together by a tensor product to obtain a post processing step that could be applied to the whole system with a reduced computational cost and occupying smaller memory,

aiming to a scalable scenario. The tradeoff is well appreciable in Figure 43 where the composite of local matrices is applied to correct global measurements.

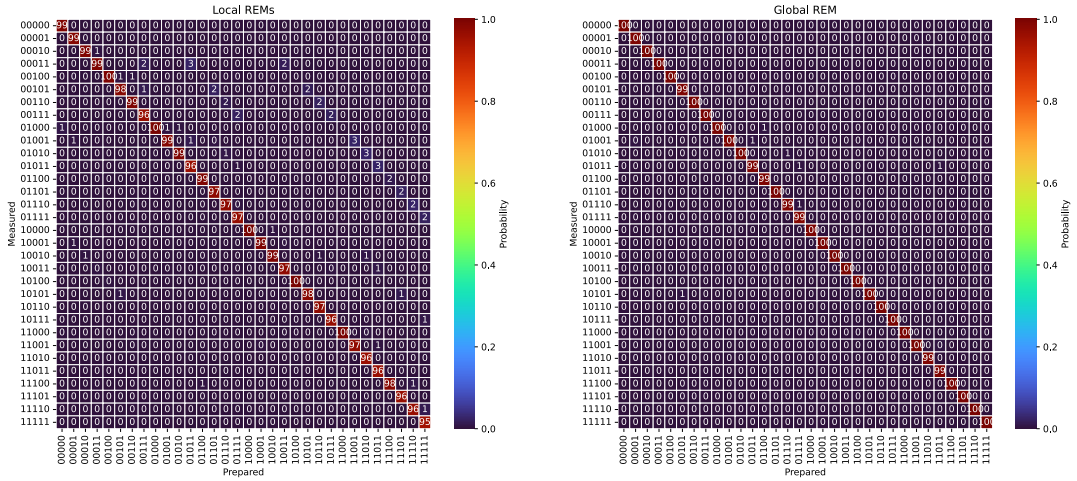


Figure 43: Left: REM applied with composition of local matrices. Right: REM applied with a global matrix.

In all the cases, an overall improvement is clearly visible, with best results for the REM performed with a global matrix. Comparing the results obtained with the composition of local matrices with respect to the ones obtained with a global one, few percent points are lost. These off diagonal elements are caused by correlations in measurements, and impossible to correct with composition of independent matrices. Nevertheless this lightweight approach improves results quality.

5.1.2. I-Q Cloud

States $|0\rangle$ and $|1\rangle$ are prepared on a qubit and then measured as complex numbers (values on the $I-Q$ plane) by accessing low level control of *Lagrange* exposed by the `pulla` library.

Two gaussians are fitted with the two sets of results (prepared states). From the covariance matrices, along with their mean on the $I-Q$ plane, the relative variance for each of the two distribution is evaluated:

$$\sigma_0^2 = 1.365 \cdot 10^{-6} \qquad \sigma_1^2 = 1.973 \cdot 10^{-6} \tag{5.1}$$

Resulting in an effective variance of: $\sigma^2 = 1.669 \cdot 10^{-6}$, and the distance between the means is $\|\mu_1 - \mu_0\| = 7.152 \cdot 10^{-3}$ evaluating the SNR as Eq. (4.1) results in $\text{SNR} = 4.285 \cdot 10^3$.
Finally the probability for a state to fall outside its region is evaluated as Eq. (4.4): $p_{\text{err}} = 0.282\%$.

In Figure 44 many kinds of information is reported: scatter plot of measurements on the $I - Q$ plane, their marginals distributions, fitted multivariate gaussians and with $\mathbf{x}$ marks the two mean points. Contour lines are linear divisions of the range of the distribution.

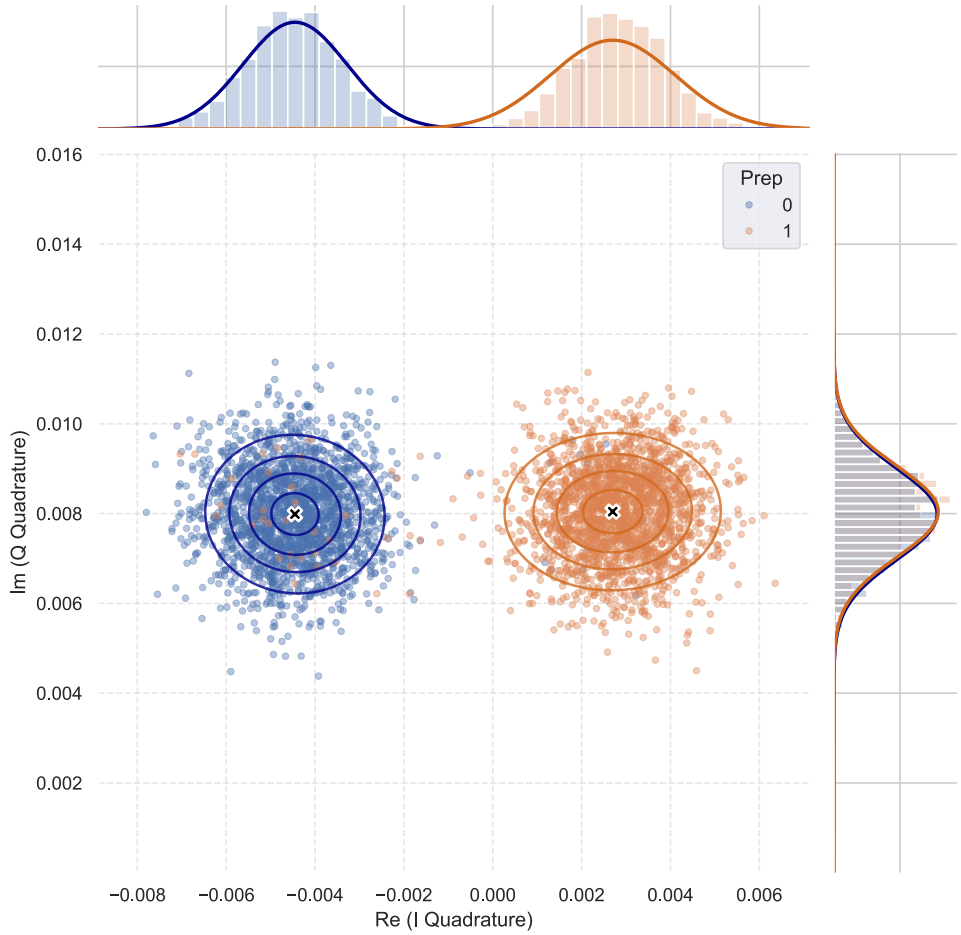


Figure 44: Scatter plot with marginal histograms and fitted normal distributions on the IQ plane, axis in arbitrary units.

Analyzing the presence of measured 1s in the prepared $|0\rangle$ region and vice versa it is possible to qualitatively appreciate the amount of state preparation errors, this data is quantitatively reported in the off-diagonal elements of the confusion matrix.

5.2. Spectroscopy

In the default implementation, `IQM Pulse` uses a CRF waveform to shape the PRX pulse. Nevertheless model derived in Section 4.2 offers a good approximation that can be used to describe measured results.

The experiment is conveniently prepared with the `Sweep` object from `IQM EXA`, by sweeping the controller drive frequency for each qubit.

A first coarse round is performed spanning the whole available range $0 - 7$ GHz. This allows to have an idea of the frequency range in which transmon resonate.

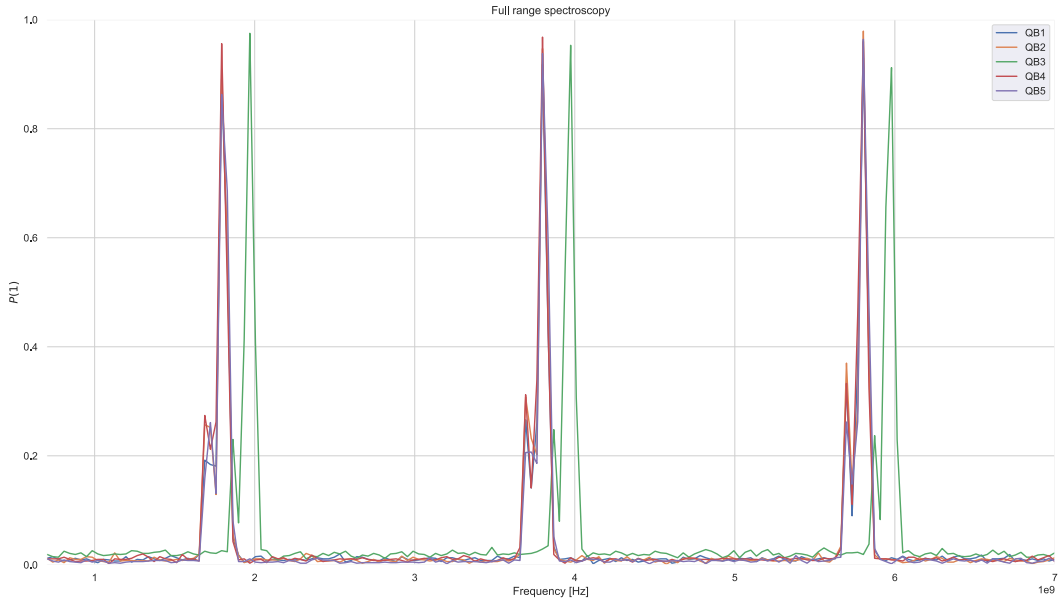


Figure 45: Full range spectroscopy on the *Lagrange* qubits.

It can be seen that the main resonance is in the $3 - 4$ GHz range where, for each qubit, a pair of peaks is present. Moreover replicas of this shape are present at ~ 2 GHz and ~ 6GHz.

Let us focus on the main resonance and perform a detailed spectroscopy there:

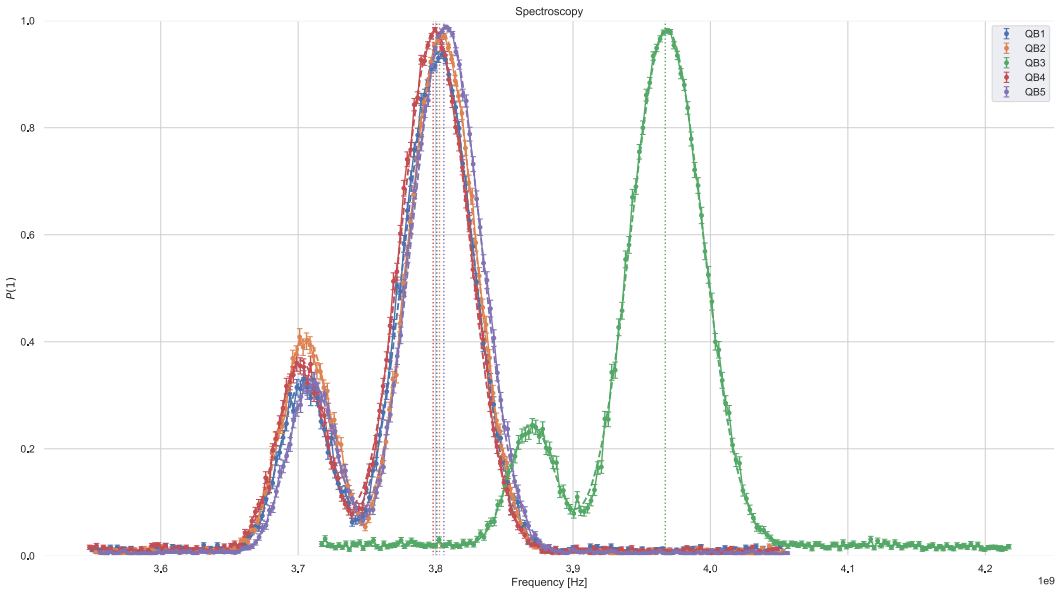


Figure 46: Detailed spectroscopy on the *Lagrange* qubits.

Noticeably, the drive frequency of the central qubit QB3 is detuned by approximately 200 MHz higher than the peripheral qubits. In the star topology of the *Lagrange* chip, this central node is highly connected via multiple tunable couplers having bigger capacitance, leading to smaller charging energy. To mitigate microwave cross-talk, frequency collisions, and the impact of the increased parasitic capacitance from these connections, central qubit is usually engineered with a higher target frequency during fabrication.

Each qubit has two peaks, let us start by focussing on the highest one. It reaches probability 1 of measuring the excited state, and after fitting the gaussian the variance is roughly 20 MHz confirming Eq. (4.13), detailed results are reported in Table 9.

	QB**1**	QB**2**	QB**3**	QB**4**	QB**5**
f_{10}(MHz)	3801.42	3803.90	3967.43	3798.53	3806.87
Δf_{10}(MHz)	0.01	0.01	0.01	0.01	0.01
σ_{10}(MHz)	19.62	18.29	24.08	20.15	19.52
$\Delta\sigma_{10}$(MHz)	0.02	0.01	0.02	0.01	0.01

Table 9: Numerical result of gaussian fitting for the main peak in spectroscopy.

Regarding the second peak, it is the result of a second order phenomenon: 2 Photons Excitation (2PE). Let us understand this process by considering the transition energies for

$$E_{20} = E_{21} + E_{10} \tag{5.2}$$

By recalling the definition of the anharmonicity coefficient

$$\alpha = E_{21} - E_{10} \Longrightarrow E_{20} = 2E_{10} + \alpha \tag{5.3}$$

When the drive pulse is sent, there is a chance that two photons interact by stimulating the $|0\rangle \rightarrow |2\rangle$ transition. To satisfy energy conservation this happens for photons at a frequency

$$x = \frac{E_{20}}{2} = E_{10} + \frac{\alpha}{2} \tag{5.4}$$

It is therefore possible to measure the anharmonicity by finding the frequency at which 2PE happens.

$$\alpha = 2(x - E_{10}) \tag{5.5}$$

Therefore, by fitting also the smaller gaussian peak and resolving its frequency, the anharmonicity can be evaluated. To enhance fitting stability, the two gaussians are not treated independently the center of the smaller is anchored to the bigger one as reported in Listing 2, estimating directly the distance between the two peaks which is $|\alpha|/2$.

```python
def two_gaussians(x, baseline,
    amp_01, f_01, sigma_01,
    amp_2PE, alpha, sigma_2PE
):

    f_x = f_01 + alpha/2

    return (
      baseline
      + amp_01 * gaussian(x, f_01, sigma_01)
      + amp_2PE * gaussian(x, f_x, sigma_2PE)
    )
```

Listing 2: Extract of code showing the relation between `f_x` and `f_2PE`.

Fitting results are reported in Table 10.

	QB**1**	QB**2**	QB**3**	QB**4**	QB**5**
α(MHz)	−195.45	−197.50	−198.93	−194.19	−194.17
$\Delta\alpha$(MHz)	0.27	0.19	0.50	0.24	0.24
σ(MHz)	11.06	11.61	10.42	11.34	10.00
$\Delta\sigma$(MHz)	0.09	0.06	0.19	0.08	0.08

Table 10: Numerical result of gaussian fitting for the smaller peak in spectroscopy and evaluated anharmonicity.

By taking a closer look at the standard deviations in Table 6 and Table 7, it can be noticed that the secondary peaks have half the standard deviation of the primary ones. This is a typical signature of a two-photon excitation (2PE).The intrinsic spectral width of the transition (e.g., due to the pulse Fourier limit or decoherence) defines an energy tolerance $\hbar\Delta\omega$. For the primary single-photon transition $|0\rangle \rightarrow |1\rangle$, the resonance condition on the drive frequency

$$|\omega_{10} - \omega_d| < \Delta\omega \tag{5.6}$$

In a 2PE $|0\rangle \to |2\rangle$, the system absorbs two identical photons, meaning the total energy provided is $2\hbar\omega_d$. The resonance condition therefore becomes:

$$|\omega_{20} - 2\omega_d| < \Delta\omega \implies \left|\frac{\omega_{20}}{2} - \omega_d\right| < \frac{\Delta\omega}{2} \tag{5.7}$$

Since the parameter being swept during spectroscopy is the single-photon drive frequency ω_d, the observed bandwidth for the 2PE is strictly halved.

A crucial observation regarding the $|2\rangle$ measured state is that it is still marked as a `1` by the discriminator. To make sure this is actually a 2PE the $I - Q$ cloud should be analyzed:

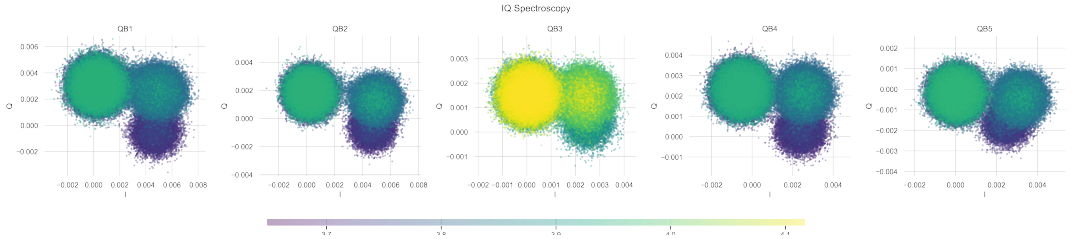


Figure 47: $I - Q$ clouds for all qubits of *Lagrange* for the spectroscopy experiment (color maps shot frequency).

Figure 47 shows exactly 3 distinct clouds of points, meaning that the $|2\rangle$ state is actually reached. In the scatter plot each point corresponds to a shot. The path in the $I - Q$ plane can be found by averaging all measures performed at the same frequency. Path measured in this way are plotted in Figure 48.

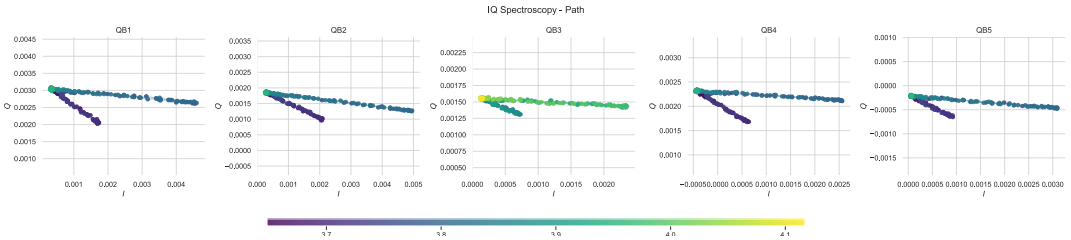


Figure 48: $I - Q$ measurements for all qubits of *Lagrange* for the spectroscopy experiment, averaged by their frequency.

Even though the exact point at each frequency is not clearly visible due to overlapping, this plots allow to identify the overall states.

5.3. Qubit coherence characterization

5.3.1. Inversion Recovery (T1)

The most important decision for this experiment lies in the sampling space, both in the separation between samples but also in the measured range and in the amount of shots. For this implementation, a hybrid sampling space is adopted by fixing the amount of samples and the fraction of them within the linear region. Typical superconducting qubits have relaxation times T_1 in the order of hundreds of microseconds, so it is worth assuming $T_1 = 100\mu s$, moreover an hybrid sampling space is used with a 70/30 linear/log ratio. After fitting the curve, resulting T_1 are reported in Table 11.

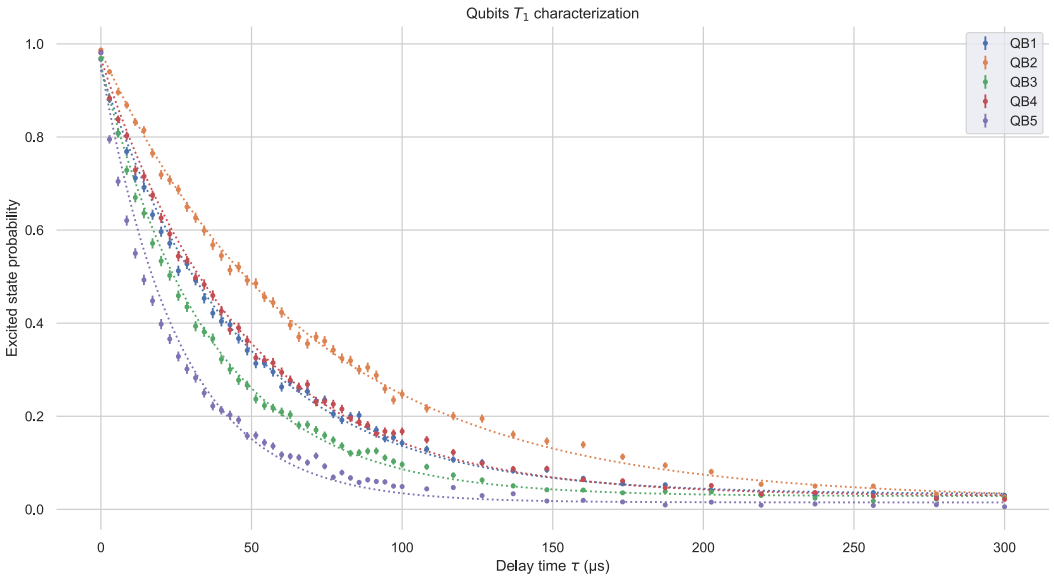


Figure 49: Hybrid sampling T_1 fitting on all qubits of *Lagrange*.

QB1	QB2	QB3	QB4	QB5
$46.09 \pm 0.4\mu s$	$68.88 \pm 0.6\mu s$	$36.14 \pm 0.3\mu s$	$47.52 \pm 0.4\mu s$	$25.88 \pm 0.2\mu s$

Table 11: Experimental estimations of the T_1 times for *Lagrange* qubits.

It should be noted that the evaluated uncertainties refer strictly to the single measurement run. Since this parameter intrinsically drifts over time, performing

repeated measurements over a longer period is necessary to fully characterize the long-term stability of the device.

5.3.2. Ramsey (T_2^*)

Starting from Eq. (4.26) it is convenient to introduce a degree of freedom in the phase of the sinusoid to enhance fitting stability. This allows the `sciPy curve_fit` to take into account some fraction of oscillation induced by non-idealities such as finite gate duration and hardware limitations, typically anticipating the oscillation with respect to the start of the delay.

$$\mathbb{P}(|1\rangle)(\tau) = A + B\cos(\Delta\omega\tau + \Delta\phi)e^{-\frac{\tau}{T_2^*}} \tag{5.8}$$

It is important to notice that having the sinusoidal term implicitly requires the sampling space to be equally distributed to avoid introducing artifacts in the fitting. Moreover the time distance between samples should be considered to respect the Shannon-Nyquist sampling condition:

$$\Delta\tau \leq \frac{1}{2\Delta f} \tag{5.9}$$

A second requirement lies in the physics of the problem: the curve is the same of a damped oscillator, then to resolve the frequency of sinusoid the exponential term should not suppress it. Roughly speaking half of a period should elapse before the exponential decay overtakes the signal:

$$\frac{1}{2\Delta f} \leq 3T_2^* \tag{5.10}$$

To set up the experiment a rough guess on T_2^* of $10\mu s$ is done to sample between $0s$ and $4T_2^*$.

Experimentally instead of using $\hat{H}$ gates, $|0\rangle$ is moved on the equatorial plane with $R_x(\frac{\pi}{2})$ and after waiting, its inverse is used to bring the state in the computational basis. This does not alter the expected results, after collecting measurements results Eq. (5.8) is fitted.

Results are plotted in Figure 50 and numerically reported in Table 12.

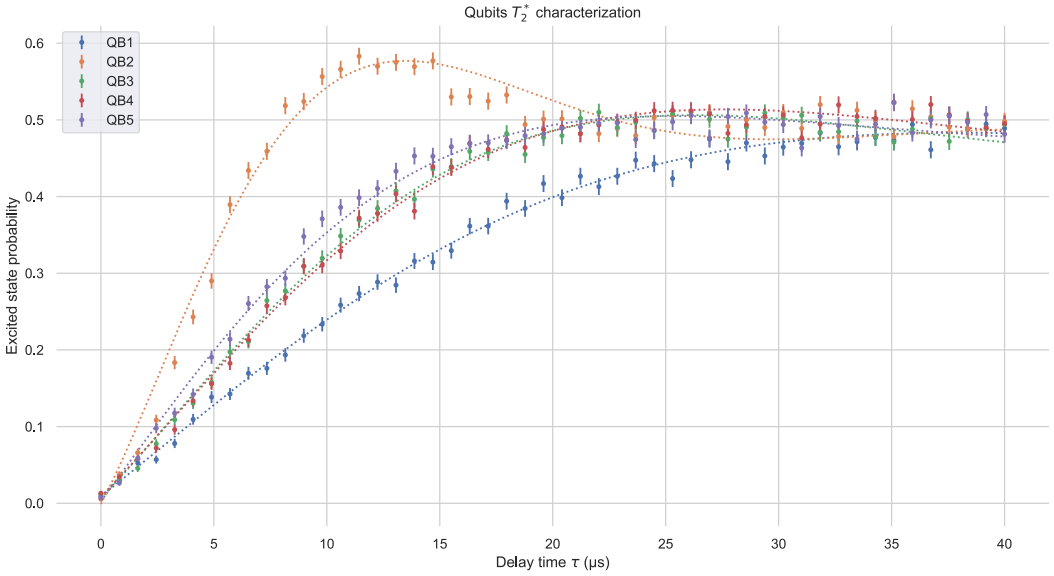


Figure 50: Fitting of Ramsey experiment measurements for T_2^* performed on all qubits of *Lagrange*

Qubit	T_2^*	Δf
QB**1**	$18.49 \pm 7.3\ \mu s$	10.19 ± 0.7 kHz
QB**2**	$8.68 \pm 0.2\ \mu s$	30.70 ± 0.7 kHz
QB**3**	$14.24 \pm 1.8\ \mu s$	15.18 ± 0.8 kHz
QB**4**	$14.81 \pm 2.2\ \mu s$	14.42 ± 0.8 kHz
QB**5**	$11.54 \pm 1.5\ \mu s$	15.11 ± 1.0 kHz

Table 12: Experimental estimations of the T_2^* times and frequency detuning for *Lagrange* qubits.

By looking at estimated detunings and uncertainties on T_2^* it can be appreciated how the fitter struggles to distinguish between the two factors. For *QB2* this is particularly clear since its detuning is clear enough, its uncertainty is very small and therefore the T_2^* is estimated with higher confidence. This can be also appreciated in Table 13 in which product of $T_2^* \cdot \Delta f$ is reported, recall that according to the conditions empirically defined previously it should be $T_2^* \Delta f \geq \frac{1}{6} \approx 0.167$.

QB1	QB2	QB3	QB4	QB5
0.188	0.267	0.216	0.214	0.174

Table 13: $T_2^* \cdot \Delta f$ for all qubits in experiment data reported in Table 12.

This means that with the T_2^* time of *Lagrange* qubits and the calibration with which the experiment is performed, detuning frequency cannot be well-resolved with the Ramsey experiment.

5.3.3. Hahn-Echo (T_2)

After an empirical rough estimation of the T_2 parameter ($20\mu s$) the hybrid linear-logarithmic sampling can be done, specifically it has been set up to perform a 70% linear from 0 to T_2 and the remaining 30% from T_2 to $4T_2$.

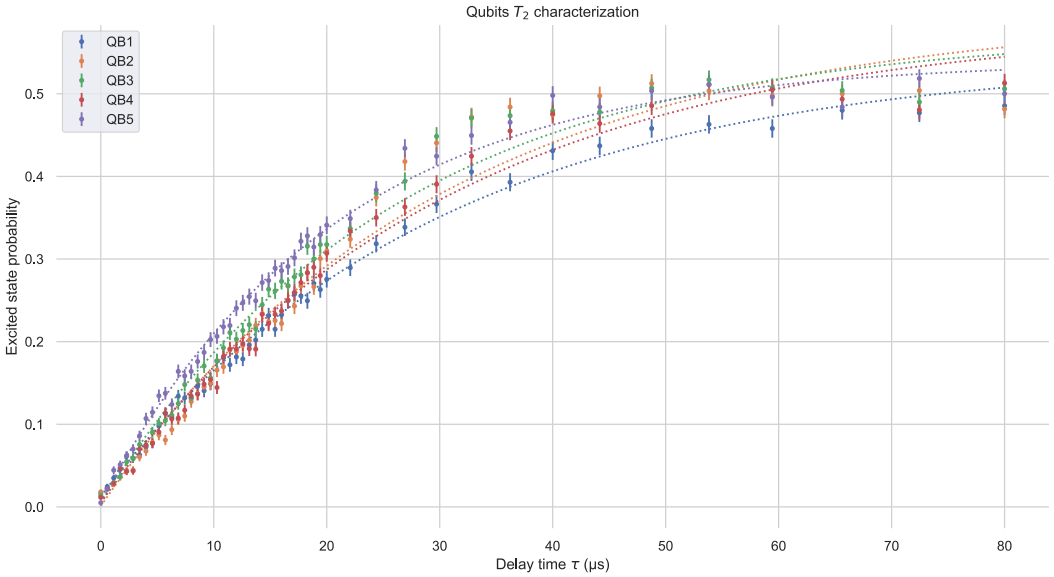


Figure 51: Fitting of Hahn-Echo experiment measurements for T_2 performed on all qubits of *Lagrange*.

From the fitting, T_2 time is evaluated and numerically reported in Table 14.

QB1	QB2	QB3	QB4	QB5
$29.53 \pm 0.9\mu s$	$29.94 \pm 0.8\mu s$	$25.92 \pm 0.6\mu s$	$30.02 \pm 0.8\mu s$	$20.77 \pm 0.4\mu s$

Table 14: Experimental estimations of the T_2 times for *Lagrange* qubits.

Data reported in Table 14 for T_2 can be used, in combination with T_1 times reported in Table 11 to evaluate

$$T_\phi = \left(\frac{1}{T_2} - \frac{1}{2T_1}\right)^{-1} \tag{5.11}$$

Being T_1 and T_2 independent measurements, uncertainty on T_ϕ can be easily propagated as

$$\begin{aligned} \sigma_{T_\phi}^2 &= \left(\frac{\partial T_\phi}{\partial T_1}\right)^2 \sigma_{T_1}^2 + \left(\frac{\partial T_\phi}{\partial T_2}\right)^2 \sigma_{T_2}^2 \\ \implies \sigma_{T_\phi} &= T_\phi^2 \sqrt{\frac{\sigma_{T_1}^2}{4T_1^4} + \frac{\sigma_{T_2}^2}{T_2^4}} \end{aligned} \tag{5.12}$$

Based on reported data, in the characterizations of T_1 and T_2 executed one after the other, T_ϕ is evaluated and reported in Table 15.

QB1	QB2	QB3	QB4	QB5
$43.44 \pm 1.9\mu s$	$38.26 \pm 1.3\mu s$	$40.40 \pm 1.5\mu s$	$43.87 \pm 1.7\mu s$	$34.68 \pm 1.2\mu s$

Table 15: Experimental estimations of the T_ϕ times for *Lagrange* qubits.

5.4. Gates characterization

5.4.1. All-XY

The 21 sequences are prepared and ran on the 5 qubits, then results are collected.

For all of the 5 qubits, results are summarily reported in Figure 52. Detailed analysis can be performed by analyzing bar plots for each qubit.

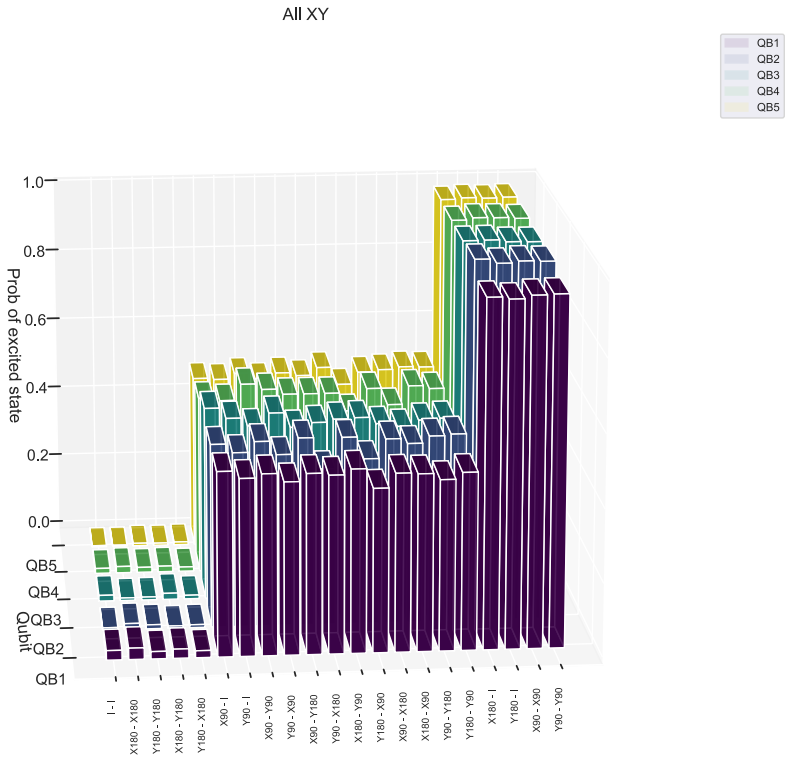


Figure 52: 3D bar plot showing measured parameters for the 21 sequences for all qubits of *Lagrange*.

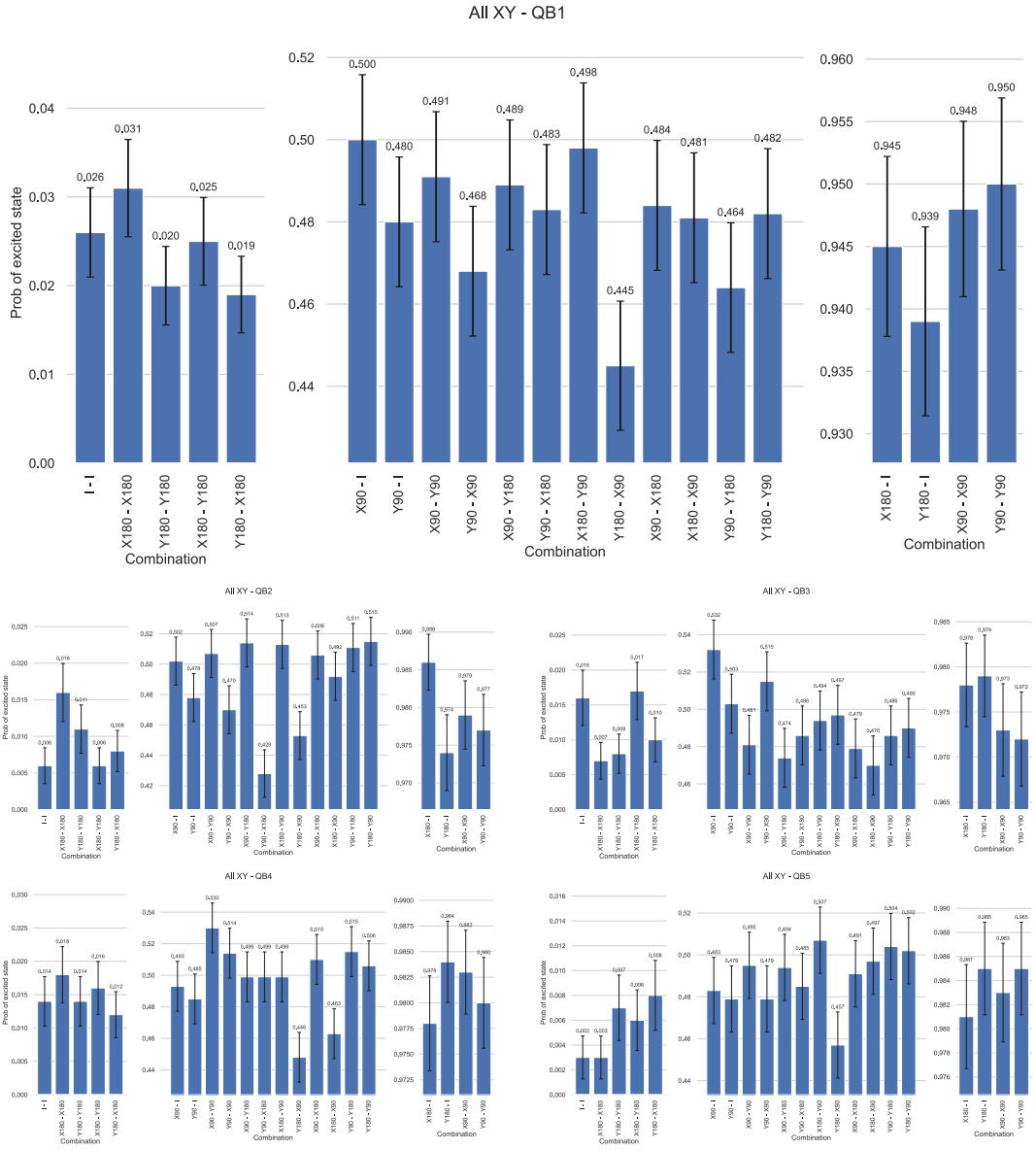


Figure 53: Detailed bar plot for All-XY experiment performed on all qubits of *Lagrange*.

For all qubits, the zig-zag pattern emerges, shining light on a phase error. Angle of the unwanted extra phase is therefore evaluated as described in Section 4.4.1 and reported in Table 16.

Qubit	QB**1**	QB**2**	QB**3**	QB**4**	QB**5**
$\Delta\theta_z$	1.32°	2.12°	−1.95°	0.92°	0.92°

Table 16: Extracted $\Delta\theta_z$ for all qubits.

5.4.2. Randomized Benchmarking

The RB experiment proposed in this work focuses on single qubit evaluations. To build quantum circuits mantaining a high level of control, the pulse level access is exploited: instead of building a circuit, the playlist is directly composed. First of all the 24 elements of $\mathcal{C}_1$ are mapped into real pulses using the decomposition:

$$G = R_z(\delta)\ \text{PRX}\ (\theta, \varphi) \tag{5.13}$$

Then, as an optimization, inverse for each of the 24 Clifford gates is evaluated in a lookup table, allowing to fast access. While sampling the Clifford gates to be appended in the circuit, the inverse is accessed in $\mathcal{O}(1)$ and applied to an accumulator-like structure. This opportunity is embedded in the definition of $\mathcal{C}_n$. By applying a sequence of gates from $\mathcal{C}_n$, the obtained gate must always be an element of $\mathcal{C}_n$. Moreover, for each applied gate its inverse must also be an element of $\mathcal{C}_n$, therefore while picking the random $i-\text{th}$ gate for the sequence, its inverse is fixed in $\mathcal{C}_n$. This principle can be appreciated in Figure 54.

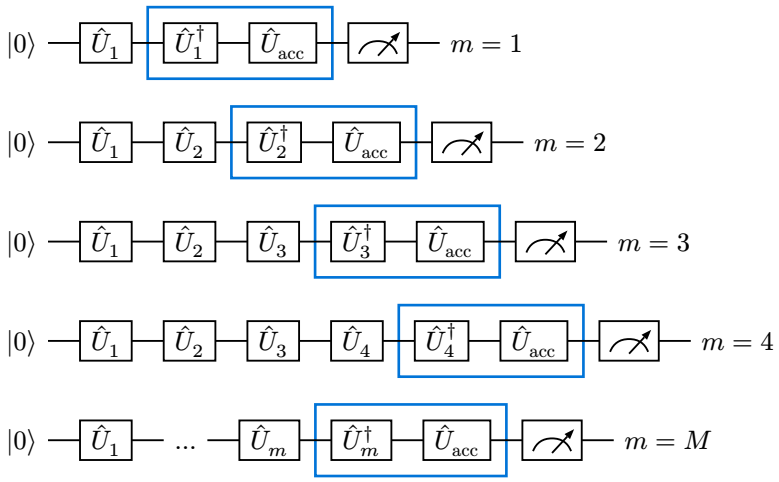


Figure 54: Quantum circuits for various m highlighting the benefit of the accumulator gate.

Moreover, an hybrid sampling is adopded for the total length m, mixing linear sampling from 1 to 50 for 25% of the samples and a logaritmic from 50 to 5000 for the remaining 75%. After running the experiment with $K = 30$ different circuit per each sampled depth, fitting is performed (Figure 55).

Infideity r is then evaluated and reported in Table 17. Whereas r represents the average depolarization error probability, it is more convenient to frame it in terms of average fidelity per Clifford gate

$$r = \frac{1-p}{2} \qquad F = 1 - r \tag{5.14}$$

	QB**1**	QB**2**	QB**3**	QB**4**	QB**5**
$F(\%)$	99.940	99.923	99.947	99.949	99.965
Δ	0.005	0.005	0.004	0.004	0.003

Table 17: Average 1 qubit gate fidelities from the RB fitting.

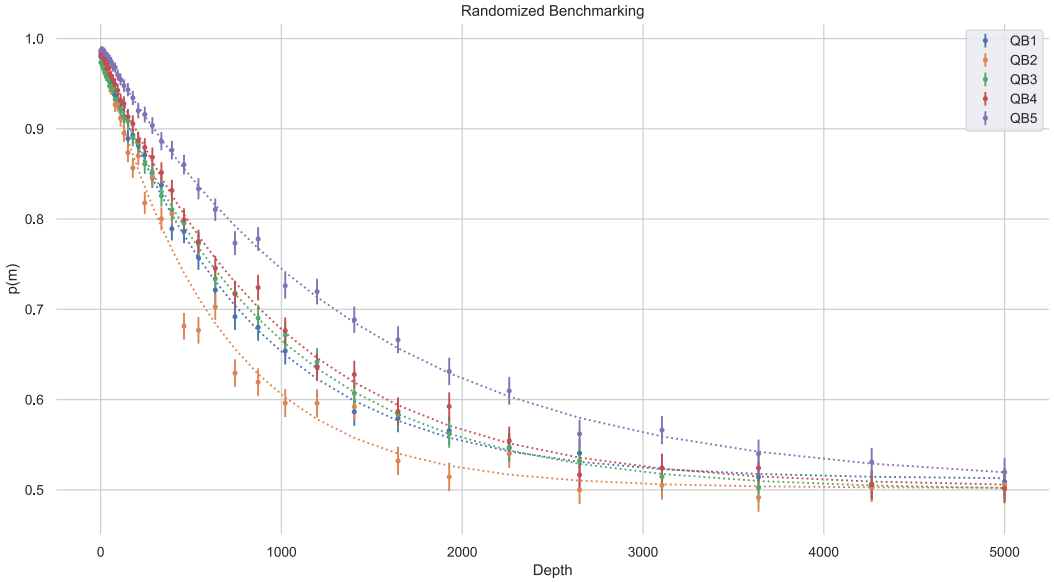


Figure 55: Fit for the RB experiment on all *Lagrange* qubits.

5.4.3. Interleaved Randomized Benchmarking

For the IRB experiment here reported, 5 different GUT are chosen:

$$\left\{\hat{H}, \hat{S}, \hat{X}, \hat{Y}, \hat{Z}\right\} \tag{5.15}$$

Results from Table 17 are used as reference for the estimation of parameters since executed right before this IRB experiment. Fitting for all traces is reported aggregating same experiments on the same qubit by color and same gate by marker.

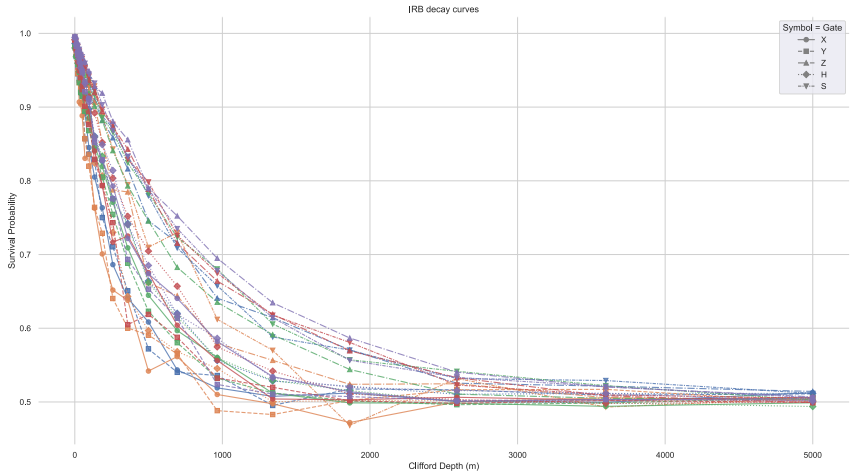


Figure 56: Fitting for IRB experiment on all *Lagrange* qubits.

Gate fidelities are collected in Figure 57 showing how $\hat{S}$ and $\hat{Z}$ outperform other gates, this is because their virtual implementation is far less error prone. One would expect such bars to reach 1, this is not the case because of limited amount of twirling: K for this experiment was set to 20.

In Figure 58 the theoretical depth of gates before the first error is reported for the same experimental data, again showing the advantage of having virtual implementations for $\hat{S}$ and $\hat{Z}$ gates. Reading the heatmap by rows, QB2 shows worst results.

Another interesting fact emerges when comparing $\hat{H}$ with $\hat{X}$ and $\hat{Y}$. Unfortunately resolving the exact cause of this discrepancy is not in the scope of IRB.

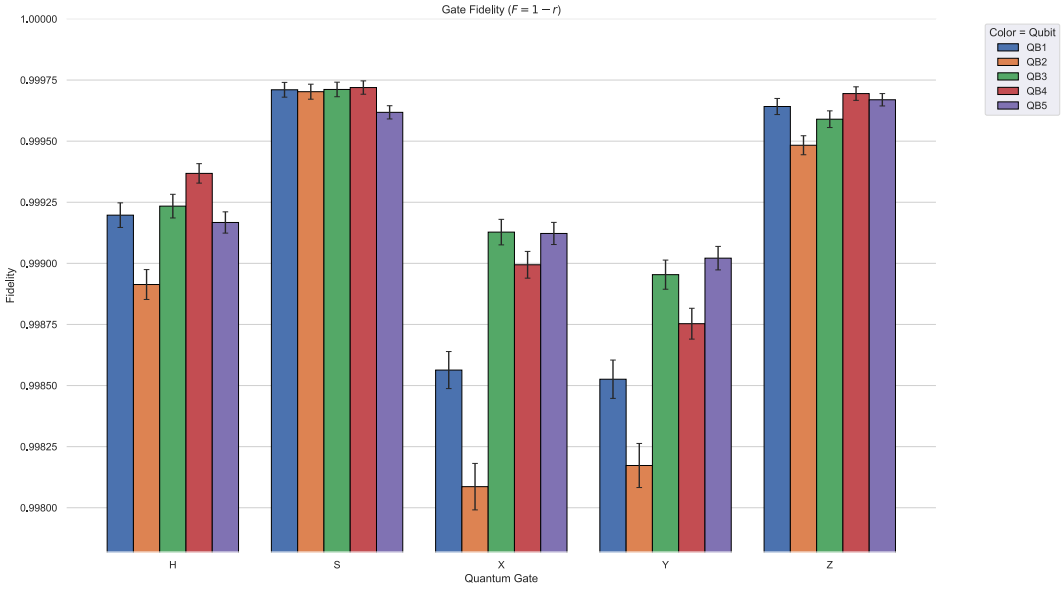


Figure 57: Bar plot with uncertainties for IRB experiment performed, results grouped per gate and colored per qubit.

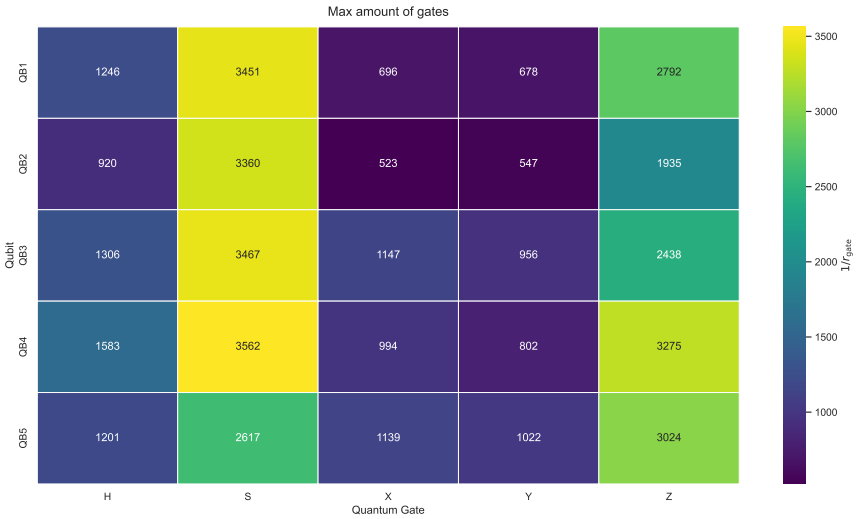


Figure 58: Estimated maximum number of gates per type per qubit.

Chapter 6
Conclusions and Future Perspectives

6.1. Conclusions

The work presented in this thesis has successfully demonstrated the development and implementation of an on-demand diagnostic and characterization suite for the *Lagrange* QPU, an IQM Spark architecture featuring five superconducting transmon qubits arranged in a star topology. With a full-stack perspective, it was possible to devise an high-level interface, starting from the quantum circuits abstraction arriving down to their pulse level implementation. Interacting directly with the hardware through the Pulla library enabled direct control of physical parameters of the hamiltonian of the system.

The experimental characterization covered the fundamental metrics of the system:

- SPAM errors: Readout Error Mitigation techniques have been employed to reduce readout errors by reconstructing the error mitigation matrix. Moreover limits of the low-level access to a quantum computer have been tested by acquiring measures in forms of IQ clouds. This latter result has been crucial for a proper interpretation of the spectroscopy experiment.
- Coherence Times: Standardized experiments such as Inversion Recovery, Ramsey, and Hahn-Echo, allowed to extract specific parameters limiting the lifespan of quantum information stored in qubits. Specifically T_1 around $25 - 68\ \mu s$ and T_2 near to $20 - 30\ \mu s$ confirmed typical values for superconducting hardware.
- Gate fidelity: Single qubit gates have been benchmarked, with three different experiments aiming to balance lightweight procedures (All-XY) with detailed per-gate information (IRB). These tests validated calibration data with a

fidelity $F > 99.9\%$ and could be used to inform an optimizer to perform a fine tuning procedure.

In summary, this thesis establishes a solid toolset to test various capacities of the system and lays the groundwork for future, more targeted experiments.

6.2. Future Perspectives

The work presented in this thesis opens several paths. Most interestingly autonomus and efficient procedures for characterization can be implemented.

The current pulse-level control can be extended to fully characterize entangling operations such as CZ gates. Deeper studies can be performed on specific QPU components such as finding optimal values for qubits and tunable couplers flux voltages (parking spots).

This toolset also provides information which can be used from high-level procedures such as Machine Learning or Bayesian-like approaches to perform informed experiments. Such tools may also be employed to optimize some parameters of this toolset itself.

The most ambitious future development is to introduce closed-loop gate optimization routines. Leveraging the readout pipeline developed in this thesis, the system could dynamically instantiate fidelity measurements and auto-correct pulse amplitudes, durations, and the DRAG parameter λ in real-time.

Appendix

A.1. Bloch Sphere

Considering the general 1-qubit quantum state $|\psi\rangle = \alpha|0\rangle + \beta|1\rangle$

Generally speaking $\alpha, \beta \in \mathbb{C}$ therefore there are 4 free parameters, making it hard for a good visualization to be possible in the 3D world.

A first constraint is posed by the normalization condition, for which

$$|\alpha|^2 + |\beta|^2 = 1 \tag{A.1}$$

Therefore reducing the degrees of freedom. It can be conveniently parametrized by writing complex numbers as imaginary exponentials with phase γ_i and modulus ρ_i:

$$\begin{aligned} |\psi\rangle &= \rho_0 e^{i\gamma_0}|0\rangle + \rho_1 e^{i\gamma_1}|1\rangle \\ &= \rho_0 e^{i\gamma_0}|0\rangle + \sqrt{1-\rho_0^2}e^{i\gamma_1}|1\rangle \end{aligned} \tag{A.2}$$

Then, recalling that a global phase term does not affect the system, an arbitrary amount $e^{i\gamma}$ can be multiplied to the global state with no observable effects. Conveniently let this phase be $-\gamma_0$,

$$|\psi\rangle = \rho_0|0\rangle + \sqrt{1-\rho_0^2}e^{i(\gamma_1-\gamma_0)}|1\rangle \tag{A.3}$$

Now, the state must live in a 2D region, specifically

$$\rho_0 \in [0,1] \qquad (\gamma_1 - \gamma_0) \in [0, 2\pi] \tag{A.4}$$

This is conveniently parametrized by introducing:

$$\varphi = (\gamma_1 - \gamma_0) \tag{A.5}$$

By looking at the rectangle spanned by these two parameters (ρ_0, φ), one could notice that φ must repeat itself so this rectangle can be promoted in the third dimension by "gluing" the boundary in which $\varphi = 0$ to the one in which $\varphi = 2\pi$. Indeed when ρ_0 is exactly 0 or 1, any phase would have no sense since the state would be respectively $|1\rangle$ or $|0\rangle$. Points on the top and, respectively, at the bottom of the cylinder are exactly indistinguishable, closing the cylinder with two poles. The sphere naturally emerged from the constraints of our system.

Therefore

$$\rho_0 = \cos\left(\frac{\theta}{2}\right) \tag{A.6}$$

$$|\psi\rangle = \cos\left(\frac{\theta}{2}\right)|0\rangle + e^{i\varphi}\sin\left(\frac{\theta}{2}\right)|1\rangle \tag{A.7}$$

The two real parameters $\theta \in [0, \pi]$ and $\varphi \in [0, 2\pi]$ completely characterize the state. These parameters can be naturally interpreted as spherical coordinates on the unit sphere in $\mathbb{R}^3$ (the Bloch sphere):

$$\theta \text{ is the polar angle}, \quad \varphi \text{ is the azimuthal angle.} \tag{A.8}$$

The mapping is one-to-one (except for the usual coordinate singularities at the poles $\theta = 0$ and $\theta = \pi$), so pure single-qubit states are in one-to-one correspondence with points on the surface of the Bloch sphere.

A.2. Unitary Transformations

Unitary transformations play a crucial role in quantum mechanics, as they describe the evolution of closed systems.

An operator is said to be unitary if its inverse corresponds to its adjoint:

$$U^{-1} = U^{\dagger} \tag{A.9}$$

Subsequent application of unitary operators still is a unitary operator, meaning that the evolution of a system can be described by many smaller evolutions one after the other.

$$U = ...U_3U_2U_1 \qquad U_1^{\dagger}U_2^{\dagger}U_3^{\dagger}...U_3U_2U_1 = \mathbb{I} \tag{A.10}$$

A useful way to construct a unitary operator is to consider an observable, represented by a Hermitian operator A, and use it to define the imaginary exponential

$$U = e^{iA} \quad A = A^{\dagger} \tag{A.11}$$

By requiring every evolution to be described by an invertible transformation, we implicitly assume that the evolution of a closed system is reversible: given the final state, the initial state can be uniquely recovered by applying the inverse transformation.

This property ensures that unitary transformations preserve the total probability.

In quantum computing, this property has important implications. However, by considering the quantum computer as the closed system, not **every** operation performed is reversible. Measurements and reset operations, in general, cannot be described by unitary operators acting on the quantum register alone. The distinction between reversible and irreversible operations is particularly relevant when considering the energetic cost of computation. In classical computing, logically irreversible operations can result in the loss of information. A paradigmatic example is the erasure of a bit, which maps two possible initial states, `0` and `1`, to the same final state. If the bit is initially in an equiprobable mixture of these two states, erasing it reduces its entropy by

$$\Delta S_{\text{sys}} = -k_B \ln(2) \tag{A.12}$$

Each computing device, when performing irreversible operations loses some information. Each lost bit in a statistical mechanics point of view corresponds

to a halving of the available microstates, therefore an increase proportional to $\ln(2)$ in the entropy of the universe. When such a process happens at a finite temperature, an amount of heat Q is dissipated to the environment. This amount is evaluated as

$$Q = -T\Delta S = k_B T \ln(2) \tag{A.13}$$

This result is known as the Landauer limit, which establishes a lower bound on the thermodynamic cost of classical irreversible computation. However, quantum computers must interact with the classical world to initialize the register and read out the final result. These operations establish an interface between quantum information processing and classical information handling. This distinction is related to the concept of the Heisenberg cut, which separates the quantum description of a system from the classical description of the measurement apparatus. Initialization may also involve reset operations, which are not generally reversible when considered at the level of the quantum register alone. In present-day quantum computers, interactions with the external world are not limited to initialization and readout: quantum gates are also controlled by external electronic equipment, typically operating at room temperature. This control architecture introduces practical constraints on quantum operations and motivates the investigation of more efficient control strategies.

Bibliography

[1] J. Rönkkö *et al.*, "On-premises superconducting quantum computer for education and research," *EPJ Quantum Technology*, vol. 11, p. , 2024, doi: 10.1140/epjqt/s40507-024-00243-z.

[2] E. Magesan, J. Gambetta, and J. Emerson, "Scalable and Robust Randomized Benchmarking of Quantum Processes," *Physical review letters*, vol. 106, p. 180504, 2011, doi: 10.1103/PhysRevLett.106.180504.

[3] E. Magesan *et al.*, "Efficient measurement of quantum gate error by interleaved randomized benchmarking," *Physical review letters*, vol. 109, no. 8, p. 80505, 2012.

[4] M. A. Nielsen and I. L. Chuang, *Quantum Computation and Quantum Information: 10th Anniversary Edition*. Cambridge: Cambridge University Press, 2010. doi: 10.1017/CBO9780511976667.

[5] N. S. Yanofsky and M. A. Mannucci, *Quantum Computing for Computer Scientists*. Cambridge: Cambridge University Press, 2008.

[6] N. Khaneja and S. J. Glaser, "Cartan decomposition of SU(2n) and control of spin systems," *Chemical Physics*, vol. 267, no. 1, pp. 11–23, 2001, doi: https://doi.org/10.1016/S0301-0104(01)00318-4.

[7] D. Gottesman, "The Heisenberg Representation of Quantum Computers." [Online]. Available: https://arxiv.org/abs/quant-ph/9807006

[8] C. M. Dawson and M. A. Nielsen, "The Solovay-Kitaev algorithm," *Quantum Information & Computation*, vol. 6, no. 1, pp. 81–95, 2006.

[9] P. Viviani *et al.*, "Lagrange: Operating Italy's First Publicly-Accessible Quantum Computer for Research and Education." [Online]. Available: https://arxiv.org/abs/2604.21695

[10] F. Marxer *et al.*, "Long-Distance Transmon Coupler with cz-Gate Fidelity above 99.8%," *PRX Quantum*, vol. 4, no. 1, Feb. 2023, doi: 10.1103/prxquantum.4.010314.

[11] D. C. McKay, C. J. Wood, S. Sheldon, J. M. Chow, and J. M. Gambetta, "Efficient Z gates for quantum computing," *Physical Review A*, vol. 96, no. 2, Aug. 2017, doi: 10.1103/physreva.96.022330.

[12] Zurich Instruments, "Dispersive Shift - LabOne Q." Accessed: Sept. 15, 2026. [Online]. Available: https://docs.zhinst.com/labone_q_user_manual/applications_library/how-to-guides/sources/01_superconducting_qubits/01_workflows/10_dispersive_shift.html

[13] IQM, "Pulse - concepts and classes." Accessed: Sept. 21, 2026. [Online]. Available: https://docs.iqm.tech/4.6/iqm-pulse/concepts.html

[14] Zurich Instruments, "Hahn Echo - LabOne Q." Accessed: Sept. 12, 2026. [Online]. Available: https://docs.zhinst.com/labone_q_user_manual/applications_library/how-to-guides/sources/01_superconducting_qubits/01_workflows/08_echo.html